



Universiteit  
Leiden  
The Netherlands

## Steps in gas-surface reactions

Lent, R. van

### Citation

Lent, R. van. (2019, December 16). *Steps in gas-surface reactions*. Retrieved from <https://hdl.handle.net/1887/81577>

Version: Publisher's Version

License: [Licence agreement concerning inclusion of doctoral thesis in the Institutional Repository of the University of Leiden](#)

Downloaded from: <https://hdl.handle.net/1887/81577>

**Note:** To cite this publication please use the final published version (if applicable).

Cover Page



Universiteit Leiden



The following handle holds various files of this Leiden University dissertation:  
<http://hdl.handle.net/1887/81577>

**Author:** Lent, R. van

**Title:** Steps in gas-surface reactions

**Issue Date:** 2019-12-16

# Steps in gas-surface reactions

## Proefschrift

ter verkrijging van  
de graad van Doctor aan de Universiteit Leiden,  
op gezag van Rector Magnificus prof. mr. C.J.J.M. Stolker  
volgens besluit van het College voor Promoties  
te verdedigen op maandag 16 december, 2019  
klokke 11:15

door

**Richard van Lent**  
geboren te Gorinchem in 1986

## Promotiecommissie

<b>Promotor:</b>	Dr. L. B. F. Juurlink Prof. dr. M. T. M. Koper
<b>Co-promotor:</b>	Dr. M. A. Gleeson
<b>Overige leden:</b>	Prof. dr. E. Hasselbrink Prof. dr. M. C. M. van de Sanden Prof. dr. G. J. Kroes Dr. I. M. N. Groot Prof. dr. H. S. Overkleef

Dit werk maakt deel uit van het onderzoeksprogramma CO<sub>2</sub>-neutral fuels programma met projectnummer 13CO24-1 dat (mede)gefinancierd is door de Nederlandse Organisatie voor Wetenschappelijk Onderzoek (NWO).



Printed by Ipskamp printing

**ISBN:** 978-94-028-1849-9



<b>Contents</b>	<b>i</b>
<b>1 Introduction</b>	<b>1</b>
<b>2 Experimental chapter</b>	<b>11</b>
Curved single crystals . . . . .	12
Boxfish . . . . .	14
Lionfish . . . . .	15
Experimental techniques . . . . .	28
<b>3 Site-specific reactivity of molecules with surface defects</b>	
– the case of H <sub>2</sub> dissociation on Pt	41
Introduction . . . . .	42
Method . . . . .	44
Results and Discussion . . . . .	45
Conclusion . . . . .	49
<b>4 Two-faced step edges in HD exchange on Pt</b>	<b>51</b>
Introduction . . . . .	52
Method . . . . .	53
Results and Discussion . . . . .	56
Conclusion . . . . .	66
<b>5 Step-type dependence of oxygen reduction on Pt(1 1 1) surfaces</b>	<b>67</b>
Introduction . . . . .	68
Method . . . . .	69

---

Results and Discussion . . . . .	70
Conclusion . . . . .	77
<b>6 Applying reflection absorption infrared spectroscopy on a curved surface – how do step-type and step density influence CO adsorption on stepped Pt(1 1 1)?</b>	<b>79</b>
Introduction . . . . .	80
Experimental details . . . . .	81
Literature review of CO adsorbed to platinum surfaces . . . . .	85
Results . . . . .	87
Top-bound CO . . . . .	89
Bridge-bound CO . . . . .	92
Conclusion . . . . .	95
<b>7 Outlook – CO<sub>2</sub> spectroscopy and state-preparation for state-resolved dissociation experiments</b>	<b>97</b>
CO <sub>2</sub> spectroscopy . . . . .	98
State preparation of CO <sub>2</sub> in the supersonic molecular beam . . .	107
<b>8 Summary and conclusion</b>	<b>127</b>
<b>9 Nederlandse samenvatting</b>	<b>133</b>
<b>A IGOR Pro procedures</b>	<b>137</b>
<b>B Chapter 3</b>	<b>147</b>
<b>C Chapter 4</b>	<b>151</b>
<b>D Chapter 5</b>	<b>157</b>
<b>Bibliography</b>	<b>173</b>
<b>List of publications</b>	<b>185</b>
<b>Curriculum vitae</b>	<b>187</b>

200 years ago, Sir Humphry Davy worked on understanding combustion.[1] He theorized that flames required higher temperatures to glow than solids. To test his theory, he devised an experiment. He suspended a platinum gauze above a flame to heat the metal up. When he quenched the flame by adding too much gaseous fuel, the flame extinguished within seconds. However, the hottest part of the platinum gauze remained aglow for several minutes until all combustible gases were consumed. While limited in the number of metals he could test, the experiment only succeeded with platinum and palladium. This was the serendipitous discovery of what was not yet called catalysis.[2] Davy applied his discovery in a safety lamp for coal miners that could warn the user of highly flammable gases and asphyxiation. Soon after Davy's discovery, Henry identified the two chemical reactions responsible: combustion of hydrogen and carbon monoxide to form water and carbon dioxide.[3] The discovery that a platinum wire glows in the presence of combustible gases and oxygen literally and metaphorically sparked 200 years of heterogeneous catalysis research.

Nowadays, it seems impossible to imagine a world without catalysis. It is used at some point in almost every commercial product around us, e.g. in growing food, making plastics, or cleaning emissions from our car exhaust. It is a multi-billion dollar industry that will never disappear. So what does a catalyst, such as Davy's platinum wire, actually do? Figure 1.1 illustrates the principle. Reactions that occur without a catalyst generally have a significant reaction barrier (black). A catalyst (red) changes the reaction path, thereby reducing the reaction barrier and stabilizing key intermediate(s). The product P is subsequently released or desorbed. A good catalyst increases the reaction rate but is unaltered after the reaction is complete. It can repeat the catalytic process countless of times. The catalyst does not alter the equilibrium but does decrease the time it takes to reach equilibrium. Three general forms of catalysis are distinguished: homogeneous catalysis, heterogeneous catalysis, and biocatalysis. The difference between the three is the state of matter of the catalyst and the reactants that it acts upon. Homogeneous catalysts are in the same state of matter (gas, liquid, or solid phase) as the reactants and generally occurs in the liquid or gas phase. Biocatalysis is a biological variation on homogeneous catalysis, where proteins are the catalyst. Both proteins and homogeneous catalysts usually have a well-defined active site.

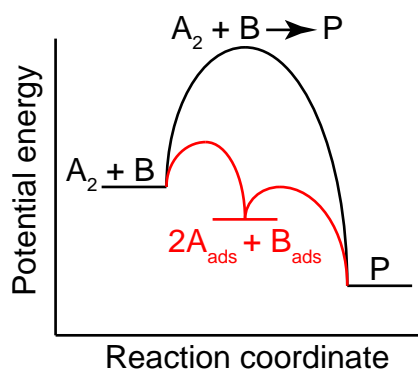


**Figure 1.1:** Schematic illustration how a generic catalyst (red) lowers the reaction barrier compared to the reaction taking place without a catalyst (black).

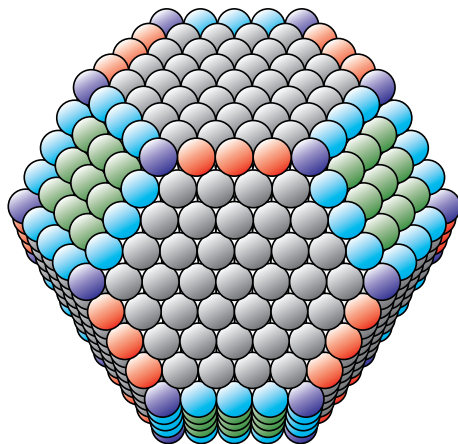


**Figure 1.2:** An exemplary nanoparticle with various surface sites: hexagonal (1 1 1) (grey) and square (0 0 1) (green) terraces. Different step edges and corners are depicted in blue, red, and purple.

In contrast, heterogeneous catalysts are in a different state of matter than the reactants – usually the solid phase. Heterogeneous catalysts generally consist of finely dispersed nanometer-sized metal particles on a porous support. An example of such a metal nanoparticle, with the face-centered cubic structure, is shown in figure 1.2. The surface of this nanoparticle comprises a variety of different types of surface atoms, indicated with different colors. Green and grey atoms represent a square (0 0 1) and hexagonal (1 1 1) terraces. Defect sites – shown in blue, red, and purple – have lower coordination numbers and generally bind reactants stronger. These different surface sites may each exhibit different catalytic activity. Catalytic reactions sometimes have an optimum particle size. These particle size effects are a trade-off between getting as much of a specific reaction site without significantly altering the electronic properties of the site. Changing the latter influences both the binding energies and catalytic activity according to the Brønsted-Evans-Polanyi principle.[4]

This thesis seeks to provide new insights in the fundamental processes that underlie heterogeneous catalysis. How defects such as those shown in figure 1.2 influence reactivity is still studied to this day, even to under-

stand the reactions that Davy already discovered 200 years ago. Since then, countless scientific advances were made that enable the work in this thesis. We would like to highlight some notable discoveries that have defined the field, starting with the work of Irving Langmuir that birthed the field of surface science and earned him the Nobel prize in 1932.[5] Langmuir studied light bulbs at General Electric and resolved a number of fundamental problems with some simple vacuum experiments. First, he showed that hydrogen molecules are dissociated by hot tungsten filaments and that these hydrogen atoms subsequently adsorb to the glass walls of the light bulb. The saturation coverage is approximately equal to the surface atoms available. Thereafter, he showed that oxygen also readily dissociates at tungsten filaments, thereby significantly reducing the emission current. The binding energy of oxygen to the tungsten surface is very high, comparable to covalent bonds. Finally, upon introducing a mixture of hydrogen and oxygen to the tungsten filament, oxygen poisons the surface. Catalytic activity towards hydrogen dissociation is negligible until adsorbed oxygen is removed from the surface. Upon oxygen removal, atomic hydrogen adsorption by the glass bulb proceeds as before. These observations were the basis for what is now known as the Langmuir-Hinshelwood reaction mechanism: reactants dissociatively adsorb at a catalytic surface and subsequently recombinationally desorb as the product.

Another noteworthy discovery in connection to the work in this thesis is that of electron diffraction, for which Thomson and Davisson were awarded the Nobel prize in 1937. We focus here on the Davisson-Germer experiment.[6] Although de Broglie[7] predicted the wave-particle duality for all particles, it had only been confirmed for photons. Unaware of this prediction, Davisson and Germer were scattering low energy electrons off a nickel surface. At some point in their experiments, they accidentally oxidized their polycrystalline nickel sample.[8] To resolve this problem, they decided to reduce the sample in hydrogen using a high temperature oven. In doing so, they annealed their polycrystalline nickel sample to temperatures sufficient to grow single crystalline grains that were larger than the size of their electron beam. Consequently, they effectively employed a single

crystal surface and showed that electrons exhibit wave-like behavior by diffracting.[8] Later, they purposely used a Ni(1 1 1) single crystal surface to perform their experiments.[6, 9] To this day, the surface science approach uses single crystal surfaces. Moreover, Low Energy Electron Diffraction is one of the most prominent surface science techniques for verifying the surface structure of single crystal surfaces.

A third technique essential to this thesis is that of molecular beams. Otto Stern was awarded the 1943 Nobel prize for his work on developing molecular beams. Although he was not the first to use atomic or molecular beams, he used them with Gerlach to show that atoms have angular momentum. In his Nobel lecture, Stern lauded the possibilities of molecular beams: "The most distinctive characteristic property of the molecular ray method is its simplicity and directness." [10] Molecular beams were used in those days to resolve problems related to classical and quantum physics. King and Wells[11] developed a surface science apparatus for directly measuring nitrogen sticking probabilities at tungsten single crystal surfaces using a molecular beam. Their approach is discussed in chapter 2. Auerbach et al.[12] showed that kinetic energy and incidence angle strongly affect the dynamics of N<sub>2</sub> dissociation at W(1 1 0). The observed dynamical behavior was unexpected and the field flourished. The dynamics of dissociative chemisorption were measured for various molecules at different surfaces.[13–18]

Throughout the years, many developments have enabled experimentalists to control virtually every aspect of molecule-surface collisions by using molecular beams. We highlight some notable examples. Early surface science experiments used nozzle heating or plasma beam sources to increase the internal state distribution of molecules.[17] Combining molecular beams with lasers opened up new possibilities, e.g. stimulated Raman pumping enabled incident hydrogen molecules to be vibrationally tagged for state-resolved dissociation and resonance enhanced multi-photon ionization (REMPI) detection for state-resolved scattering.[19] Molecules such as methane or water had to wait for the advent of tunable coherent in-

frared light sources for state-resolved dissociation.[20, 21] For methane, vibrational excitation opened up many new possibilities. As a polyatomic molecule, it has a lot more vibrational degrees of freedom than diatomic molecules. The vibrational efficacy, which compares vibrational and kinetic energy in breaking the bond, varies for different normal mode vibrations (and their overtones).[20, 22, 23] Using isotopologues, it is possible to also show bond specificity in  $\text{CHD}_3$  dissociation.[24] Even more recently, hexapole alignment gives stereo-dynamic control over incident  $\text{O}_2$  molecules, showing what molecular orientation is most beneficial for dissociation.[25–27]

The surface science approach uses single crystal surfaces as model catalyst. These model catalysts are generally studied under ultrahigh vacuum (UHV) conditions. New surface science techniques are usually first applied to so-called low Miller index surfaces. For metals with the face centered cubic structure, such as platinum, these are  $(1\ 1\ 1)$ ,  $(1\ 1\ 0)$ , and  $(0\ 0\ 1)$  shown in figure 1.3a. Single crystal boules are cut to expose one of these low Miller index surfaces. Since it is impossible to cut metal single crystals with subnanometer accuracy, small miscuts always result in long planes of low Miller index surfaces separated by step edges. These step edges can dominate overall reactivity at the surface if the low Miller index surface exhibits little to no reactivity. The influence of step edges can be studied systematically by purposely ‘miscutting’ the single crystal boule at a larger angle, as schematically shown in figure 1.3b. The surface then exposes high Miller index surfaces with shorter terraces separated by step edges, such as the  $(5\ 5\ 3)$  surface shown. Throughout this thesis, surfaces with **A-type** or  $\{0\ 0\ 1\}$  steps are marked in blue. Surfaces containing **B-type** or  $\{1\ 1\ 0\}$  steps are marked in red.

UHV allows for a large range of surface sensitive techniques.[28] However, the use of separately polished flat surfaces to probe the influence of different step types and/or terrace widths imposes difficulties:[29] sample-to-sample variation in the quality and purity of the surface and bulk of individual single crystals; the need to break vacuum; initial cleaning of new crystals,



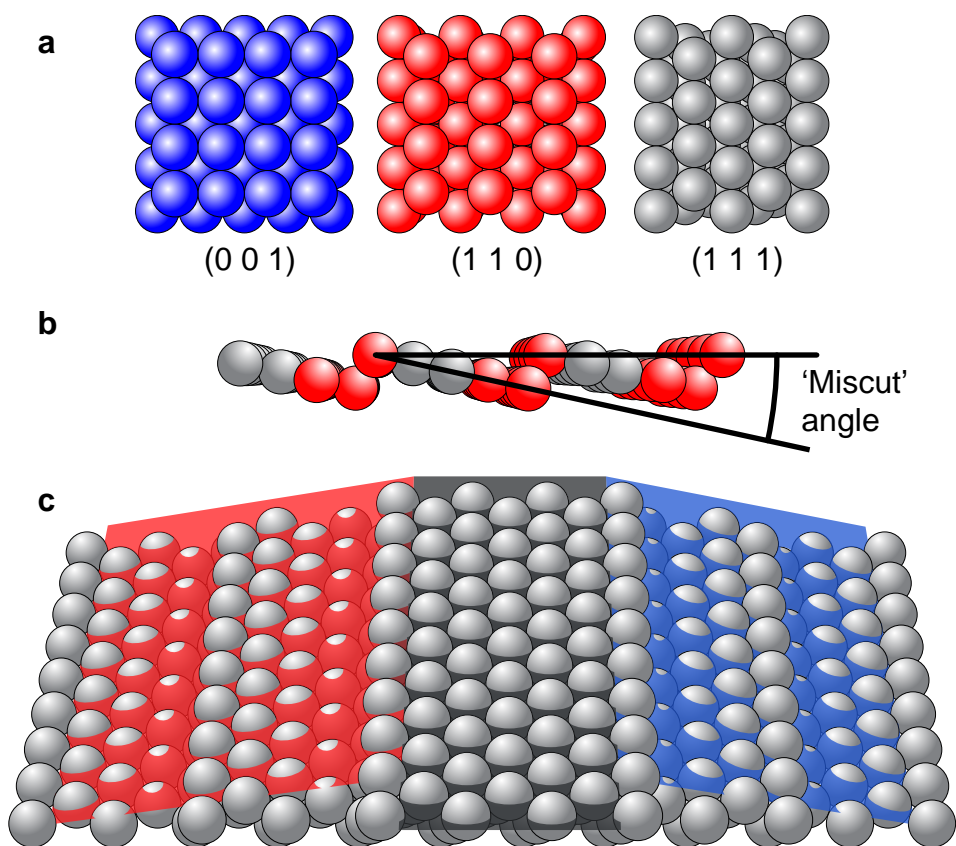


**Figure 1.3:** a) Low Miller index surfaces for face-centered cubic crystals. b) High Miller index surfaces can be exposed by cutting the single crystal at an angle with respect to the low Miller index surface, shown here for the (5 5 3) that occurs at approximately  $12.3^\circ$  with (1 1 1). c) Illustration how a curved surface exposes surfaces that vary from (5 5 3) along (1 1 1) to (3 3 5).

which may take months of sputtering-annealing cycles; and differences in absolute temperature measurement resulting from minor variations in thermocouple connections. Some problems can be overcome. Repetitive breaking of UHV conditions can be eliminated through the use of a load-lock system, but exchangeable sample mechanisms usually compromise heating and/or cooling efficiency. The effect of different impurities between crystals can be removed (at least in part) by cutting all samples from the same single crystal boule. However, the expense and time necessary to work with multiple individual crystals remains. In our experience, the experimental time requirement is proportional to the number of surfaces studied.

An alternative to this traditional surface science method of studying the influence of steps is to use a curved surface. Various shapes have been utilized, including fully cylindrical crystals, which exhibit at least two regions of each low Miller index structure on their circumference;[30–32] and dome-shaped crystals, which also include kinked step edges.[33, 34] For a nickel cylinder with its rotational axis along  $(1\ 0\ \bar{1})$ , we found mostly smooth variations in step density between the three low Miller index surfaces  $(0\ 0\ 1)$ ,  $(1\ 1\ 1)$  and  $(1\ 1\ 0)$ . [35] In contrast, faceting of high Miller index planes was observed on a cylindrical Pt crystal oriented with its rotational axis along  $(0\ 0\ 1)$ . [32] Limitations of working with a full cylindrical crystal include the thermal inertia of a large sample, and the difficulty of adapting sample holders to this shape. A compromise solution is to fashion a section of curved crystal into the approximate size and shape of a typical flat sample. Although the range of surface structures available on such a partial section is more limited, such crystals have been employed successfully in standard UHV systems.[36, 37] In these cases, they expose surfaces ranging from  $(5\ 5\ 3)$  along  $(1\ 1\ 1)$  to  $(3\ 3\ 5)$ , as indicated in figure 1.3c. Generally, the direction of curvature is chosen such that the curvature results from atomically straight step edges. Dome-shaped crystals offer a continuous range of surface structures, including straight and kinked step edges. Cu crystals were employed in studies of surface structure and chemical reactivity[33, 34]. Spherical single crystals were also employed in electrochemistry to resolve the roughening of Pt electrodes upon scanning

to oxidative potentials.[38]

Studies employing curved single crystal surfaces require experimental techniques with sufficient spatial resolution; a detail that is generally unimportant with macroscopically flat surfaces. Various techniques have been applied to study the continuously varying surface structure with high spatial resolution. Early studies employed Low Energy Electron Diffraction (LEED),[35, 39] Auger Electron Spectroscopy[40, 41] and Photoelectron emission microscopy.[32] More recently Scanning Tunneling Microscopy[36, 42, 43] and probes using electromagnetic radiation, e.g., Angle Resolved Photoemission Spectroscopy,[42, 44] and X-ray Photoelectron Spectroscopy (XPS),[36] have been shown to be applicable with high spatial resolution. These techniques mostly probe the chemical identity, oxidation state, and electronic states of the surface and its adsorbates. The dynamics of chemical processes were studied using supersonic molecular beams. In this way, the King and Wells technique was used to determine the absolute probability of molecular and dissociative adsorption as a function of incidence angle and kinetic energy.[30] Also, spatially-resolved temperature programmed desorption has demonstrated differences in the desorption of  $\text{H}_2\text{O}$  from different step types of a curved  $\text{Ag}(1\ 1\ 1)$  single crystal.[37] Planar Laser-Induced Fluorescence showed that light-off temperatures for CO oxidation on a curved  $\text{Pd}(1\ 1\ 1)$  sample are lower at  $\{1\ 1\ 0\}$  steps than  $\{0\ 0\ 1\}$  steps.[45]

How defects influence reactivity is actively studied to this day.[27, 46–48] Platinum is one of the best catalysts for oxidation reactions. It is used for hydrogen oxidation in fuel cell applications, but also for CO oxidation in the three-way car catalyst. Throughout this thesis, we study processes relevant to these two applications using stepped surfaces. We use both curved and traditional flat single crystal surfaces to study how defects influence reactivity in surface reactions relevant to hydrogen fuel cells. We systematically unravel mechanistic details by studying the catalytic steps individually. In chapter 3, we elucidate how defect density and defect type affect initial hydrogen dissociation. Dissociation occurs at the site of im-

pact and does not require a highly mobile precursor. For the first time to our knowledge, we extract site-specific reaction cross sections for the  $\{0\ 0\ 1\}$  and  $\{1\ 1\ 0\}$  steps. The  $\{1\ 1\ 0\}$  step type has a larger reaction cross section than the  $\{0\ 0\ 1\}$  step type. In chapter 4, we show that while defects increase reactivity, they lower selectivity in isotopic scrambling of dihydrogen. We attribute this to poor diffusive mixing at steps. In chapter 5 we show using two molecular beams that  $\{1\ 1\ 0\}$  steps are also more reactive in oxygen reduction than  $\{0\ 0\ 1\}$ . This is a result of both higher  $O_2$  and higher  $H_2$  sticking. In chapter 6, we adapt reflection absorption infrared spectroscopy so it may be applied to curved single crystal surfaces. We then use this technique to study CO adsorption on platinum as proof of principle. Finally, we present an outlook in chapter 7. There, we describe the spectroscopy of  $CO_2$ . Throughout this thesis work, we developed an optical excitation setup to prepare  $CO_2$  in a vibrationally excited state for state-resolved  $CO_2$  dissociation experiments. We present initial characterization of the optical setup and  $CO_2$  excitation in the supersonic molecular beam.

This thesis deals with results obtained using two ultrahigh vacuum machines: Lionfish and Boxfish. We provide a general description of the two machines. Chapter 6 details how reflection absorption infrared spectroscopy is performed at curved single crystal surfaces using Boxfish. Lionfish is described in much more detail in this chapter. In addition, our experiments involving reactions at curved surfaces benefit from proper molecular beam characterization. We have taken steps in measuring the flux and shape of the supersonic molecular beam at the sample using a stagnation tube. We present our findings and analysis in this chapter.

## Curved single crystals

As described in chapter 1, catalytic activity in heterogeneous catalysis is often promoted by step edges. However, the exact role of step edges and terraces in catalytic processes is still debated in literature. Studies are still undertaken to unravel the fundamental processes that underlie catalytic reactions.

The general surface science approach uses macroscopically flat single crystal surfaces. A single crystal is grown and subsequently cut to expose a low Miller index surface. These low Miller index surfaces contain predominantly the (0 0 1), (1 1 0), or (1 1 1) facet. However, small mis-cuts will also introduce defects in the form of step edges and kinks. As a result, terraces on typical low miller index surfaces are on the order of several hundred nm wide. The influence of defects is usually studied using regularly stepped surfaces.[29, 49] Regularly stepped surfaces are produced by cutting the single crystal at an angle with respect to a low Miller index plane. In this way, specific terrace widths can be selected by choosing specific angles.[50] Studying the influence of terrace width or step density generally involves using multiple single crystals.

A variation on this approach is the use of curved single crystal surfaces. The crystal is then cut as (a section of) a cylinder[32] instead of a macroscopically flat disk. The angle with low miller index surfaces can be varied smoothly by following the curvature of the crystal, exposing a plethora of surface structures. The crystals used throughout this thesis are cut such that a low miller index surface is located at the apex of the curved surface. The  $31^\circ$  macroscopic curvature of the surface results in monatomic step edges and, as such, the step density varies smoothly from approximately  $0.001 \text{ nm}^{-1}$  at the apex to  $1 \text{ nm}^{-1}$  at the sides. For face centered cubic crystals, such as our platinum sample, the (1 1 1) surface separates stepped surfaces containing {0 0 1} steps on one half of the sample and {1 1 0} on the other half. The surface structure then varies from Pt(3 3 5) on one side, to Pt(1 1 1) at the apex, and Pt(5 5 3) on the other side.

The curved platinum crystal (Surface Preparation Lab) is similar to a curved Ag(1 1 1) crystal described previously.[37] The sample can be pictured as a thin circular section normal to the axis of a complete cylinder; this parent cylinder has its axis in the  $[1 \bar{1} 0]$  direction and a radius of  $r = 15.0$  mm. The section is 8 mm in diameter, therefore it encloses  $31^\circ$  of cylindrical azimuth, chosen such that the apex is a (1 1 1) plane of the FCC structure of bulk Pt. The curvature is created by spark erosion and sanding, after which the surface is polished in an automated, custom-built polishing machine (Surface Preparation Lab). The curvature of the crystal imposes a gradual increase in monatomic step density[36] as a function of azimuthal distance from the apex. The (1 1 1) terraces are separated by  $\{0\ 0\ 1\}$  (A-type) steps on one half of the crystal, and  $\{1\ 1\ 0\}$  (B-type) steps on the other half. The separation of the two step types is verified using temperature programmed desorption.[51] Thus the crystal encompasses surface structures ranging from Pt(3 3 5) at  $-14.4^\circ$  to Pt(5 5 3) at  $+12.3^\circ$ . The curved single crystal is mounted in a 10 mm square tantalum holder that is encased in Pt foil to prevent tantalum contamination.

Microscopic techniques, such as scanning tunneling microscopy (STM), sample a small surface area of the crystal on the order of  $2 \times 2\ \mu\text{m}^2$ . With such high spatial resolution, it is quite straightforward to disentangle contributions by terraces and step edges. This is not possible for macroscopic techniques – terraces and steps are sampled simultaneously. This is also true for macroscopic techniques used on flat single crystal surfaces due to inevitable miscuts.

All techniques used throughout this thesis are macroscopic and convolute over a range of surface structures along the curved surface. The electron beam used in LEED probes a diameter ( $\phi$ ) or area (step density) of  $\sim \phi = 1\text{ mm}$  ( $\pm 0.15\text{ nm}^{-1}$ , chapter 6) or  $\sim \phi = 0.35\text{ mm}$  ( $\pm 0.05\text{ nm}^{-1}$ , chapters 3 and 4). The focused IR beam used for RAIRS in chapter 6 creates an approximately 6 mm long oval at the surface with FWHM  $\sim 0.72\text{ mm}$  ( $\pm 0.11\text{ nm}^{-1}$ ). The supersonic beam is skimmed to a rectangle of  $0.5 \times 6.4\text{ mm}^2$  ( $\pm 0.07\text{ nm}^{-1}$ , chapter 4) or  $0.135 \times 6\text{ mm}^2$  ( $\pm 0.02\text{ nm}^{-1}$ ,

chapters 3 and 4). Limiting the footprint of experimental techniques also limits the convolution over different surface structures. However, it generally reduces the signal-to-noise ratio as well. Signal averaging becomes crucial in the molecular beam experiments. The signal averaging method used throughout this thesis for King and Wells experiments is described in more detail in chapter 2.

### Boxfish

Boxfish is the ultrahigh vacuum (UHV) apparatus used in chapter 6. It is a UHV chamber with a base pressure of  $2 \times 10^{-10}$  mbar. It is equipped with a LEED/Auger system (VG, RVL - 900), a quadrupole mass spectrometer (Pfeiffer, QMA 200), a sputter gun (IS40C1, PreVac), and an external Fourier transform infrared spectrometer (Bruker, Vertex 70) for RAIRS.

The crystal holder is suspended from a bath-type liquid nitrogen cryostat on a x, y, z,  $\phi$  manipulator. The liquid nitrogen level is kept at approximately 50% to avoid contraction or expansion of the cold finger and consequential motion of the sample. The sample holder is electrically isolated from the cryostat and the rest of the machine by AlN plates. The crystal is heated by radiative heating and electron bombardment using a commercial filament (Osram, 150 W). High temperatures ( $> 600$  K) are achieved by applying a positive bias to the crystal. The curved Pt surface is cleaned through multiple cycles of  $\text{Ar}^+$  sputtering (Messer, 5.0; 400 K;  $0.5 \mu\text{A}$ ;  $45^\circ$ ; 10 min; 0.25 kV), followed by  $\text{O}_2$  treatment (Messer, 5.0;  $3.5 \cdot 10^{-8}$  mbar; 900 K; 3 min) and *in vacuo* annealing (1200 K; 3 min). Three cleaning cycles were performed every day prior to experiments. The surface structure was verified using LEED. (Chapter 6) The sample was annealed for 3 min at 1200 K between individual measurements to ensure the quality of the surface.



## Lionfish

Lionfish is the UHV apparatus used in chapters 3, 4, and 5. It has a base pressure of  $< 1.0 \cdot 10^{-10}$  mbar. The main feature of this apparatus are the two molecular beams; a double differentially pumped supersonic molecular beam (SSB), and a single differentially pumped effusive beam (EB). The molecular beams cross at  $45^\circ$  at the sample. Additionally, the apparatus contains: a four-grid MCP LEED/Auger (BLD800IR, OCI Vacuum Micro-engineering), a quadrupole mass spectrometer (QMA 200, Pfeiffer vacuum), and a quadrupole mass spectrometer (UTI-100C) that can be translated along the SSB axis for time of flight spectroscopy (TOF).

Single crystal samples are mounted on a x, y, z,  $\phi$  manipulator. The sample temperature is measured using a K-type thermocouple. The crystal is cooled using a bath liquid nitrogen cryostat and heated via radiative heating and electron bombardment by a tungsten filament (Osram). A bias potential can be applied to the sample or the filament to increase the electron bombardment efficiency so that the required temperatures can be reached. The curved Pt surfaces are cleaned by Ar sputtering ( $6 \cdot 10^{-6}$  mbar, Messer 5.0,  $45^\circ$ , 900 K, 0.5 kV, 1  $\mu$ A), O<sub>2</sub> annealing (900 K,  $3 \cdot 10^{-8}$  mbar, Messer 5.0) and 1200 K *in vacuo* annealing. For the final cleaning cycle, O<sub>2</sub> annealing and 1200 K annealing are replaced by 900 K *in vacuo* annealing to avoid O<sub>2</sub> induced step doubling or high temperature induced faceting.

## Supersonic molecular beam

Supersonic molecular beams are a powerful tool for studying gas-surface dynamics. The supersonic expansion results in cooling of molecules in the molecular beam, thereby narrowing translational and rotational distributions. Vibrational cooling is inefficient. In contrast to translational and rotational energy, vibrational energy is generally too large to be dissipated through collisions. The kinetic energy of the molecular beam can be varied by seeding into lighter gases, anti-seeding into heavier gases, or by vary-

ing the expansion temperature. Additionally, the internal energy increases only with expansion temperature or optical excitation (chapter 7).

A cut-through of the supersonic molecular beam (SSB) is shown in figure 2.1. The supersonic molecular beam consists of three differentially pumped stages – the source chamber (SSB1, green), first differentially pumped stage (SSB2, blue), and the second differentially pumped stage (SSB3, red) – attached to the main chamber (orange). The molecular beam is formed in the source chamber by expanding a constant flow of gas from a tungsten nozzle with a 28  $\mu\text{m}$  laser drilled orifice. The nozzle temperature is measured using a C-type thermocouple laser welded to the nozzle. The temperature of the nozzle can be controlled by radiative heating; a ring surrounding the nozzle can be heated through electron bombardment by two filaments (Osram). Heat shields protect the rest of the system from warming up. A skimmer (diameter  $\phi = 0.45$  mm) separating SSB1 and SSB2 selects the coldest part of the expansion.

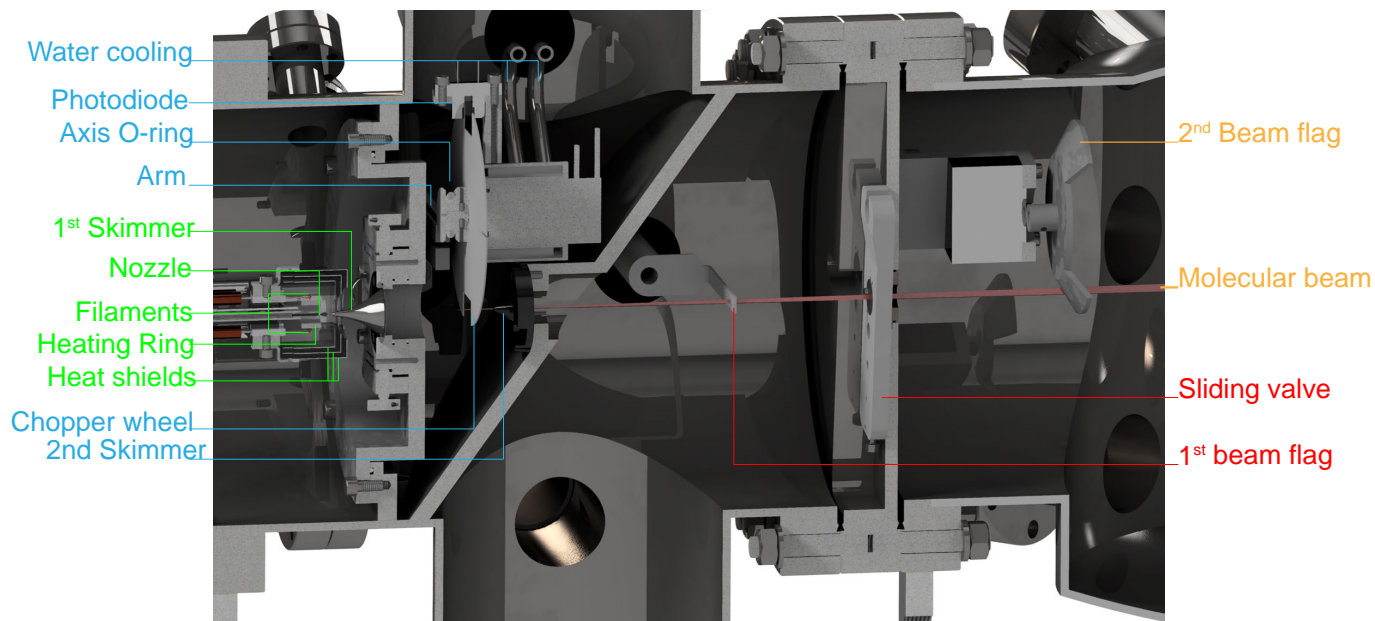


**Figure 2.1:** A cut-through of the supersonic molecular beam showing its various parts in the source chamber (SSB1, green), first differentially pumped stage (SSB2, blue), second differentially pumped stage (SSB3, red), and main chamber (orange).

SSB2 contains a water-cooled brushless motor (2444 S 024 B, Faulhaber). It chops the molecular beam for TOF or reduces the number of molecules striking the surface by its duty cycle(16%). The chopper wheel contains two 0.85 mm and two 17 mm slots chopping the beam at a radius of approximately 56.0 mm. The chopper frequency is measured with an optical sensor (TCSS 2100). The chopper can be opened by translating a stainless steel arm onto the axis O-ring while monitoring the pressure in the second differentially pumped stage. A second skimmer ( $\phi = 2.5$  mm) separates the SSB2 from SSB3.

The second differentially pumped section contains a stainless steel beam flag used for King and Wells experiments. The flag is operated through a Labview controlled solenoid valve. The molecular beam is shaped by one of four different orifices:  $\phi = 1.8$  mm (chapter 5), 3.2 mm, 6.2 mm, and a slit). Throughout this thesis, two different slit sizes are used:  $0.25 \times 3$  mm<sup>2</sup> (chapter 4) and  $0.065 \times 3$  mm<sup>2</sup> (chapters 3 and 4). The orifice is selected with the sliding valve separating SSB3 from the main chamber.

As the molecular beam enters the main chamber, it can be interrupted prior to impinging upon the crystal using a second beam flag. This beam flag is driven by a UHV compatible stepper motor (C14.1, Arun Microelectronics Ltd). The beam flag is operated manually (chapter 5) or by sending commands to the stepper motor controller (SMD210, Arun Microelectronics Ltd) with labview (chapters 3 and 4). With the flag opened, the molecular beam is free to impact the surface or, when the crystal is translated out of the molecular beam path, fly into the on-axis mass spectrometer for time of flight spectroscopy.

### **Forming a supersonic molecular beam**

Three flow controllers (Bronkhorst) feed the supersonic beam with gases. The thermal mass flow controllers (MFC) use the thermal conductivity of gases to measure and then regulate the flow using a control valve. These

flow controllers are calibrated for  $\text{N}_2$  flow but can be corrected for different gases using the Bronkhorst developed FLUIDAT<sup>®</sup> website.

A gas mixture is created using the flow controllers. The supersonic beam is formed by expanding this gas mixture from the tungsten nozzle into the source chamber. The pressure inside the nozzle – measured with a capacitance manometer (MKS, 750C14MC02GA) – stabilizes after some time. Figure 2.2 shows that the equilibrated nozzle pressure is proportional with flow, but that the expansion is gas specific (the pressure drop over a tube has a viscosity dependence).

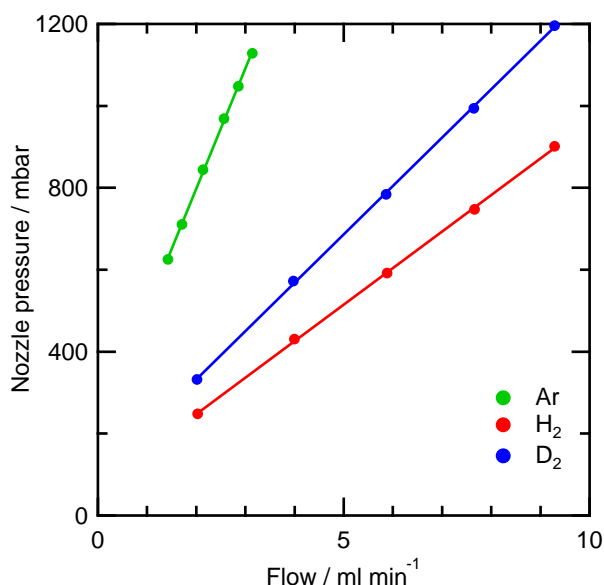


**Figure 2.2:** Nozzle pressure dependence on flow for pure Ar,  $\text{D}_2$ , and  $\text{H}_2$  expansions.

The flows shown in figure 2.2 are significantly smaller than the available range of the flow controllers (10, 20, and 50 ml min<sup>-1</sup>). The flow (or nozzle pressure) available is limited by the pressure in the source chamber and its fore-vacuum pump. The flow out of the nozzle orifice depends on the nozzle pressure, gas type, and orifice diameter. Since the pressure inside the nozzle

takes time to stabilize, the flow into the source chamber also takes time to stabilize. As a result, it takes some time for the source chamber pressure to equilibrate. SSB1, SSB2, and SSB3 are each pumped by a turbo molecular pump (TMU 521P, Pfeiffer Vacuum; HiPace 300, Pfeiffer Vacuum; TMU 261P, Pfeiffer Vacuum), each backed by a rotary vane pump (DUO 30A, Pfeiffer Vacuum; 2010, Alcatel; E2M5, Edwards). The pressures in SSB1 and SSB3 are measured using a cold cathode pressure gauge (IKR 270, Pfeiffer Vacuum), while the pressure in SSB2 is measured using a full range pressure gauge (PKR 251).

The pressures inside the source and differentially pumped chambers are shown in figure 2.3. The equilibrium pressure in the source chamber is dominated by the flow from the nozzle, the average molecular mass of the gas inside the nozzle, and the pumping speed of the turbo molecular pump. The observed non-linear behavior is likely due to the increased fore-vacuum pressure, which were not actively monitored during these experiments. In contrast, the pressure in both SSB2 and SSB3 is approximately linear with the flows and nozzle pressures used here. The gas load on the pumps is much smaller and pressure build up at the back of the turbo molecular pump is not an issue for SSB2 and SSB3.

## **Flux measurement**

The pressures in the supersonic molecular beam are important parameters for starting experiments. More important for experimental conditions are the flux and footprint of the molecular beam at the surface. Both are measured by exchanging the sample manipulator with a stagnation tube. The stagnation tube is schematically shown in figure 2.4. A  $\phi = 6$  mm tube is suspended from a x, y, z manipulator. At the crystal position, a 1 mm hole is drilled into the tube, after which the area around the orifice is milled to a wall thickness of  $\sim 0.3$  mm. The tube has a  $45^\circ$  plate behind orifice so that molecules flying through the orifice scatter into the tube. A calibrated pressure gauge (Series 370 stabil-ion, Granville-Phillips) is mounted to the tube on an elbow at the top of the manipulator. The

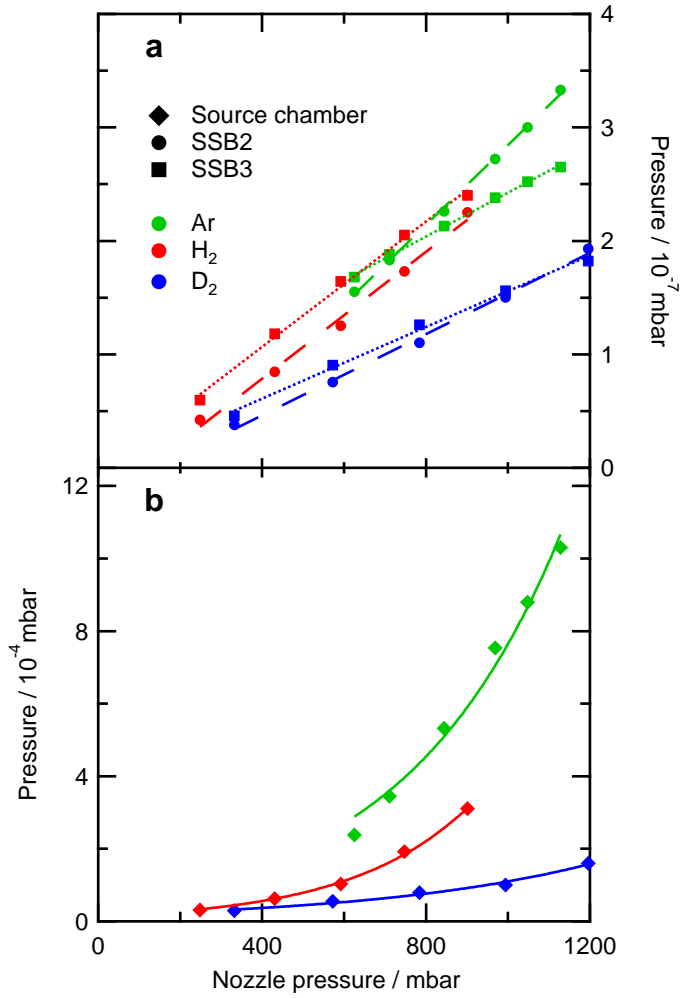


**Figure 2.3:** The pressure dependence of the source and differentially pumped stages on the nozzle pressure for Ar, D<sub>2</sub>, and H<sub>2</sub> flows shown in Figure 2.2.

elbow reduces both the error in the volume and the stagnation tube base pressure.

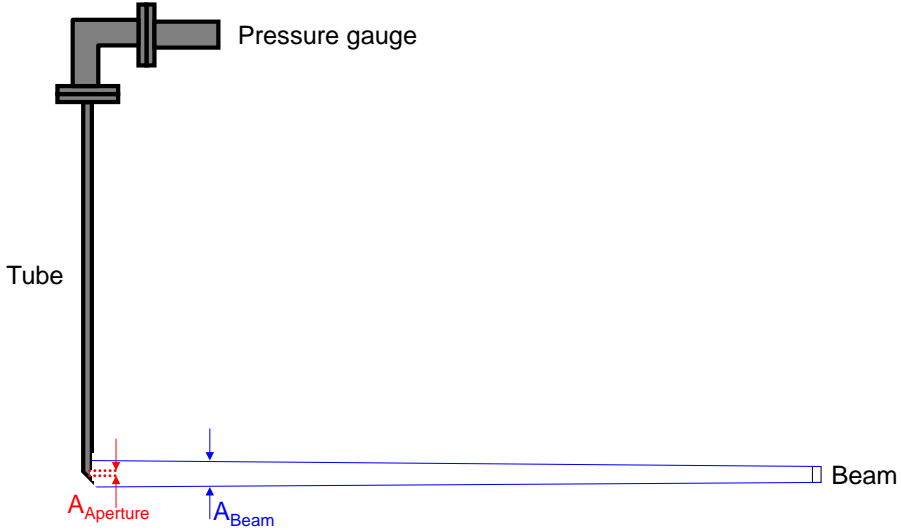


**Figure 2.4:** Schematic view of the stagnation tube used to measure the flux and shape of the beam.

We start with measuring the flux of the molecular beam, before determining its footprint. Prior to the beam being incident on the orifice, an equilibrium is set such that:

$$\frac{dn}{dt} = 0 \quad (2.1)$$

where  $n$  is the number of molecules. The initial pressure is governed by constant contributions: outgassing of the stagnation tube walls, residual gas molecules from the main chamber flying effusively into the stagnation tube, and molecules flying effusively out of the stagnation tube. Molecules flying effusively through an orifice is described by the collision rate with the area of the orifice. As such, when the molecular beam overlaps with the orifice, the equilibrium is disturbed by an instantaneous increase of  $\Phi_{in}$  with the flux of the molecular beam,  $\Phi_{beam}$ :

$$\frac{dn}{dt} = (\Phi_{in} - \Phi_{out}) A = (\Phi_{beam} - Z_W) A \quad (2.2)$$



where  $Z_W$  is the collision rate in *molecules*  $m^{-2} s^{-1}$ . The change in the number of molecules can be rewritten to a change in pressure and expressed as function of the collision rate:

$$\frac{dP}{dt} = \left( \Phi_{beam} - \frac{P}{\sqrt{2\pi \frac{M}{N_A} k_B T}} \right) A \frac{k_B T}{V} \quad (2.3)$$

We now rewrite the right hand brackets in order to change the expression into a standard integral:

$$\frac{dP}{dt} = \left( 1 - \frac{P}{\Phi_{beam} \sqrt{2\pi \frac{M}{N_A} k_B T}} \right) \Phi_{beam} A \frac{k_B T}{V} \quad (2.4)$$

The integral can then be set up:

$$\int_0^P \frac{1}{1 - \frac{P}{\Phi_{beam} \sqrt{2\pi \frac{M}{N_A} k_B T}}} dP = \int_0^t \Phi_{beam} A \frac{k_B T}{V} dt \quad (2.5)$$

and is solved using the standard integral:

$$\int \frac{1}{b + ax} = \frac{1}{a} \ln|ax + b| \quad (2.6)$$

It results in the following expression:

$$-\Phi_{beam} \sqrt{2\pi \frac{M}{N_A} k_B T} \ln \left| 1 - \frac{P}{\Phi_{beam} \sqrt{2\pi \frac{M}{N_A} k_B T}} \right| = \Phi_{beam} A \frac{k_B T}{V} t \quad (2.7)$$

Isolating P results in:

$$P = \Phi_{beam} \sqrt{2\pi \frac{M}{N_A} k_B T} \left( 1 - e^{\left( -\frac{A \frac{k_B T}{V}}{\sqrt{2\pi \frac{M}{N_A} k_B T}} t \right)} \right) \quad (2.8)$$

In the limit of large t, the pressure in the stagnation tube is then a function of  $\Phi_{beam}$  in the following way:

$$P = \Phi_{beam} \sqrt{2\pi \frac{M}{N_A} k_B T} \quad (2.9)$$

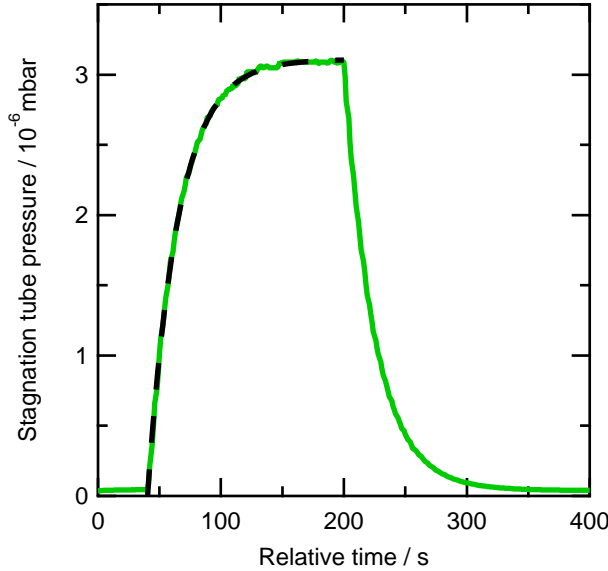


**Figure 2.5:** The pressure inside the stagnation tube as a function of time. The beam is opened to the main chamber at  $t = 0$ . At  $t = 40$  s, the flag inside the main chamber is opened so that the beam directly impinges unto the orifice into the stagnation tube. After impinging for 160 s, the beam is switched off causing the pressure to drop. The black dashed line is a exponential fit to the data.

Figure 2.5 shows an example of the recorded data for an Ar beam. The pressure measured with the calibrated pressure gauge is recorded from the analog controller output using Labview. The data is fitted with a general fit function based on equation 2.8 (dashed black line) to extract the stagnation pressure. The beam flux is calculated from the stagnation pressure using equation 2.9.

The calculated flux for different flows of Ar,  $H_2$ , and  $D_2$  beams are presented in figure 2.6. The flux for the three different gases show a linear dependence over the range measured. Unfortunately, the flux for mixed beams cannot be determined through extrapolation of the pure beams. These may be determined by repeating the experiments outlined here, but starting from a mixed beam and varying the flow of one of the constituents

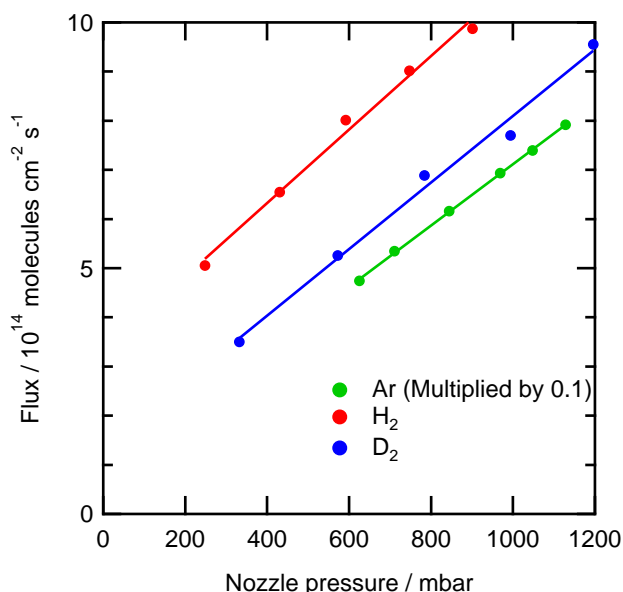


**Figure 2.6:** Flux dependence on nozzle pressure for Ar,  $\text{D}_2$ , and  $\text{H}_2$  beams shown in figure 2.2. Note that the flux from the Ar beam is multiplied by 0.1.

at a time. These results present a reasonable estimate for beam fluxes used throughout this thesis.

## Beam profile

Throughout this thesis, the molecular beam is combined with curved single crystal surfaces to study the effect of step density on dissociation and catalytic activity. The footprint of the molecular beam is a key experimental parameter due to surface structure convolutions, as detailed in chapter 2. The orifice between SSB3 and the main chamber controls the size and shape of the molecular beam.

This orifice can be varied using a sliding valve. The sliding valve contains a slit of  $3 \times 0.065 \text{ mm}^2$  (or  $0.25 \times 3 \text{ mm}^2$ ) and three circular orifices;  $\phi = 1.8 \text{ mm}$ ,  $3.2 \text{ mm}$ , and  $6.2 \text{ mm}$ . The size of the molecular beam at the surface can be estimated from the size and distance between the sliding

valve and first skimmer orifices, and extrapolating to the surface position. We assume that the first skimmer is the point source for the molecular beam. The skimmer-orifice and skimmer-sample distances are 202.5 mm and 398.3 mm, respectively. Using simple trigonometry, we calculate a beam diameter of 3.54 mm for the smallest orifice ( $\phi = 1.8$  mm).

Alternatively, the footprint of the beam can be measured with the stagnation tube setup shown in Figure 2.4. Similarly to the flux measurements, the orifice of the stagnation tube is placed at the crystal position. After aligning the orifice to the center of the beam, the 1 mm orifice is traced across the molecular beam normal to the propagation axis. The beam footprint has been measured for the two beam shapes mainly used throughout this thesis: the  $3 \times 0.065$  mm<sup>2</sup> slit and the 1.8 mm orifice. The experiments are performed similar to those shown in figure 2.5. An exponential fit is used to extract the stagnation pressure. The results are normalized to the maximum pressure, where the molecular beam completely covers the stagnation tube orifice.

The results for the circular orifice are shown in figure 2.7. As the orifice is translated into the beam, the pressure rises quickly until a plateau is reached where the orifice is smaller than the molecular beam. The beam pressure shows a stable value over the range where the orifice is completely overlapped by the beam. The overlap can be calculated using the standard math problem of calculating the overlap between two circles.[52] The general solution for the overlap is shown in equation 2.10.

$$\begin{aligned}
 A_{st \text{ sector}} &= r_{st} \cdot \text{acos} \left( \frac{d^2 + r_{st}^2 - r_b^2}{2 \cdot d \cdot r_{st}} \right) \\
 A_{b \text{ sector}} &= r_b \cdot \text{acos} \left( \frac{d^2 + r_b^2 - r_{st}^2}{2 \cdot d \cdot r_{st}} \right) \\
 A_{correction} &= \frac{1}{2} \sqrt{(-d + r_{st} + r_b)(d + r_{st} - r_b)(d - r_{st} + r_b)(d + r_{st} + r_b)} \\
 A_{overlap} &= A_{st \text{ sector}} + A_{b \text{ sector}} - A_{correction}
 \end{aligned} \tag{2.10}$$

where  $r_{st}$  and  $r_b$  are respectively the radius of the stagnation tube orifice and the radius of the molecular beam, while  $d$  is the distance between the

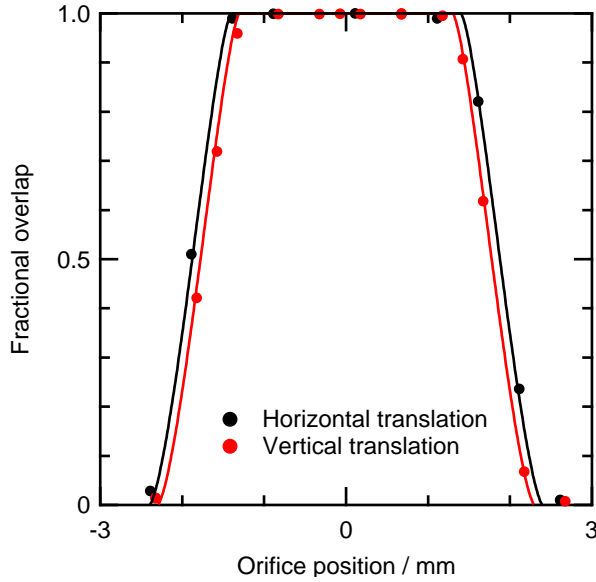


**Figure 2.7:** Beam profile experiment of a molecular beam shaped with the 1.8 mm diameter orifice. The beam profile is shown as the fractional overlap of the stagnation tube orifice with the molecular beam as a function of on-axis horizontal and vertical displacement. Solid lines are simulated data using the Igor procedure in appendix A. There, a beam radius of 1.9 mm and 1.8 mm are used for respectively horizontal and vertical translation impinging onto a 0.5 mm radius orifice.

center of the two circles. Using the Igor procedure in Appendix A, the overlap is calculated numerically. A few logic operators are included in the procedure to account for either circle being smaller than the other. The results are shown in figure 2.7. The calculated overlap agrees well with the measured data, but suggest that the molecular beam may be slightly elliptical. A slight misalignment could have caused the orifice to be translated off-center with respect to the molecular beam producing the same result. The results suggest that the molecular beam has a 3.8 mm diameter as it impinges onto the surface.

A similar analysis is applied to a beam shaped by a slit aperture translates over the stagnation tube orifice. The overlap is calculated by summing

the area of all different sections when the rectangular beam overlaps the circular orifice. The procedure used to calculate the overlap for vertical and horizontal translation can be found in Appendix A.

Experimental results are shown with simulated beam profiles in figure 2.8. Spread in the horizontal translation data is caused by hysteresis in the x-y manipulator. The calculated overlap shows that the footprint of the molecular beam at the sample is  $6.0 \times 0.126 \text{ mm}^2$ .

The beam size we report here are somewhat larger than suggested by the calculated 3.54 mm. They are even larger than 3.0 mm reported by Cao.[53] However, the previous results are too narrow for the reported data; the simulated line falls well between the data and easily explains part of the discrepancy ( $\sim 0.5 \text{ mm}$ ). While presumably not essential to their simulated results, the reported orifice sizes are also incorrect. A smaller discrepancy may also stem from the stagnation tube orifice either not being symmetric or having a diameter somewhat smaller than 1 mm. We have not verified the orifice shape after identifying the discrepancy with the previous data and calculated results.

### **Experimental techniques**

A number of experimental techniques are applied throughout this thesis. We now provide a basic description for the most important techniques, starting with a description of LEED and RAIRS as used on Boxfish for chapter 6. Thereafter, we provide a description of time of flight, our analysis thereof, and finish with a description of the King and Wells technique used for measuring sticking probabilities.

### **Low energy electron diffraction**

Low energy electron diffraction (LEED) is used throughout this thesis to verify the structure of the single crystal surfaces. A generic 3-grid LEED is shown in figure 2.9. In LEED, an electron gun sends a beam of electrons at the surface. The sample is placed in both the focus of the electron beam

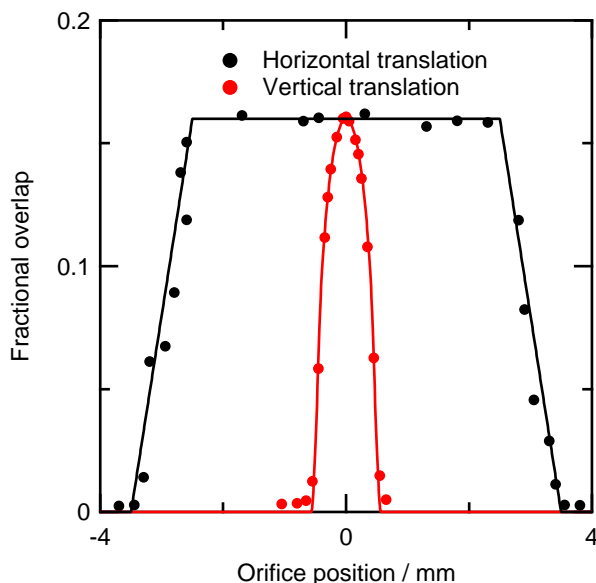


**Figure 2.8:** Beam profile results for a molecular beam shaped with a  $0.065 \times 3$  mm slit orifice. The beam profile is the fractional overlap of the stagnation tube orifice with the molecular beam as a function of horizontal and vertical displacement. Solid lines are simulated with Igor procedures in appendix A and A. There, the molecular beam is a  $6.0 \times 0.126$  mm rectangle impinging onto a 0.5 mm radius orifice.

and the origin of the three (or four) concentric spherical grids. Electrons may scatter elastically or inelastically from the surface. The grids filter out inelastically scattered electrons, while elastically scattered electrons pass through to hit a phosphorescent screen. They show up as green dots, which form a diffraction pattern. From the resulting pattern the average surface structure can be derived. Regularly stepped surfaces cause an additional splitting in the diffraction pattern by introducing an additional diffraction grating, such as shown in figure 1.3b.

### Reflection absorption infrared spectroscopy

Reflection Absorption Infrared Spectroscopy (RAIRS) is the characteristic technique used on Boxfish. Surface vibrational spectroscopic methods are powerful techniques for identifying adsorbates, but RAIRS can also be

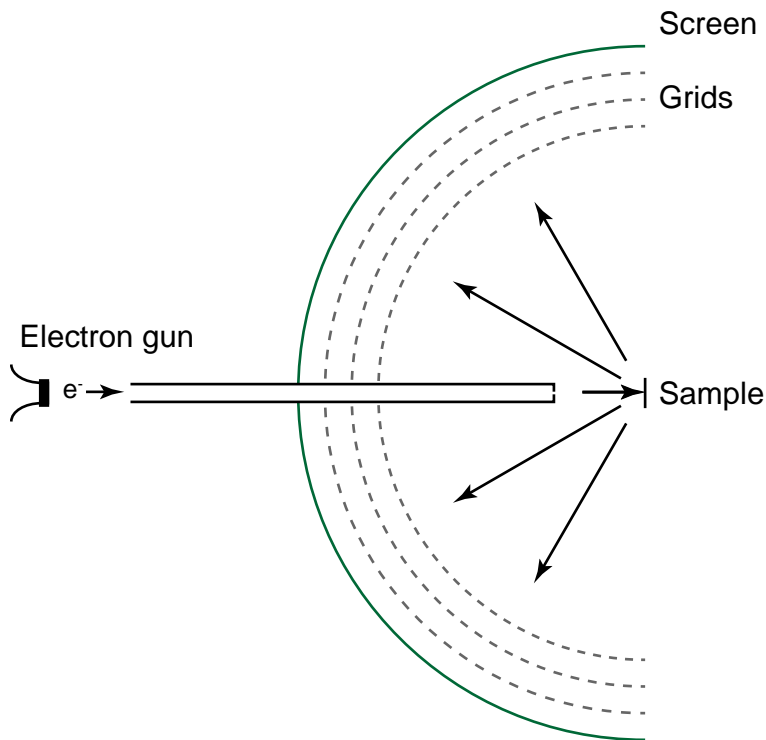


**Figure 2.9:** Schematic overview of a generic 3-grid low energy electronic optic.

used to extract details, e.g. on interactions between adsorbates or surface binding sites.

RAIRS is a spectroscopic technique which works in the infrared region. To describe how RAIRS works, it is convenient to describe infrared radiation as a wave with an electric and magnetic field vector. Molecules can absorb infrared radiation if the electric field of the infrared radiation resonates with the electric field of the transition dipole. Infrared absorption increases with the overlap between the electric field of the infrared radiation and the transition dipole moment. Absorption of infrared radiation by molecules leads to excitation of molecular vibrations. In order to excite a vibration in the molecule, there has to be a change in the dipole moment. This is the selection rule for infrared absorption.



When a dipole is adsorbed to a conducting surface, the surface creates a mirror image of the dipole through its electrons. Depending on the orientation of the dipole, this either cancels or doubles the effective dipole moment. The dipole moment of molecules adsorbed perpendicular to the surface is doubled, while the dipole moment is canceled when adsorbed parallel to the surface. Combined with the selection rule, this means the dipole of molecules adsorbed parallel to the surface do not absorb infrared radiation.

Only molecules with a dipole perpendicular to the surface absorb infrared radiation. The electric field vector of infrared radiation needs to have as much overlap with the dipole moment as possible, which is achieved by using polarized radiation. The polarization angle is taken with respect to the surface normal where p stands for parallel and s stands for senkrecht (German for perpendicular). As dipoles are aligned perpendicular to the surface, all interaction with infrared radiation results from p-polarized light. RAIRS is performed in reflection. It is intuitive that the amount of p-polarized radiation is a function of the angle with the surface. If the angle with the surface is  $90^\circ$ , there will be no p-polarized radiation possible. If the angle with the surface is a grazing angle, then a large amount of radiation can be p-polarized and there is more absorption.

Infrared (IR) experiments are generally performed using a Fourier transform infrared (FTIR) spectrometer. Boxfish uses a Bruker Vertex 70 FTIR spectrometer. Inside the FTIR spectrometer a globar radiates IR radiation. This is combined with a Helium-Neon laser used as a reference. A tungsten filament is present as a white light source within the FTIR. It provides a visual indication of the IR beam for aligning purposes. A Michelson interferometer is used to create an interference pattern in the IR radiation beam, which is required for measuring the interferogram in FTIR. Using additional mirrors, the IR radiation is reflected out of the spectrometer, which is where our setup is different from a normal FTIR spectrometer.

After exiting the spectrometer, the beam of IR radiation is steered using two gold coated mirrors to the right height and angle of incidence for the off-axis parabolic mirrors. The gold coated parabolic mirror focuses the IR beam on the sample. Prior to reflection by the sample, the radiation is polarized by a thallium bromoiodide (KRS-5) wire grid polarizer and passes through a calcium fluoride UHV compatible window. The IR beam reflects off the sample, passes out of the UHV chamber through another calcium fluoride window and is collimated again by a second gold coated parabolic mirror that is identical to the previous mirror. Finally, a third gold coated parabolic mirror focuses the IR radiation onto a liquid nitrogen cooled mercury cadmium telluride (MCT) detector, which measures the interferogram. The IR spectrum is finally calculated by applying the Fourier transform and dividing the sample measurement with a reference measurement.

### **Time of flight**

Supersonic molecular beam techniques are a valuable tool in studying molecule-surface dynamics. As mentioned previously, supersonic molecular beam techniques give control over the kinetic energy through seeding and anti-seeding, or changing the expansion temperature. Although the kinetic energy distribution narrows from the expansion, it is critical to measure the kinetic energy distribution to account for remaining energy convolution effects in experiments. The velocity of molecules can be measured using Time of Flight spectroscopy (TOF). In TOF, the flight time of molecules traveling a known distance is measured.

As described before, Lionfish uses a continuous molecular beam. However, TOF requires it to be pulsed. The molecular beam is modulated with a mechanical chopper using two narrow and two broad slits. After some flight time, molecules cross the distance between the chopper wheel and the ionization region of the QMS. There, molecules are ionized, accelerated into the quadrupole, mass selected, and detected by a channeltron. The channeltron signal is amplified and pulses are counted using a multi-scalar

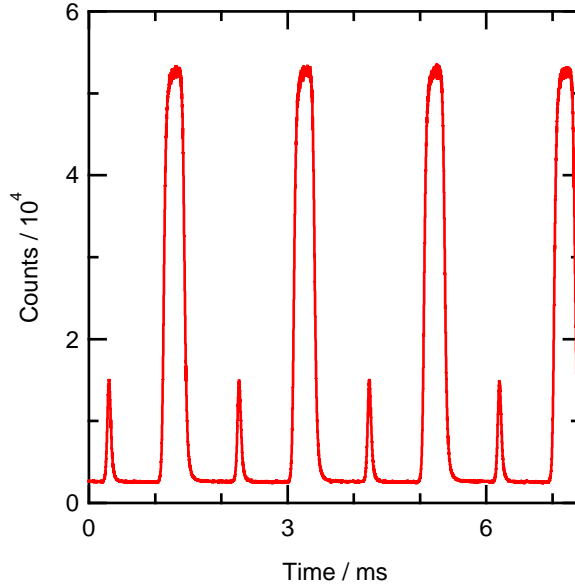


**Figure 2.10:** TOF spectrum of a pure D<sub>2</sub> supersonic beam.

card. The mass spectrometer measures for  $1\frac{7}{8}$  chopper periods. The optical sensor triggers the next pulse by detecting a slit. A number of these pulses are recorded and summed up, resulting in the typical TOF spectrum shown in figure 2.10.

The most basic way of analyzing TOF is by determining the flight time for various mass spectrometer positions. The most-probable flight time can be extracted by fitting the first small peak in the TOF spectra with a Gaussian function. The velocity,  $\frac{dy}{dt}$ , can be directly extracted from the distance dependent most-probable flight time.

Alternatively, if the distance from the chopper to the mass spectrometer is known, the time of flight spectra can be fitted. Fitting TOF spectra has the benefit that the velocity distribution can be extracted after deconvolving any broadening effects. The TOF signals are broadened by both the pulse length of the chopper and by the length of the ionization field of the TOF mass spectrometer.

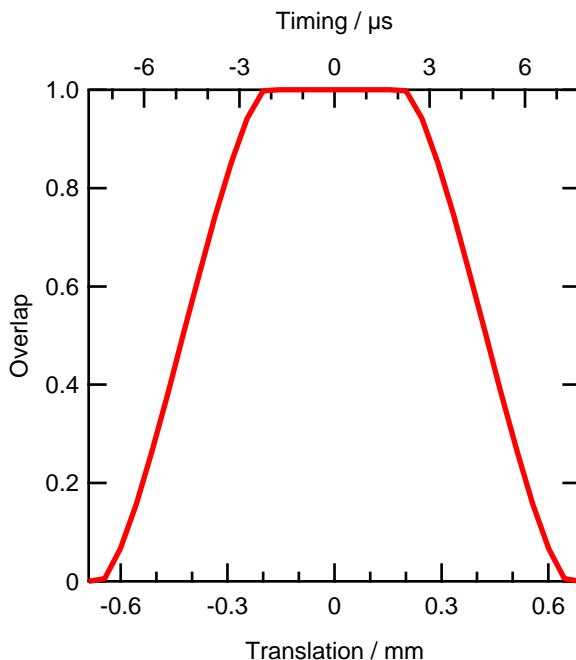


**Figure 2.11:** The gating function of the chopper results in a convolution.

Chopper convolution can be accounted for by broadening the fit function of the TOF spectra with the chopper gating function. We approximate the chopper slit rotating through the molecular beam by calculating the overlap of a rectangle passing over a circle, similar to the slit aperture beam profile experiments in chapter 2. Using the IGOR procedure in appendix A, the chopper gating function is calculated with the same time constant ( $0.5 \mu\text{s}$ ) as the recorded data. The resulting gating function is shown in figure 2.11. The fit function is generated with the IGOR procedure and includes the gating function weighted time broadening.

The TOF QMS has a 3 cm long ionization region, which is beneficial for the signal-to-noise ratio of the QMS. However, it causes extra broadening. As molecules fly into the 3 cm long ionization region of the mass spectrometer, ionization may occur anywhere along its length. As a result, the neutral flight path may vary with  $\pm 1.5 \text{ cm}$ . We are aware of this potential

broadening mechanism but disregard its influence in our analysis.

The functional form for a TOF spectrum measured using a density sensitive detector is:[54–56]

$$f(t) = \left(\frac{l}{t}\right)^4 \cdot e^{-\left(\frac{\frac{l}{t} - \frac{l}{t_0}}{\sqrt{\frac{2RT}{M}}}\right)^2} \quad (2.11)$$

with neutral flight path  $l$ , neutral flight time  $t$ , gas constant  $R$ , gas temperature  $T$ , and molecular mass  $M$ . The neutral flight time is measured by fitting multiple TOF spectra at different positions with Gaussian functions and extrapolating to  $l = 0$ . The fit function is weighted by convoluting the neutral flight time with the pulse width due to the chopper gating function.

After fitting, the TOF spectra can be deconvoluted for the chopper gating function by using the fit function. The time of flights are converted to the flux weighted distribution by dividing the fits by velocity  $v$ . [54] The fits are then redimensioned from neutral flight time to velocity and energy using the following transformations:

Velocity:

$$v = \frac{l}{t} \quad (2.12)$$

Signal as a function of velocity:

$$\begin{aligned} \int f(t) \cdot dt &= \int f(v) dv \\ f(v) &= f(t) \cdot \frac{dt}{dv} = f(t) \cdot \frac{t^2}{l} \end{aligned} \quad (2.13)$$

Energy:

$$E = \frac{1}{2}mv^2 \quad (2.14)$$

Signal as a function of energy:

$$\begin{aligned} \int f(v) dv &= \int f(E) dE \\ f(E) &= f(v) \frac{dv}{dE} = f(v) \frac{t}{l} \end{aligned} \quad (2.15)$$

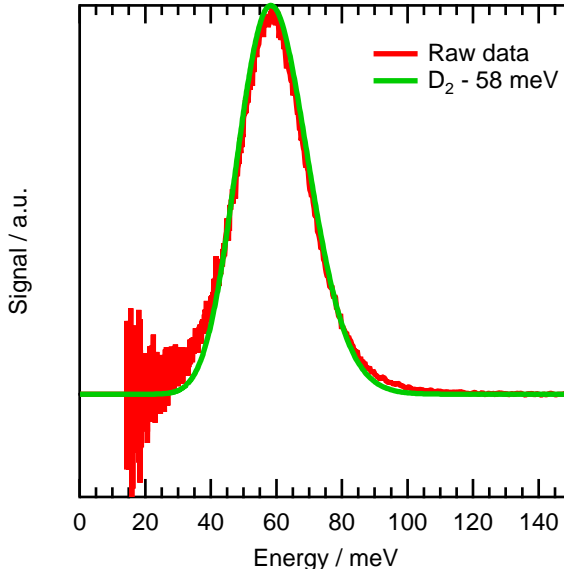


**Figure 2.12:** Example flux-weighted  $D_2$  kinetic energy distribution of the transformed raw data and the resulting fit for a pure  $D_2$  supersonic molecular beam. The most probable  $E_{kin}$  (FWHM) is 58.3 (25.2) meV .

Using this procedure, we extract kinetic energy distributions, exemplified by those shown in figure 2.12. Kinetic energy distributions of the beams used in chapters 3, 4, and 5 are included in their respective appendices.

### King and Wells

Initial sticking probabilities in chapters 3, 4, and 5 are measured using the standard King and Wells (KW) method.[11] Figure 2.13 shows two exemplary KW traces for  $D_2$  from chapter 3, as measured with the QMS. In the KW method, two beam flags are used to modulate the molecular beam. Figure 2.1 shows where the two inert flags are both located. The first flag either blocks the beam in SSB2, or lets the beam pass into the main chamber. As the molecular beam enters the main chamber, the molecular beam scatters off the second inert beam flag and increases the  $D_2$  partial pressure. ( $t = -5 - 0$  s) The measured stable (partial) pressure is proportional to the total flux incident entering the main chamber. After a few seconds,

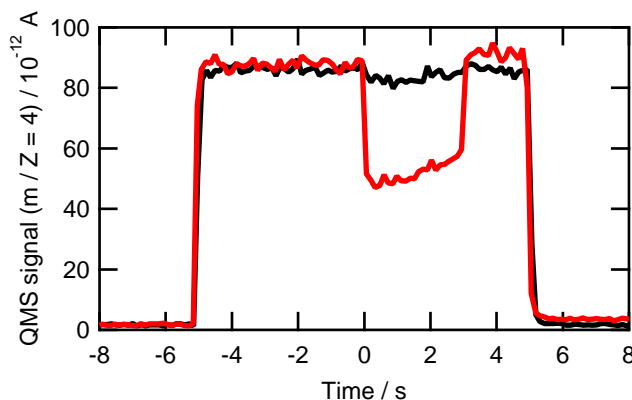


**Figure 2.13:** Two exemplary  $D_2$  King and Wells experiments for high (red) and low (black) step density surfaces.

the second flag is retracted at  $t = 0$  s so that the  $D_2$  beam impinges onto the sample. Molecules that either remain behind at the surface due to (dissociative) adsorption or react to form a different product lower the partial pressure of  $D_2$ , and hence the  $D_2$  flux, by a fraction. The King and Wells experiment is stopped by closing the second flag at  $t = 3$  s and closing the first flag at  $t = 5$  s

For chapters 3 and 4, the two beam flags are computer controlled with Labview to ensure that the time delay between opening and closing is well-defined. The resulting measured sticking curves are much more reproducible than manual controlled beam flags (chapter 5). Therefore, we can use signal averaging of multiple measurements to increase signal-to-noise levels.[46] With a curved single crystal surface, we can then measure sticking curves at up to 8 different crystal positions (surface structures) consecutively in one experiment. After each experiment with 7 or 8 surface structures probed, we flash the crystal to desorb all adsorbed molecules. For chapters 3 and 4, we perform a sputter and anneal cycle after 8 experiments.

Sticking on surfaces with low step density show the strongest time (coverage) dependence in chapter 3. Consequently, we start every sticking experiment at or nearest to the (1 1 1) apex and expose the crystal to the molecular beam for only 3 s at each position. We probe different surface structures on the crystal by moving the crystal with respect to the beam, starting from the apex, in one direction in 1 mm increments. In this way, we measure sticking probabilities for a number of relative crystal positions (and different surface structures) in one experiment, e.g. 0 mm (1 1 1), +1 mm, +2 mm, +3 mm, -3 mm, -2 mm, -1 mm. Consecutive experiments are performed in reverse order, but still start at or close to the (1 1 1) surface. We observe no difference in  $S_0$  between experiments performed in normal or reverse order.

Results from the King and Wells experiments are normalized to the total flux and inverted, yielding time (coverage) dependent sticking traces. Two typical sticking traces for surfaces containing A- or B-type step edges are shown in figure 2.14 along with the fits used to extrapolate to  $S_0(\text{D}_2)$  in chapter 3.  $S_0$  is extracted from these time (coverage) dependent data by extrapolating a linear least squares fit to  $t = 0$  s:

$$S(t) = S_0 + \frac{dS}{dt} \cdot t \quad (2.16)$$

There is an error in  $S_0$  due to an uncertainty in the slope and the intercept. An additional error is introduced in  $t = 0$ , because the mass spectrometer measures  $\sim 7$  data per second. We assume that the flag, and hence  $S_0$ , occurs at  $t = 0$  s. We calculate the error propagation in the usual way for multiplication and summation.

We determine reaction probabilities in a similar fashion for reactions at surfaces in chapters 4 and 5. The reactant partial pressure ( $\text{D}_2$  for chapter 4 and  $\text{O}_2$  and  $\text{HD}$  for chapter 5) decrease as they are consumed in surface reactions. For chapter 4, we again measure the average partial pressure fraction consumed when opening the second beam flag to determine the consumption probability. The same applies for chapter 5, but two



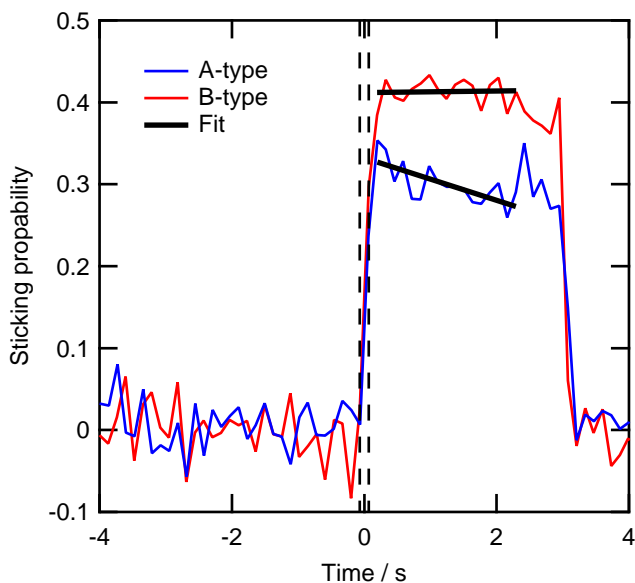


**Figure 2.14:** Typical signal averaged sticking traces are shown in blue and red for A- and B-type step edges. The black linear fit is extrapolated to  $t = 0$ . The dashed lines indicate the error in determining  $t = 0$ .

molecular beams are used in conjunction. There, the KW method requires normalization under identical experimental conditions, i.e. identical incident flux from both molecular beams with the second flag open and closed. Appendices C and D elaborate on the methods used to extract reaction probabilities for these experiments.



---

**Site-specific reactivity of molecules with surface defects – the case of  
H<sub>2</sub> dissociation on Pt**

---

The classic system that describes weakly activated dissociation in heterogeneous catalysis has been explained by two dynamical models that are fundamentally at odds. Whereas one model for hydrogen dissociation on Pt(1 1 1) invokes a pre-equilibrium and diffusion toward defects, the other is based on direct and localized dissociation. We resolve this dispute by quantifying site-specific reactivity using a curved Pt single crystal surface. Reactivity is step type dependent and varies linearly with step density. Only the model that relies on localized dissociation is consistent with our results. Our approach provides absolute, site-specific reaction cross sections.

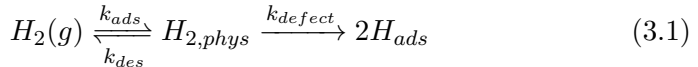
## Introduction

At the heart of any chemical transformation lie the dynamical events associated with elementary reactions. In gas phase reactions, reactant energy is redistributed over the limited degrees of freedom available in the products. For gas-surface collisions, the bulk provides a massive sink for energy dissipation. This makes mechanistic problems for gas-surface reactions quite challenging, as exemplified by ongoing discussion regarding the role of phonons and electron-hole pairs in surface reactions.[57, 58] In addition, surface heterogeneity may cause site-specific reactions to dominate overall kinetics in catalysis. For example, CO oxidation was recently shown to be site-specific on both Pt[47] and Pd[45].

The prototypical system in heterogeneous catalysis is  $\text{H}_2$  dissociation on Pt. It is essential to the development of chemically accurate theoretical modeling of gas-surface interactions.[59] It is clear that  $\text{H}_2$  dissociation occurs through dynamical processes.[59, 60] However, after four decades of research, two opposing dynamical models describing  $\text{H}_2$  dissociation prevail in the literature. The fundamental discrepancy between the models lies in the assumed fate of kinetic energy of incident molecules. In the first model, it is conserved in the collision and incident molecules elastically scatter into a precursor state. In the second model, incident kinetic energy is not conserved. Depending on the exact point of impact, it couples directly to the dissociation coordinate or is dissipated, for example, by excitation of a frustrated rotation.

The two models for  $\text{H}_2$  dissociation on Pt surfaces are illustrated in figure 3.1. Model 1, schematically shown in figure 3.1a, was proposed by Poelsema, Lenz, and Comsa.[61, 62] Scattering experiments have previously shown that atoms and molecules may diffract into a physisorbed state.[63, 64] In their model, the elastic collision only leads to dissociation when a  $\text{H}_2$  molecule also encounters a defect during friction-free diffusion across the

surface. The model is summarized by:



The rate constant for adsorption ( $k_{ads}$ ) depends on the probability to resonantly scatter into the physisorbed state ( $S_{0,nL}$ ). The rates at which physisorbed molecules desorb ( $k_{des}$ ) or encounter defects ( $k_{defect}$ ) depend on their velocity ( $\nu$ ), residence time ( $\tau$ ), and the average distance between defects ( $L_d$ ). The model predicts a dissociation probability on the clean surface,  $S_0$ :

$$S_0 \propto S_{0,nL} \left(1 - e^{-\frac{L_d}{\nu\tau}}\right) \quad (3.2)$$

For large distances between defects, reactivity is rather sensitive to  $L_d$ . For short distances, i.e. higher defect densities, this sensitivity is lost. The transition occurs when the physisorbed molecule has a mean free path, i.e.  $\nu \cdot \tau$ , comparable to the distance between defects.

In model 2, Baerends and coworkers,[65] Hayden and coworkers,[66] and Somorjai and coworkers[67] propose parallel dynamical mechanisms for different surface sites, e.g. terraces and steps. None of these mechanisms contains a long-lived, diffusing precursor state. Dissociation is adequately represented as elementary:



The observed reactivity represents an average ( $k_{ave}$ ) from site-specific contributions. Terraces contribute by direct dissociation, as illustrated in figure 3.1b. Incident kinetic energy is used to surmount activation barriers that vary with exact location and molecular orientation. Steps contribute by the two mechanisms illustrated in figures 3.1c and 3.1d. The first occurs at the cusp and is responsible for the initial negative correlation of reactivity with incident kinetic energy ( $E_{kin}$ ). [66, 68] Dynamical calculations suggest that kinetic energy is converted to molecular rotation. Dissociation occurs when the dynamically trapped molecule senses the upper edge of the step.[65] The second contribution by steps is barrier-free dissociation at the upper edge.[65, 66, 68–70] Kinetic energy flows into the reaction coordinate

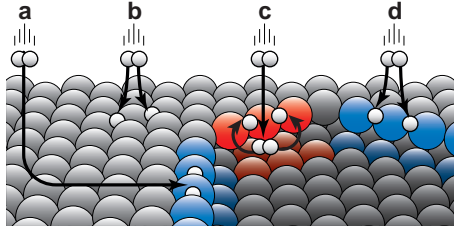


**Figure 3.1:** a) Model 1: mobile precursor mechanism. b) Model 2: direct activated dissociation at (1 1 1) terraces. c) Model 2: trapping mediated dissociation at step edges. d) Model 2: direct dissociation at step edges. A- and B-type steps are shown in blue and red respectively. c) and d) can take place at either step type but relative contributions may vary.

and is quickly lost to the substrate. The reactivity constant in this model can be represented as the weighted average of site-specific reactivities,  $S_0^{site}$ ,

$$S_0 \propto \sum_{site} f^{site} \cdot S_0^{site} \quad (3.4)$$

In contrast to the previous one, this second model thus predicts a strictly linear relation between reactivity and the fractional occurrence of each type of reactive site,  $f^{site}$ . Whereas the first model also did not discriminate between defects, this model does allow for varying contributions by, e.g., the A- and B-type step edges depicted in figure 3.1.

A new approach allows us to test both models on a single sample. The step density along a curved Pt surface has been shown to vary smoothly from 'defect free' (1 1 1) to highly stepped surfaces.[36] By combining a curved surface approach and supersonic molecular beam methods [30] with highly improved spatial resolution, we resolve that  $H_2$  dissociation does not require physisorption and diffusion to defect sites. In addition, we quantify site-specific reactivities for both  $\{0\ 0\ 1\}$  (A-type) and  $\{1\ 1\ 0\}$  (B-type) step types.

## Method

A schematic illustration of the experiment is shown in figure 3.2a-e. Our Pt single crystal is cut as a  $31^\circ$  section of a cylinder along the  $[1\ \bar{1}\ 0]$

rotational axis. The (1 1 1) surface appears at the apex.[71] The macroscopic curvature of the crystal is a direct result of monatomic steps.[36] Consequently, the local surface structure on our crystal varies smoothly from Pt(3 3 5) via Pt(1 1 1) to Pt(5 5 3).[71] As both A- and B-type steps are spatially separated by the (1 1 1) surface, their influence on reactivity can be probed independently. We measure initial sticking probabilities ( $S_0$ ) using the King and Wells approach (see chapter 2).[11] The molecular beam is incident on the surface along the [1 1 1] vector. We measure  $S_0$  as a function of step density by translating the single crystal surface with respect to our rectangular-shaped supersonic molecular beam (0.126 x 6.0 mm<sup>2</sup>). Figure 3.2d illustrates the relative sizes of the crystal and the beam. Figure 3.2e quantifies the convolution of the narrow molecular beam with step density. Near (1 1 1) it is limited to 0.01 nm<sup>-1</sup>. Our measurements are limited to step densities of 0.8 nm<sup>-1</sup> due to narrowing of the crystal at high step densities in combination with the 6 mm width of our beam.

## Results and Discussion

Figure 3.2f shows  $S_0$  at a surface temperature ( $T_s$ ) of 155 K as a function of step density and step type for  $E_{kin} = 9.3$  meV and 100 meV. These energies are produced by (anti)seeding D<sub>2</sub> beams and estimated from time of flight measurements. At the lower  $E_{kin}$ ,  $S_0$  starts at  $0.01 \pm 0.05$  for the (1 1 1) surface and increases linearly with step density.  $S_0$  for B-type step edges are consistently higher than A-type step edges at similar step density. At the higher  $E_{kin}$ , the influence of steps has disappeared and  $S_0$  is approximately constant over the entire step density range. This energy dependence is consistent with all previous King and Wells studies of H<sub>2</sub> dissociation on flat and stepped single crystal surfaces. [18, 66, 68–70, 72]

For the lower  $E_{kin}$ , where steps are the dominant source of dissociation, figure 3.3 compares  $S_0$  as a function of step density for  $T_s = 155$  K and 300 K. Results are only shown for B-type steps, but the trend is identical for A-type steps. Also shown as dashed lines are predictions for  $S_0$  by model 1,[62] as described in appendix B. The curvature in the predicted step density

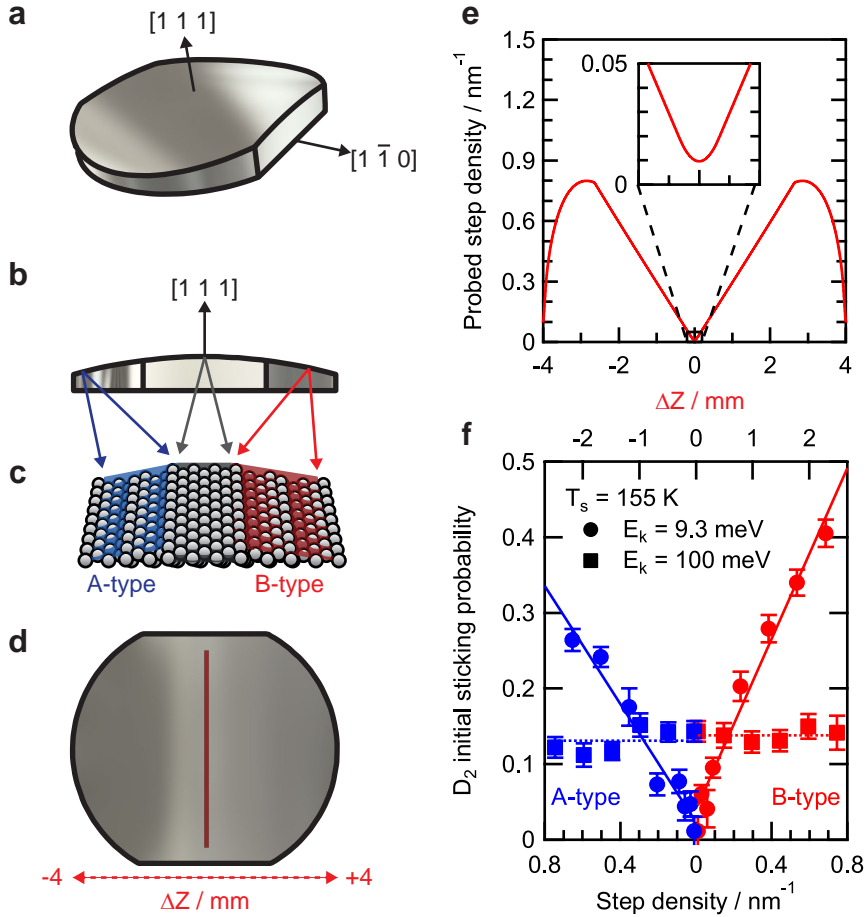


**Figure 3.2:** a) Birdseye view of the curved Pt single crystal. b) Side view along the  $[1\ \bar{1}\ 0]$  vector. c) Side view showing the surface structure and surface planes of Pt(3 3 5) (A-type steps), Pt(1 1 1), and Pt(5 5 3) (B-type steps) in blue, gray, and red, respectively. d) Top view with the molecular beam size in red. e) Step density probed by the molecular beam at the position relative to the (1 1 1) surface. f)  $S_0$  ( $D_2$ ) at  $T_s = 155\text{ K}$  as a function of step density. Results from A- and B-type step edges are depicted in blue and red. Circles and squares represent  $E_{kin} = 9.3\text{ meV}$  and  $E_{kin} = 100\text{ meV}$ . Lines are least square fits to the data. Error bars represent the standard deviation in  $S_0$ .



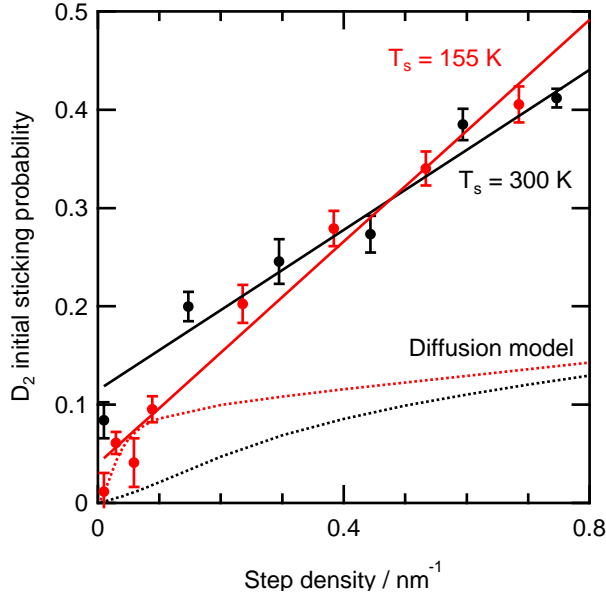


**Figure 3.3:**  $S_0$  (D<sub>2</sub>) for  $E_{kin} = 9.3$  meV as a function of **B-type** step density. Circles are measured data. Solid lines are fits to the data. Dashed lines are predicted results from model 1. Red and black represent  $T_s = 155$  K and 300 K respectively. Error bars represent the standard deviation in  $S_0$ .

dependence is a logical consequence of model 1. When the 'mean free path' of the physisorbed state approaches or exceeds the distance between defects, increasing defect density becomes less effective in increasing  $S_0$ . Only at high defect density, does  $S_0$  become proportional to step density.

Our results are clearly at odds with the predictions by this model. Not only is  $S_0$  underestimated over the entire defect density range, two crucial dependencies are not reproduced in the experiment. First, predicted curvature in the  $S_0$  dependence on step density near the (1 1 1) surface is absent. Second, the  $T_s$  dependence opposes the predicted trend. Whereas model 1 clearly reduces  $S_0$  with increasing  $T_s$  due to the diminishing residence time in a physisorbed state, we find that  $S_0$  generally increases or is hardly affected. An attempt to improve the model by incorporating Debye-Waller

attenuation, reducing the probability of scattering into the resonant state, would increase this discrepancy. In addition to these erroneous dependencies, the site-specific reactivity of  $S_0$  seen in figure 3.2f is not captured in model 1. Finally, it also does not capture the observed step density independence at the higher  $E_{kin}$ .

In contrast, our results are in agreement with the two underlying assumptions of model 2. Terrace and step sites contributing proportionally to their abundance and the absence of a freely diffusing precursor require a strictly linear dependence of  $S_0$  on step density. Least squares fitting yields a residual reactivity due to dissociation on the Pt(1 1 1) surface. Individual fits to **A-** and **B-type** steps for lower incident energy yields  $0.023 \pm 0.009$  and  $0.040 \pm 0.008$ . This is in good agreement with previous results[18, 72] for Pt(1 1 1), even with experimental results for the clean 'defect free' surface [61] on which model 1 is based. This residual reactivity of the 'defect free' Pt(1 1 1) surface is explained by recent dynamical calculations for  $D_2$  dissociation.[73] Select impact geometries show barrier-free dissociation on the Pt(1 1 1) surface.

The slope of the linear fits in figure 3.2f reflect the summed contributions of direct barrier-free and trapping-mediated dissociation at step edges, shown in figures 3.1c-d. Multiplying the slope of each linear fit with the width of the unit cell yields the reaction cross section for  $H_2$  dissociation at the step edge.[70] For our low  $E_{kin}$  data at  $T_s = 155$  K, these are  $0.108 \pm 0.007$  and  $0.157 \pm 0.007$  nm<sup>2</sup> for **A-** and **B-type** steps. The reaction cross section for **A-type** steps agrees quantitatively with theoretical results that show the surface area of the Pt(1 1 2) unit cell where impact at the step results in dissociation.[65] We previously showed that the direct contribution at the upper edge, shown in figure 3.1d, amounts to 0.043 nm<sup>2</sup>. [70] The trapping-mediated mechanism in figure 3.1c is then responsible for the 0.065 nm<sup>2</sup> difference at **A-type** steps. As the local structure at the upper edge is identical, the significantly larger cross section for **B-type steps** compared to **A-type** steps suggests larger and/or deeper molecular chemisorption wells at its cusp.

## Conclusion

In summary, the model ascribing H<sub>2</sub> dissociation on Pt mostly to a highly mobile precursor fails to predict the reactivity dependence on step density and surface temperature. In addition to a lack of site specificity, the model erroneously assumes that the perfect Pt(1 1 1) surface only exhibits activated adsorption.[73] As reactivity in this model is fully ascribed to defects, the model’s parameters and other conjectures must reflect this overestimate. We believe this to be represented by the unphysical assumption that all scattering occurs into the ground vibrational level of the physisorbed state. Furthermore, while the model’s parameters are based on a fit to experimental data using dissociation from a bulb gas at room temperature, the known complex angular dependence to dissociation [18, 74] is not taken into account. More assumptions may contribute to its failure, e.g. that no other possible outcome than dissociation exists when physisorbed molecules encounter a defect.

Simultaneously, our data support that dissociation is dominated by impulsive interactions at the impact site. In the relevant regime, there is no significant surface temperature dependence and, at low kinetic energy, dissociation is strictly linear with step density. At incident energies exceeding most barriers to dissociation on the terrace, the contribution of steps becomes indiscernible; reactivity becomes independent of step density. From our low kinetic energy data, we extract site-specific reaction cross sections for **A-** and **B-type** step edges in a chemical reaction. The reaction cross section of **B-type** steps is significantly larger than that of **A-type** steps, suggesting a larger molecular chemisorption well with more efficient kinetic energy dissipation. These results present benchmarks for future construction of high dimensional potential energy surfaces and guide dynamical studies aiming to understand the kinetics of this prototypical system. In particular, the origin of the significantly larger cross section for dissociation at **B-type** step edges may be extracted from calculation of the potential energy surface of H<sub>2</sub>/Pt(2 2 1). Additional (quantum) dynamical calculations, similar to those performed by Baerends and coworkers[65, 75]

could confirm the dominant contributions of the three parallel dynamical mechanisms captured by model 2.

---

**Two-faced step edges in HD exchange on Pt**

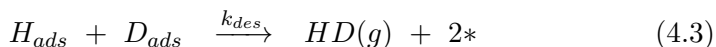
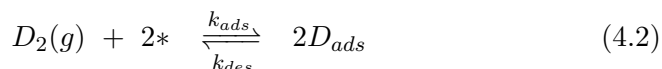
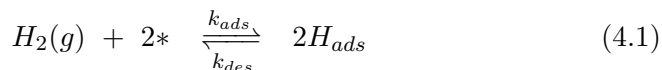
---

Particle size effects in catalysis are commonly attributed to the number of defect sites present and their electronic properties. Dissociation increases with the number of defects, but how subsequent atomic diffusion at defects influences overall reactivity is generally disregarded. Measuring structure sensitive surface diffusion directly is challenging, especially under reaction conditions, where the kinetics are too fast for most experimental techniques. By using the varying step density of a curved single crystal surface, we instead study how isotopic scrambling of dihydrogen is influenced by step edges. Our results show that step edges lower selectivity towards the HD product compared to terrace sites. We introduce a model that assumes fast isotropic mixing at terraces and no diffusive mixing at steps. The model agrees qualitatively with our data and may provide an additional explanation for lower catalytic activity of very small nanoparticles.

## Introduction

Catalysts increase reaction rates of chemical reactions and enable many industrial applications in use today. While heterogeneous catalysts speed up chemical reactions, the reaction mechanisms at play are still not fully understood. Unraveling reaction mechanisms requires systematic study of all elementary steps involved and identifying reaction intermediates. For heterogeneous catalysts, this is exacerbated by the heterogeneous nature of surfaces; elementary reaction steps may be surface-structure dependent.

The simplest heterogeneously catalyzed reaction is isotopic scrambling of dihydrogen. A good catalyst is Pt. The reaction mechanism requires at least three elementary reaction steps:  $H_2$  dissociation,  $D_2$  dissociation, and subsequent recombination to form HD:



The heterogeneous nature of the catalyst surface is not captured in these commonly used reaction equations. The stars in the equations indicate surface sites, but do not distinguish between different types. Indeed, previous studies showed that HD formation on Pt surfaces [76–78] is strongly influenced by surface structure. This was explained by increased dissociative sticking of reactants at step edges.

Following several studies [65, 66, 68–70, 75] on the influence of steps, we recently showed that hydrogen dissociation is direct, local, and step type dependent.[79] Reactions 4.1 and 4.2, as the simplest dissociative gas-surface reactions, are thus rather well-understood. However, reaction 4.3 requires that hydrogen ( $H_{ads}$ ) and deuterium ( $D_{ads}$ ) atoms be adjacent. Therefore, HD formation is expected to depend on the surface mobility of  $H_{ads}$  and  $D_{ads}$  and their degree of mixing.

Diffusion on Pt(1 1 1)[80] is fast, as barriers for  $H_{ads}$  and  $D_{ads}$  diffusion are low: 68 meV and 76 meV respectively[81]. These barriers have been corroborated by theory.[82, 83] Diffusion on Pt(1 1 1) proceeds via two parallel mechanisms: quantum tunneling at low temperature and classical hopping at high temperature.[84, 85] Studies on the influence of surface defects on hydrogen diffusion have been limited[86, 87] due to additional challenges involved.[81, 82] However, theory has predicted that diffusion at steps is anisotropic.[88] Barriers for diffusion parallel and orthogonal to the  $\{0\ 0\ 1\}$  step edge are 0.15-0.2 and 0.35 eV respectively, significantly exceeding barriers on the (1 1 1) terraces.[88]

In this study, we resolve whether these larger diffusion barriers influence HD formation on Pt surfaces. Combining molecular beam techniques and a curved single crystal surface approach, we compare locally averaged-step density dependent HD formation and  $D_2$  consumption in a zero (low) coverage limit with initial sticking probabilities. Although both the  $\{0\ 0\ 1\}$  (A-type) and  $\{1\ 1\ 0\}$  (B-type) steps enhance dissociative adsorption, they are less selective toward enhancing HD formation. Anisotropic diffusion at steps limits diffusive mixing compared to extended (1 1 1) terraces. This is corroborated by increased HD selectivity upon faceting a section of the curved crystal surface. A simple model qualitatively agrees with our results and shows that diffusion of intermediates is integral to the overall reaction mechanism and selectivity toward the HD product.

## Method

Experiments are performed in an ultra-high vacuum setup with a base pressure lower than  $1 \cdot 10^{-10}$  mbar. The apparatus contains, among others, a quadrupole mass spectrometer (QMS), a supersonic molecular beam with an on-axis quadrupole mass spectrometer for time of flight measurements, and low energy electron diffraction and Auger electron spectroscopy optics. The Pt single crystal surface and the crystal holder are schematically shown in figure 4.1a. The curved surface protrudes from a square holder with two legs attaching it to a liquid nitrogen cryostat. The crystal is cut

as a  $31^\circ$  section of a cylinder with a 15 mm radius,  $[1 \bar{1} 0]$  as principal axis, and the  $(1 \ 1 \ 1)$  surface at the apex ( $Z = 0$  mm). With the proper cleaning procedure[89], the macroscopic curvature of the surface is a direct consequence of monatomic steps. Consequently, the local surface structure on our crystal varies smoothly from  $\text{Pt}(3 \ 3 \ 5)$  via  $\text{Pt}(1 \ 1 \ 1)$  to  $\text{Pt}(5 \ 5 \ 3)$ . [71] As both **A**- and **B-type** steps are spatially separated by the  $(1 \ 1 \ 1)$  surface, their influence on reactivity can be probed independently.

Reactivity experiments are performed using supersonic molecular beam techniques.  $\text{H}_2$  and  $\text{D}_2$  are antiseeded in Ar and supersonically expanded from a tungsten nozzle with a 28  $\mu\text{m}$  orifice. The expansion is skimmed. Two additional pumping stages and skimmers produce a rectangular-shaped molecular beam at the sample ( $6.0 \times 0.126 \text{ mm}^2$  or  $6.0 \times 0.5 \text{ mm}^2$ ). The  $\text{H}_2$  and  $\text{D}_2$  mixture is made such that the surface concentrations are equal in the following way. The reaction rate for forming HD,  $R_{\text{HD}}$ , can be written as:

$$R_{\text{HD}} = k \cdot [\text{H}_{\text{ads}}] [\text{D}_{\text{ads}}] \quad (4.4)$$

where  $k$  is the reaction rate constant, and  $[\text{H}_{\text{ads}}]$  and  $[\text{D}_{\text{ads}}]$  are the surface concentrations of hydrogen and deuterium. If we assume low surface coverage, resulting from fast recombinative desorption, and no isotope dependence for adsorption and desorption[18, 66], then the relative surface concentrations are:

$$[\text{H}_{\text{ads}}] \propto 2 \cdot \bar{S}_0 \Phi_{\text{H}_2} \quad (4.5)$$

$$[\text{D}_{\text{ads}}] \propto 2 \cdot \bar{S}_0 \Phi_{\text{D}_2} \quad (4.6)$$

$\bar{S}_0$  is the local average sticking probability, which depends on step density and by extension on position on the curved surface. It also depends on kinetic energy ( $E_{\text{kin}}$ ).  $E_{\text{kin}}$  for  $\text{H}_2$  and  $\text{D}_2$  are approximately 11 and 23 meV respectively, as determined using time of flight measurements. The higher  $E_{\text{kin}}$  for  $\text{D}_2$ , decreases its  $\bar{S}_0$  by a factor of 1.4.[70] We compensate this by mixing 1.4 times more  $\text{D}_2$  into the beam than  $\text{H}_2$ . Consequently,  $[\text{H}_{\text{ads}}]$  and  $[\text{D}_{\text{ads}}]$  are approximately equal under reaction conditions.



Reactivity measurements are performed with the standard King and Wells approach.[11] The molecular beam forms a  $6.0 \times 0.126 \text{ mm}^2$  (or  $6.0 \times 0.50 \text{ mm}^2$ ) stripe on the single crystal surface. The narrow size of the beam limits the step density convolution along the curved surface. The relative size of the narrow molecular beam and the sample are shown in figure 4.1. Upon being admitted into the main chamber, the beam is blocked by an inert flag. The partial pressures of  $\text{H}_2$ ,  $\text{D}_2$ , HD, and Ar increase, thereby providing a measure of the background reactivity of the UHV system, e.g. due to hot filaments. After 30 seconds, the inert flag is retracted and the beam directly impinges onto the sample. An increase and decrease in the HD and  $\text{D}_2$  partial pressures respectively indicates reactivity toward HD formation by the sample. After measuring HD formation for 30 s, both flags are closed. The sample is subsequently moved 0.5 mm to expose a different section of the curved surface to the molecular beam.

The King and Wells[11] approach works if molecules that scatter off the inert flag and the sample increase the background pressure isotropically. The validity of this assumption requires that the QMS has no line of sight of the beam scattering off either the sample or the inert flag. The curved nature of the surface increases the risk of measuring higher partial pressures due to directional scattering of molecules from the sample into the ionization region of the QMS. The top panel of figure 4.1b shows the evolution of Ar carrier gas throughout the isotopic scrambling experiment. The shaded and hatched sections indicate Ar scattering off the inert flag and the curved crystal respectively. Regardless of whether the beam scatters off the inert flag or the sample, the Ar signal remains constant for each position.

The absolute Ar signal clearly increases over the course of the experiment. The nozzle and expansion pressures are constant throughout the day, ruling out a change in beam conditions. We have previously observed that the absolute QMS signal increases[53] or decreases[90] in a reducing or oxidizing gas for our type of QMS (Baltzers Prisma QMS 200). Comparison of the Ar signal with the HD and  $\text{D}_2$  signals in the other panels of figure 4.1

reveal that the relative sensitivity change varies for the different gases. It seems that the change in signal is due to a change in oxidation state of either the QMS filament or the channeltron. The emission current of the QMS filament is regulated, leaving the channeltron as the likely culprit. We suggest that oxidation or reduction of the channeltron material reduces or increases the number of electrons released upon impact. This also explains why the sensitivity change varies seems to be gas-specific, as evidenced by the different relative increases for Ar and D<sub>2</sub> shown in figure 4.1b. During data analysis, we correct for changes in signal by scaling measured data with their background (shaded area) partial pressure.

In addition to Ar, the D<sub>2</sub>, H<sub>2</sub>, and HD QMS currents are measured for various surface structures by impinging the molecular beam onto different sections along the curved surface. H<sub>2</sub> results are omitted from further discussions as the H<sub>2</sub> background pressures are higher and QMS signals for mass-to-charge ratio of 2 are convolved by D<sub>2</sub>. Figure 4.1b compares the raw data of the HD formation experiment for five positions. At every position, we first obtain the background HD partial pressure resulting from all catalytic surfaces, e.g. the nozzle or hot filaments from the sample heating or QMS. Upon impinging the beam onto the surface, H<sub>2</sub> (not shown) and D<sub>2</sub> are consumed to form HD (hatched area).

## Results and Discussion

From the raw data in figure 4.1, we extract the relative step density dependent HD formation rate,  $R_{HD}$ . We subtract the background production from the total amount and include previously mentioned corrections for the channeltron efficiency. Figure 4.2 shows these HD formation rates at  $T_s = 500$  K and 800 K with our previous  $\bar{S}_0$  results (chapter 3) at  $T_s$  155 K and 300 K. HD formation shows the same three characteristics as  $\bar{S}_0$ : HD rates are lowest for the (1 1 1) surface, increase linearly with step density, and are higher at **B-type** than **A-type** step edges. In contrast to  $\bar{S}_0$ , increasing  $T_s$  lowers HD formation slightly. Most striking though, step edges yield an approximate tenfold increase in  $\bar{S}_0$  from the apex to the crystal edge, while

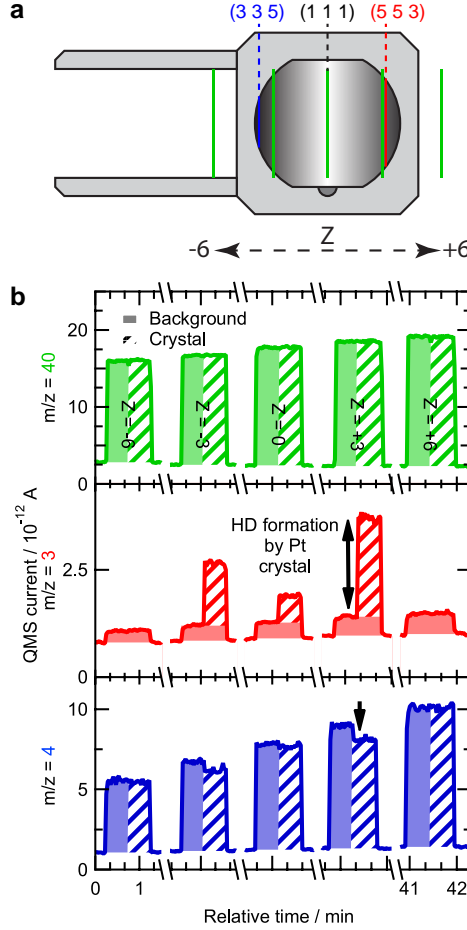


**Figure 4.1:** King and Wells type HD formation experiments at 800 K. a) The molecular beam (green) impinges onto different parts of the curved surface. The relative sizes of the molecular beam and the sample are to scale. Also indicated are the  $(3\ 3\ 5)$  (blue) and  $(5\ 5\ 3)$  (red) surfaces. b) The top, middle, and bottom panels show the raw Ar, HD, and  $D_2$  data respectively for the five different positions indicated in figure 4.1a. The shaded areas show the background signal of HD, Ar, and  $D_2$  after scattering off the inert flag. The hatched areas indicate the beam directly impinging onto the curved sample. The hatched area in the HD signal indicates the HD rate (QMS current) produced by the sample. The fractional drop of the hatched  $D_2$  signal is used to determine  $\bar{C}_0$ .

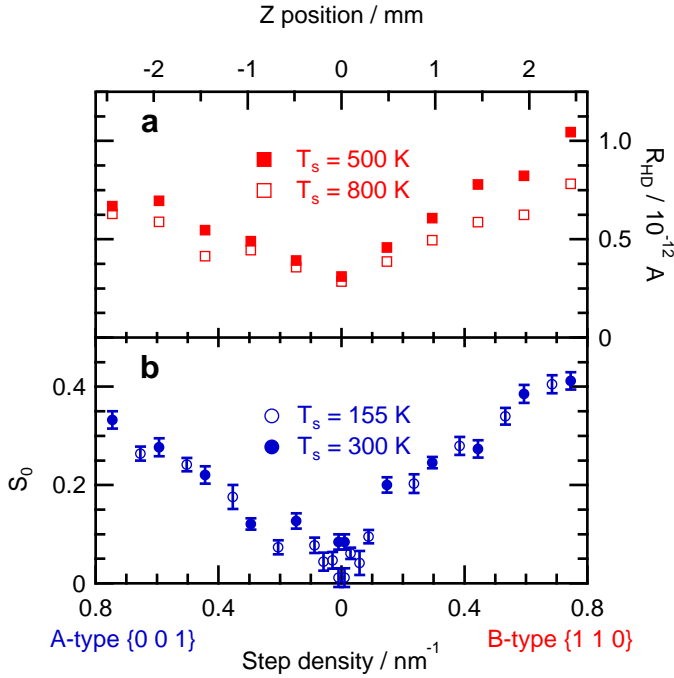


**Figure 4.2:** a) D<sub>2</sub> initial sticking probability ( $\bar{S}_0$ ) and b) HD rate (QMS current) measured as a function of **A-** (left) and **B-type** (right) step density with a 126  $\mu\text{m}$  sized molecular beam.

HD formation only increases roughly threefold over the same step density range for the more reactive step type. Surprisingly, H-D exchange is thus relatively high for the (1 1 1) surface compared to highly stepped surfaces.

A more insightful comparison can be deduced from the drop in D<sub>2</sub> partial pressure in figure 4.1 when HD is being formed (marked by the arrow in the bottom panel). We define  $\bar{C}_0$  as the locally-averaged initial consumed D<sub>2</sub> fraction when performing the H-D exchange reaction on the clean surface, akin to initial sticking probabilities ( $\bar{S}_0$ ) as determined by the King and Wells method[11]. Figure 4.3 shows  $\bar{C}_0(\text{D}_2)$  during HD production as a function of step density for  $T_s = 500$  K and 800 K. Again,  $\bar{C}_0(\text{D}_2)$  is linear with step density, but increases only a factor of 2-3 over the entire step density range. It varies from 0.04 at the (1 1 1) surface to 0.07 and 0.11 at high **A-type** and **B-type** step densities, respectively. Hence, the same

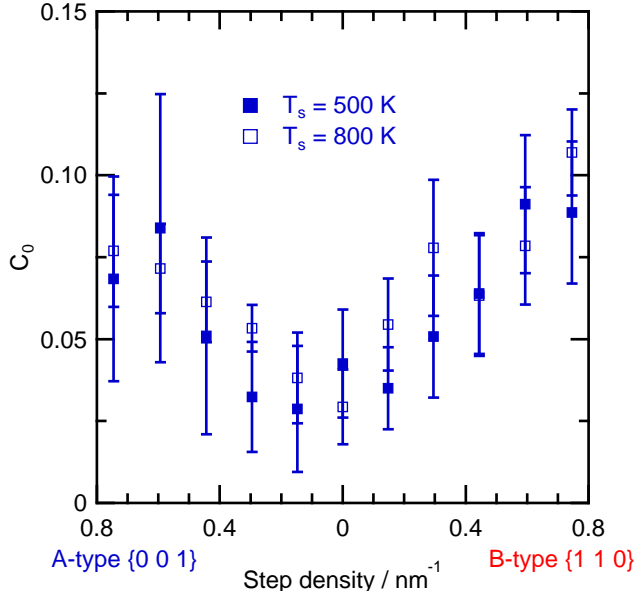
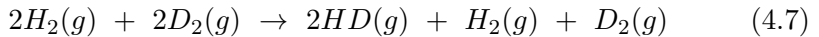


**Figure 4.3:** D<sub>2</sub> consumption probability ( $\bar{C}_0$ ) during HD production shown in figure 4.2 as a function of step density measured with a 126  $\mu\text{m}$  sized molecular beam.

characteristics observed in HD product formation reappear when analyzing loss of one the two reactants (here D<sub>2</sub>). Only the T<sub>s</sub> dependence seems lost in the noise.

Variations in how dissociated reactants diffuse may impact the HD rate and  $\bar{C}_0$  compared to  $\bar{S}_0$  for different reaction sites. We take two extreme cases. For (1 1 1) surfaces we assume fast diffusion leading to isotropic mixing. For steps, we assume no diffusion.

If fast diffusion of equal H<sub>ads</sub> and D<sub>ads</sub> surface concentrations leads to an isotropic mixture, the overall surface reaction becomes:



which expresses the statistically expected ratio through the stoichiometric coefficients. From this, it follows that half of the impinging D<sub>2</sub> (H<sub>2</sub>) is

consumed to form HD. Hence, the  $\bar{C}_0$  ( $D_2$ ) is:

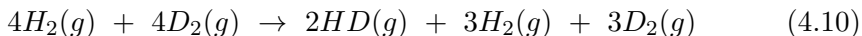
$$\bar{C}_0 = \frac{1}{2} \cdot \bar{S}_0 \quad (4.8)$$

Here, we neglect isotope effects. Different zero point energies for  $H_2$ ,  $D_2$ , and HD only slightly alter the  $H_2$ ,  $D_2$ , and HD equilibrium pressures. We justify this choice by realizing that our beam experiments occur on a single collision basis and start with only  $H_2$  and  $D_2$ . Since the sticking probabilities are lower than unity (only 0.08 at (1 1 1)), our experiments cannot reach equilibrium.

The situation changes for assumed absence of diffusion at steps. In the limit of no diffusion parallel or orthogonal to the step edge, atoms that originate from the same molecule remain adjacent to one another. Figure 4.4 illustrates how the statistics change. Consider the red step bound atoms as  $D_{ads}$  from a dissociated  $D_2$  molecule, while green step bound atoms represent  $H_{ads}$  or  $D_{ads}$  (originating from either  $H_2$  or  $D_2$ ). Recombinative desorption of either red atom has a 50% probability to desorb with its original partner, forming  $D_2$ . Alternatively, there is a 50% chance that a red atom desorbs with its green neighbor, desorbing as HD or  $D_2$  depending on whether the green atoms were originally an  $H_2$  or  $D_2$  molecule. In the limit of low coverage and no diffusion, absence of green atoms increases the probability of forming back the original molecule. Consequently, 75% of available H and D atoms return as  $H_2$  and  $D_2$ . At most, 25% of available  $H_{ads}$  and  $D_{ads}$  atoms are consumed to form HD in this scenario:

$$C_{0,steps} = \frac{1}{4} \cdot S_0 \quad (4.9)$$

The overall surface reaction at steps becomes:



The difference between fast and no diffusion thus reveals itself in the fraction  $\eta$ :

$$\bar{C}_0 = \eta \cdot \bar{S}_0 \quad (4.11)$$

The best case scenarios we have presented here show that fast diffusion and an isotropic distribution of surface bound atoms is revealed by  $\eta = 0.5$ . Slow anisotropic diffusion at steps may exhibit  $\eta = 0.25$  at best. As the ability to mix decreases, so does  $\eta$ .

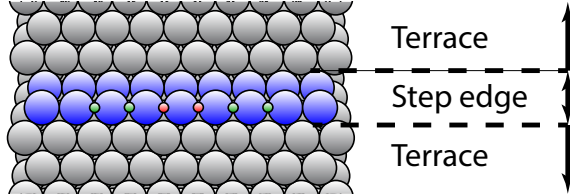


**Figure 4.4:** Illustration of hindered mixing at steps.

Reactivity measurements at the (1 1 1) surface show  $\bar{S}_0 = 0.08$  for  $T_s = 300$  K.  $\bar{C}_0$  ( $D_2$ ) = 0.04 indicates that mixing at the (1 1 1) surface is isotropic,  $\eta = 0.5$ . At high step densities,  $\bar{S}_0$  for **A-type** and **B-type** step edges shown in figure 4.2 are as high as 0.33 and 0.41. Fast diffusion at steps would result in  $\bar{C}_0$  ( $D_2$ ) equals 0.15 and 0.20. Instead, we find that  $\bar{C}_0$  ( $D_2$ ) equals 0.08 and 0.09, which agrees with limited diffusion at steps. However, large error bars of  $\bar{C}_0$  in figure 4.3 prevents reliable  $\eta$  determination. Therefore, we will now present  $\eta$  as a function of step density measured with a larger beam, thereby reducing spatial resolution but improving the signal-to-noise ratio.

To emphasize the influence of local surface structure, we use an extra characteristic of the curved Pt(1 1 1) crystal to our advantage. It contains **Pt(9 9 7)**, which is well-known to exhibit step-doubling and faceting.[89, 91] Both types of reconstructions lower step density and increase the fraction of (1 1 1) terraces. The sensitivity to reconstructions of **Pt(9 9 7)** requires a specific cleaning procedure for the curved Pt(1 1 1) sample.[53] The correct cleaning procedure yields the desired surface structure with monatomic steps and no faceting. However, reconstructions provide additional means to study the influence of surface structure, e.g. how double high step edges affect reactivity.[92] Here, we anneal the sample to  $T_s =$

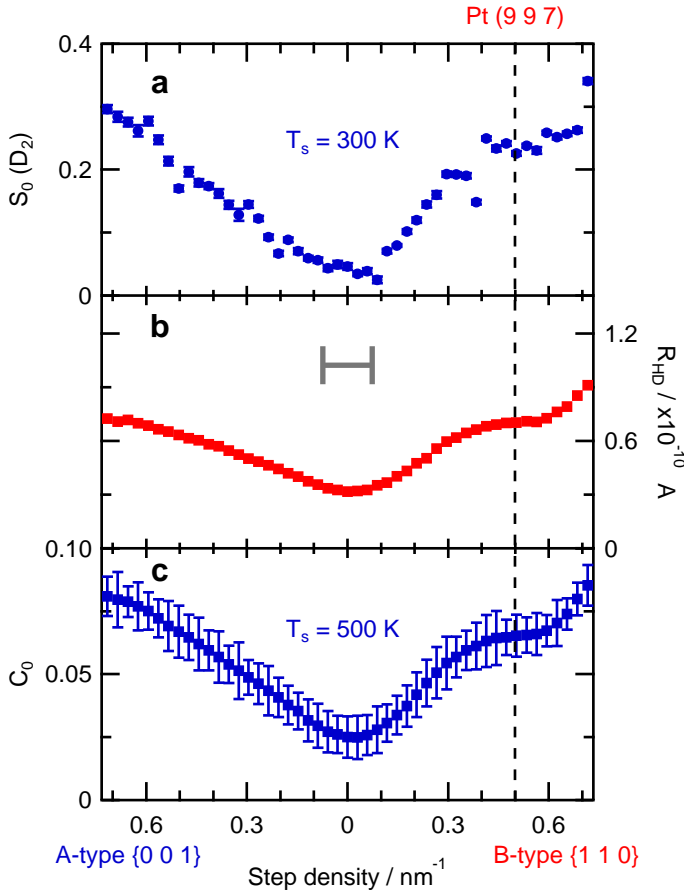


**Figure 4.5:** D<sub>2</sub>  $\bar{S}_0$  at  $T_s = 300$  K. HD formation and  $\bar{C}_0$  measured at  $T_s = 500$  K as a function of step density. The crystal is annealed at 1200 K to induce surface faceting near Pt(9 9 7). The gray horizontal error bar illustrates the 500  $\mu$ m wide beam size convolution.

1200 K and thereby locally facet the sample near (9 9 7)[89], forming extended terraces. Facetting peaks around Pt(4 4 3).[53] The results for  $\bar{S}_0$ , HD rate, and  $\bar{C}_0$  (D<sub>2</sub>) are shown in figure 4.5. Here,  $\bar{C}_0$  (D<sub>2</sub>) are extracted from the D<sub>2</sub> and HD data using the mass balance, as described in appendix C.

Again, at 300 K  $\bar{S}_0$  around Pt(1 1 1) is 0.04-0.05 and we measure  $3 \cdot 10^{-10}$  A for HD formation.  $\bar{C}_0$ (D<sub>2</sub>) is 0.025 during HD formation, as



determined from the HD and D<sub>2</sub> signals.  $\bar{S}_0$ ,  $\bar{C}_0$ , and the HD pressure increase linearly with **A-type** step density. However,  $\bar{S}_0$ ,  $\bar{C}_0$ , and HD formation for **B-type** steps show reactivities that level off around 0.5 nm<sup>-1</sup> step density, or **Pt(9 9 7)**. The larger beam size convolution makes it difficult to pinpoint over what range faceting occurs, but previous results[53] suggest this occurs at **Pt(4 4 3)**. Using the increased signal-to-noise ratio in these data, we calculate the surface structure dependent HD selectivity,  $\eta$ .

Figure 4.6 shows  $\eta$  results in red, as determined from the results from figure 4.5.  $\eta$  is approximately 2-2.5 times higher for Pt(1 1 1) than highly stepped surfaces. For **A-type** step edges, the HD selectivity flattens off at approximately 0.30±0.07 nm<sup>-1</sup> (or 10-17 atom wide terraces). The selectivity for surfaces containing **B-type** step edges also flattens off, but only does so at 0.6 nm<sup>-1</sup> (or 6-8 atom wide terraces). While dissociation probabilities are lower for the faceted **B-type** surface, these surfaces show values for  $\eta$  similar to (1 1 1). Inducing faceting on the **B-type** side improves selectivity towards H-D exchange.

From the model that describes initial reactant dissociation as a linear combination of steps and terraces[70], we construct a similar model for HD production including the extreme cases of surface diffusion. First, dissociation is described as the sum of dissociation at (1 1 1) terraces and steps:

$$\bar{S}_0 = \alpha \cdot S_0^S + (1 - \alpha) \cdot S_0^T \quad (4.12)$$

where  $\alpha$  is the relative abundance of step sites. Second, we invoke this same linear dependence for D<sub>2</sub> consumption, but assume the mixing behavior at steps and terraces changes as discussed previously.  $\bar{C}_0$  is described as the sum of contributions to HD formation by steps and terraces:

$$\bar{C}_0 = \frac{\alpha}{4} \cdot S_0^S + \left( \frac{1 - \alpha}{2} \right) \cdot S_0^T \quad (4.13)$$

where  $\frac{1}{2}$  and  $\frac{1}{4}$  represent  $\eta$  at terraces and steps.  $\alpha$  is determined from the reaction cross sections in chapter 3 for the size of the two types of step

edges. These widths closely resemble the width of the  $\{1\ 1\ 3\}$  and  $\{3\ 3\ 1\}$  microfacets, as shown in appendix C. We then attribute reactivity at **A-** and **B-type** step edges to only the  $\{1\ 1\ 3\}$  and  $\{3\ 3\ 1\}$  facets. We assume that the sticking probability at steps,  $S_0^S$ , is unity as the linear relation of  $\bar{S}_0$  with step density predicts (see appendix C). The sticking probability at the  $(1\ 1\ 1)$  terraces,  $S_0^T$ , is 0.0315 as extracted from the same linear dependence. We thus assume:

$$S_0^S = 32 \cdot S_0^T \quad (4.14)$$

This model predicts surface structure averaged values for  $\eta$ :

$$\bar{\eta} = \frac{\bar{C}_0}{\bar{S}_0} = \frac{7.5\alpha + \frac{1}{2}}{31\alpha + 1} \quad (4.15)$$

We convolute the values by averaging over 0.5 mm to simulate the width of the molecular beam.

Figure 4.6 presents the  $\eta$  results from our model in black. We obtain good agreement with experimental results for high **A-** and **B-type** step density. The model predicts a slight asymmetry due to the larger reaction cross section for **B-type** steps than **A-type** steps. Note that the model does not incorporate the reconstruction centered around **Pt(9 9 7)** and **Pt(4 4 3)**. Consequently, HD exchange is higher there than predicted by the model. Despite large error bars near  $(1\ 1\ 1)$ , a result of the large relative error in  $S_0$ , extended  $(1\ 1\ 1)$  terraces are significantly more selective towards HD formation than predicted by our simple model.

First, we address why  $\eta$  at the  $(1\ 1\ 1)$  surface exceeds the highest expected value of 0.5. Our model does not include any  $T_s$  dependence for reactivity. It assumes  $S_0$  at 300 K and 500 K are identical. While  $T_s$  dependencies reported in literature are generally weak,[18, 66, 68]  $S_0$  increases from 0.12 to 0.14 on Pt(1 1 1) by increasing  $T_s$  from 100 K to 300 K[18], albeit at higher  $E_{kin}$ . If we assume the same  $S_0$  increase at terraces from  $T_s = 300$  K to 500 K, then  $\eta$  lowers by approximately 15% at  $(1\ 1\ 1)$  and agreement with our model improves.

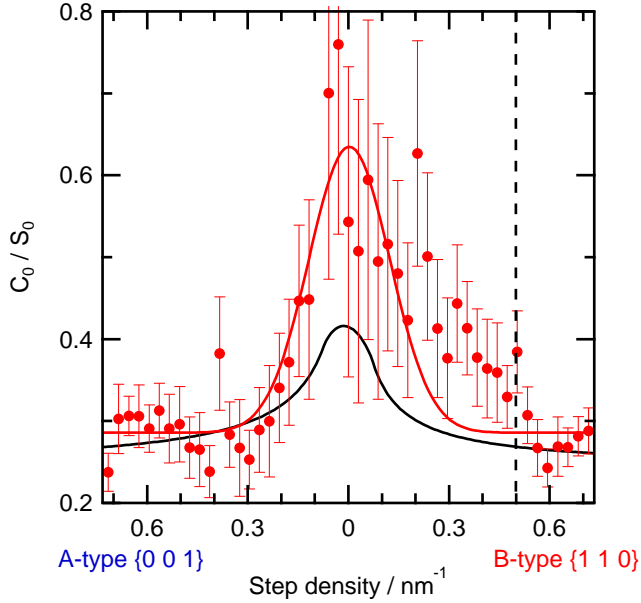


**Figure 4.6:** HD selectivity as a function of step density. Symbols show the data. The solid red line is a Gaussian fit to the **A-type** data to guide the eye. The solid black line is calculated from equation 4.15, which assumes different mixing behavior for dissociation at terraces or dissociation at steps.

A  $T_s$  dependence at steps manifests itself as a decrease in indirect dissociative adsorption at steps,[66] i.e. the reaction cross section of the step edge will be smaller. We do not observe the significant negative correlation of  $S_0$  with  $T_s$ [66] in chapter 3[79] and a  $T_s$  dependence for  $S_0^S$  cannot explain the overall trend. It would reduce the slope in equation 4.12, but the curvature remains.

Second,  $\eta$  is also significantly higher at intermediate **A-type** step density than predicted by our simple model. The model assumes isotopic scrambling occurs between identical sites. We explain deviation at lower step density by diffusion between two different sites, i.e. diffusion from steps onto the terrace. As terraces become wider, scrambling is more probable when  $H_{ads}$  and  $D_{ads}$  can readily diffuse over the (1 1 1) terrace and move farther from the initial reaction site. For narrow terraces,  $H_{ads}$  and  $D_{ads}$

may diffuse orthogonal to the step edge but will quickly return to it.

These results highlight the importance of diffusion in catalytic reactions at surfaces. Heterogeneously catalyzed reactions often exhibit particle size dependencies ascribed to the number of (defect) sites available. Diffusion of intermediates is often neglected. As catalyst particles become smaller, reduced catalytic activity is attributed to electronic effects related to coordination numbers.[93, 94] Our results show that limited diffusion of reactants at small terraces also hinders overall reaction kinetics.

## Conclusion

In conclusion, we have studied the step density dependence of HD formation using a curved Pt(1 1 1) single crystal surface. By comparing initial sticking probabilities with D<sub>2</sub> consumption during H-D exchange, we show that diffusion is essential in HD formation. By facetting a section of the curved surface, we confirm that extended (1 1 1) terraces improve selectivity toward the HD product. A simple model assuming fast diffusion at terraces and no diffusion at steps is in good agreement with our results. These results show that diffusion is integral to the overall reaction mechanism and may be an additional explanation for particle size effects observed in heterogeneous catalysis.

---

**Step-type dependence of oxygen reduction on Pt(1 1 1) surfaces**

---

A model fully ascribes oxygen reduction reactivity on Pt(1 1 1) to a single unknown surface defect, but it disregards the influence of other types of surface defects. Some elementary reaction steps involved are sensitive to step type. Here, we confirm that step defect type indeed influences oxygen reduction by impinging two molecular beams onto two stepped Pt(1 1 1) surfaces containing different step types. The two molecular beams used consist of pure oxygen and a hydrogen-deuterium mixture respectively. Our results show that one step type, {1 1 0} step edges, is more reactive than {0 0 1} steps under oxygen lean reaction conditions. These results show that defect type is an important consideration in reactivity studies that consider the complete reaction mechanism.

## Introduction

Fuels cells are a promising avenue for using renewable energy stored into chemical bonds. One of the biggest challenges in proton exchange membrane fuel cells is rate limiting oxygen reduction at the anode.[95] Reaction rates during catalysis depend on the reaction mechanisms at play, which are strongly influenced by the nature of the catalyst.[96, 97] One of the best catalysts for oxygen reduction is platinum. The current model[98] based on experimental results on Pt(1 1 1) suggests two overall mechanisms take place: sequential addition of  $H_{ads}$  at low temperature ( $T_s$ ) and disproportionation of  $H_2O_2$  that transports  $H_{ads}$  to the active site at elevated  $T_s$ . Eventual water formation is proposed to occur at one single reaction site by varying the defect density through sputtering. Although the model[98] for Pt(1 1 1) points toward defects as the active site, the nature of the active site remains unclear. The sputter approach offers little control in the types of defects present at the surface.[99]

Specific surface sites of catalysts may influence catalytic activity[47] and selectivity[100] of chemical reactions. Ample evidence shows that various elementary steps in oxygen reduction are structure sensitive as well. First, we showed in chapter 3 that dissociative adsorption of  $H_2$  on stepped Pt surfaces exhibits higher reactivity at  $\{1\ 1\ 0\}$  (B-type) step edges than  $\{0\ 0\ 1\}$  (A-type) steps.[79] Second,  $O_2$  sticking probabilities for the two step types differ with incident energy ( $E_{kin}$ )[101, 102] and molecular orientation[27]. Third, desorption energies for hydrogen, oxygen, and water differ for the two step types.[51] Thermal desorption of co-adsorbed water and oxygen suggests that OH formation, the key intermediate to water formation, favors B-type steps over A-type.[103] These observations make it likely that water formation from hydrogen and oxygen is step type dependent as well.

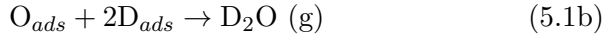
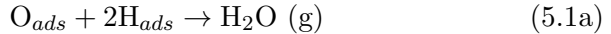
Here, we investigate whether oxygen reduction is step-type dependent by reacting oxygen with a mixed  $H_2/D_2$  beam on oxygen-covered Pt(3 3 5) and Pt(5 5 3) surfaces. B-type steps of Pt(5 5 3) exhibit significantly higher  $O_2$  reaction probabilities than A-type steps of Pt(3 3 5) under similar

conditions despite having a lower step density. After  $O_{ads}$  depletion under hydrogen rich conditions,  $O_2$  sticking probabilities (S) resemble the initial sticking probabilities ( $S_0$ ) on the clean surface. Our results suggest that neither step-type requires significant  $\theta_O$  to catalyze the reaction. Higher **B-type** sticking probabilities during the reaction show structure sensitivity for water formation.

## Method

The experiment is schematically illustrated in figure 5.1. The **Pt(3 3 5)** and **Pt(5 5 3)** surfaces are precovered in  $O_{ads}$  using a supersonic molecular beam of  $O_2$ , depicted in red. Afterwards, a 1:1 mixed  $H_2:D_2$  beam impinges the sample simultaneous to the  $O_2$  beam. The incident  $H_2$  and  $D_2$  dissociate and subsequently react with  $O_{ads}$  to form water for 30 s. Subsequently, the  $O_2$  beam flag is closed so that remaining  $O_{ads}$  is titrated by the hydrogen beam.

With the surfaces covered (but not saturated) with  $O_{ads}$ , they are subsequently exposed to both a supersonic  $O_2$  and effusive hydrogen beam. The latter consists of equal amounts of  $H_2$  and  $D_2$ .  $H_2$  and  $D_2$  dissociate and may either react with adsorbed oxygen to form one of three isotopologues of water:



or scramble to recombinatively desorb as one of three isotopologues of dihydrogen:



Due to the molecular beam sizes, reaction 5.2 occurs in both area 1 and 2 (see figure 5.1), while reaction 5.1 only takes place in area 1. This is

confirmed by deconvoluting the HD signal in appendix D, showing that reaction 5.2 indeed only occurs in area 1 upon complete removal of  $O_{ads}$ . Similar behavior was observed previously for Pt(1 1 1).[104] Henceforth, we shall only consider reactivity by area 1. Further experimental details are provided in appendix D. The  $O_2$  and HD signals yield direct and indirect evidence of the surface reactions at play:

$$R_{H_2O} \propto \frac{dP_{H_2O}}{dt} \propto -\frac{1}{2} \frac{dP_{O_2}}{dt} \propto -\frac{dP_{H_2}}{dt} \quad (5.3)$$

where R is the reaction rate.

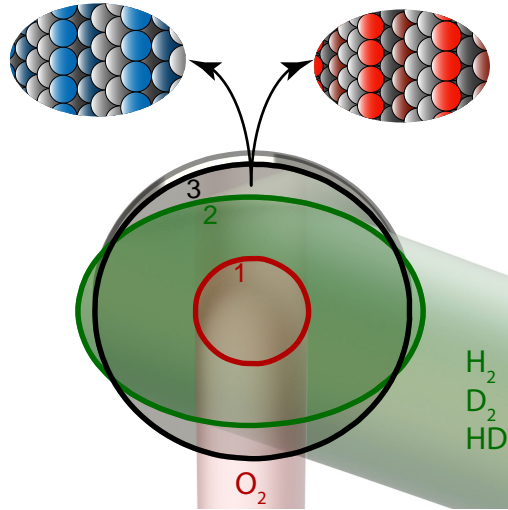


**Figure 5.1:** Schematic overview of the experiment. Area 1 of the surface is precovered with the supersonic  $O_2$  beam (red), and the effusive  $H_2/D_2$  beam (green) subsequently reacts with the adsorbed oxygen. Area 2 comprises the surface that is impinged by the effusive beam but is not precovered with  $O_{ads}$ . Area 3 is not impinged directly by either beam. Experiments are performed on Pt(3 3 5) (left) and Pt(5 5 3) (right) surfaces at a surface temperature of 500 K.

## Results and Discussion

Figure 5.2 shows signal-averaged time-dependent  $O_2$  sticking for the Pt(3 3 5) and Pt(5 5 3) surfaces, as measured using the King and Wells



method.[11] This is a pure room temperature expansion of  $O_2$ . The fit to the time of flight can be found in appendix D. The sticking behavior is representative of dissociative adsorption of  $O_2$  on stepped Pt surfaces.[27, 101, 102] The  $O_2$  sticking probability quickly drops over time as the  $O_{ads}$  coverage ( $\theta_O$ ) increases. Hence,  $O_2$  sticking probabilities for both stepped surfaces are sensitive to coverage. Initial sticking probabilities ( $S_0$ ) are extracted by fitting the data with a double exponential fit and extrapolating to the beam flag opening at  $t = 0$ . [27, 102] With sticking probabilities of 0.35 and 0.25,  $S_0$  for **Pt(5 5 3)** exceeds that of **Pt(3 3 5)** under these conditions ( $T_s = 500$  K,  $E_{kin} = 82$  meV). Sticking on **Pt(5 5 3)** agrees well with previous results for low  $E_{kin}$  at  $T_s = 500$  K.[102] Sticking at **Pt(3 3 5)** appears somewhat lower, which may be a result of a difference in  $E_{kin}$  distribution with previous results.[101]

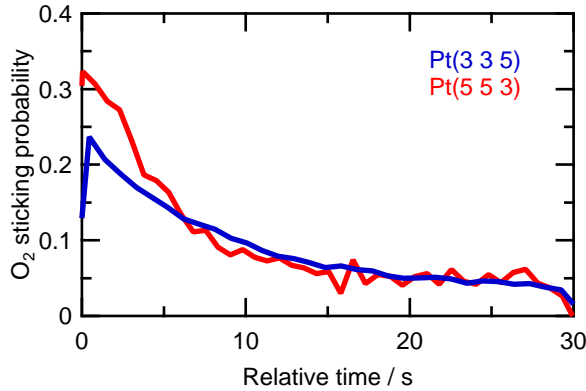


**Figure 5.2:**  $O_2$  time-dependent sticking traces for the clean **Pt(3 3 5)** (blue) and **Pt(5 5 3)** (red).

Figure 5.3 shows the reactivity of area 1 for **Pt(3 3 5)** (left) and **Pt(5 5 3)** (right) as a function of time (horizontal axis), and O:H ratio in the zero coverage limit (vertical axis). Panels a and b show the change in  $O_2$  sticking probability, whereas panels c and d report water formation measured through the variation in HD production. Attached to the four panels are  $O_2$  sticking and  $R_{H_2O}$  curves exemplifying low (both) and high ( $R_{H_2O}$ ) O:H ra-

tios. We explain the relation between water formation and HD production before discussing the results.

Dissociative adsorption of  $O_2$ ,  $H_2$ , and  $D_2$  leaves  $O_{ads}$ ,  $H_{ads}$ , and  $D_{ads}$  on the surface. Our experiment is insensitive to recombinative desorption of  $2H_{ads}$  and  $2D_{ads}$  forming  $H_2$  and  $D_2$ . [11] Only  $H_{ads}$  and  $D_{ads}$  that end up forming HD or water do not return as  $H_2$  and  $D_2$ . Hence, the measured total reaction rate ( $R_{total}$ ) results from  $H_{ads}$  and  $D_{ads}$  reacting to form either HD or a water isotopologue. We split the total reactivity into reactivity along equation 5.1 ( $R_{H_2O}$ ) and equation 5.2 ( $R_{HD}$ ).  $R_{HD}$  is equal to  $2 \cdot R_{H_2}$  and  $2 \cdot R_{D_2}$ , assuming no isotope effect and isotropic mixing of H and D atoms. Chapter 4 shows this to be the case for (1 1 1), but not for (3 3 5) and (5 5 3). However,  $R_{HD}$  is then still proportional to the total rate of recombinative desorption of  $H_2$ ,  $D_2$ , and HD.

We assume the same for water formation.  $R_{HDO}$  reflects water formation for all isotopes. When normalizing the total rate, recombinative desorption rate, and water production rate ( $\hat{R}$ ), we may state:

$$\hat{R}_{HD} + \hat{R}_{H_2O} = 1 \quad (5.4)$$

Therefore, changes in  $\hat{R}_{HD}$  directly reflect the change in  $\hat{R}_{H_2O}$  by

$$\hat{R}_{H_2O} = 1 - \hat{R}_{HD} \quad (5.5)$$

In other words, H and D atoms not returning as  $H_2$  or  $D_2$  must have reacted to form either HD or an isotopologue of water. We normalize HD production by considering that HD production is maximized when area 1 is completely depleted of  $O_{ads}$ .

At 0 s in figure 5.3, the combination of the two beams initiates water formation via reaction 5.1. Panels a and b show that  $O_2$  sticking gradually increases over time for both Pt(3 3 5) and Pt(5 5 3) upon impinging the hydrogen beam. For low hydrogen flux,  $O_2$  sticking increases only to approximately 0.02. In contrast,  $O_2$  sticking reaches 0.25 and 0.35 for Pt(3 3 5) and Pt(5 5 3) within 5 s, as illustrated by the two example traces.  $O_2$  sticking is consistently higher for Pt(5 5 3) than Pt(3 3 5).

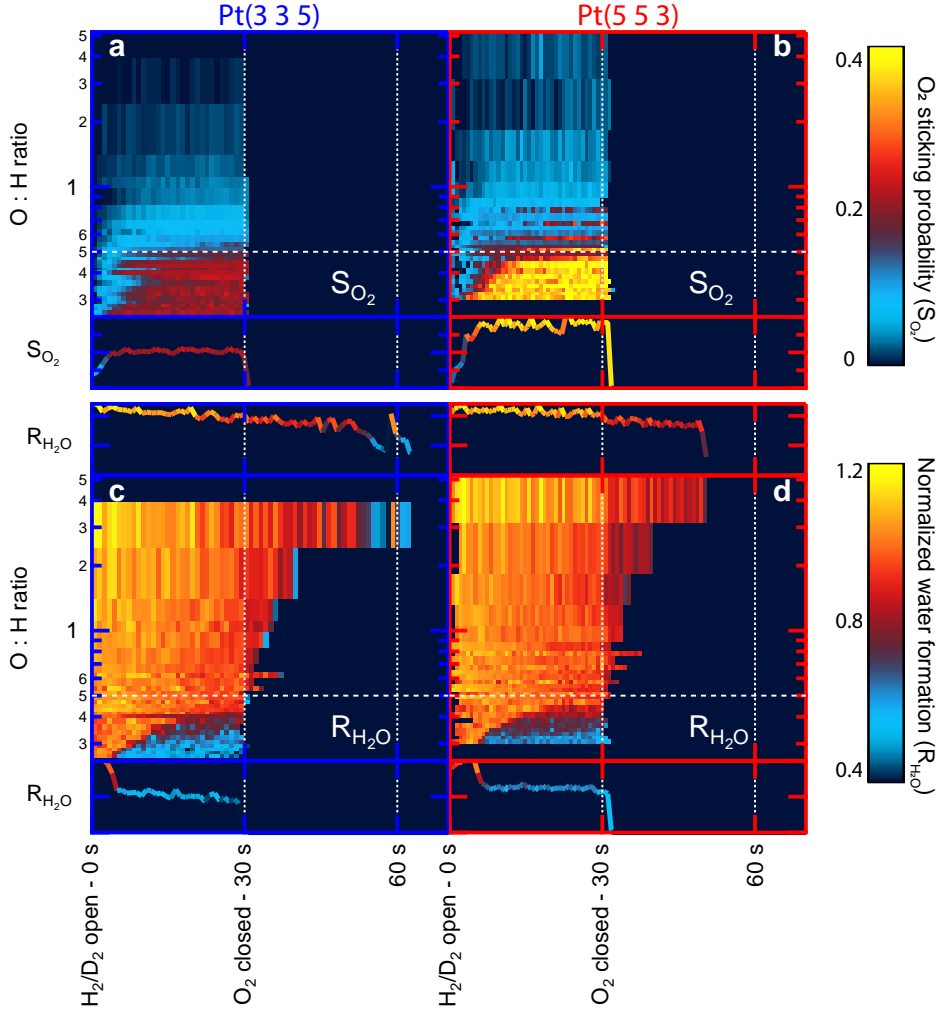


**Figure 5.3:** Comparison of  $O_2$  sticking (top panels) and normalized water formation (bottom panels),  $R_{H_2O}$ , for Pt(3 3 5) (blue axes) and Pt(5 5 3) (red axes) measured as a function of time (bottom axes) and O:H ratio available for reaction at the clean surface (left axes). Normalized water production in panels c and d are extracted from HD formation (see text). At 30 s, the  $O_2$  beam is discontinued. Shown for clarity are the  $O_2$  sticking and  $R_{H_2O}$  traces for the lowest O:H ratio and the  $R_{H_2O}$  traces for the highest O:H ratio.

Panels c and d show that all initial hydrogen dissociation in area 1 of figure 5.1 leads to reaction 5.1. The data suggest that a rather constant flux of water forms for some time. Water formation occurs until 50 s for Pt(5 5 3) and well past 60 s for Pt(3 3 5) for hydrogen poor experiments, as exemplified by the top panels. With increasing hydrogen, the quick drop in water formation occurs earlier and converges to 30 s, i.e. where the incident O<sub>2</sub> flux is stopped.

The nearly constant water formation implies that most adsorbed hydrogen, which may potentially form HD by reaction 5.2, is consumed instead by reaction 5.1. An additional increase in  $\hat{R}_{HD}$  reveals a drop in  $\hat{R}_{H_2O}$  prior to 30 s if the hydrogen flux is sufficiently high. This behavior is exemplified by the two lower  $\hat{R}_{H_2O}$  panels. There, in contrast to the constant initial  $\hat{R}_{H_2O}$  observed for low hydrogen flux, a fraction of hydrogen ends up in reaction 5.2. Note that simultaneous to this drop in HD consumption, O<sub>2</sub> sticking in the top panels approximates S<sub>0</sub>. Therefore, a steady state sets in upon complete O<sub>ads</sub> removal, where reaction 5.1 becomes O<sub>ads</sub> limited. As discussed previously, remaining hydrogen undergoes reaction 5.2. Appendix D details how we extract the O:H ratio from the O<sub>ads</sub> limited data and extrapolate the O:H ratio to excess oxygen data.

We now compare how the time required to deplete the surface of O<sub>ads</sub> depends on the O:H ratio for the two stepped surfaces. Figure 5.3 shows that the O<sub>2</sub> sticking probability increases as O<sub>ads</sub> is removed with both time and H flux. Figure 5.4 shows the time required to remove all adsorbed oxygen from the surface as a function of the O:H ratio. Essentially, it follows the transition from orange to red/blue in  $\hat{R}_{H_2O}$  in figure 5.3. Less time is required to remove all O<sub>ads</sub> for Pt(5 5 3) (red) than Pt(3 3 5) (blue). The data show two linear regimes. Under oxygen lean conditions, approximately 5 s are required to remove all O<sub>ads</sub> from O<sub>ads</sub> buildup prior to impinging the hydrogen beam. As the relative amount of oxygen increases, so too does the time required to deplete the surface of O<sub>ads</sub>. For O:H ratios approaching 0.5, approximately 30 s is required to consume all O<sub>ads</sub>. At 30 s, the incident O<sub>2</sub> beam is discontinued and O<sub>ads</sub> is no longer replenished

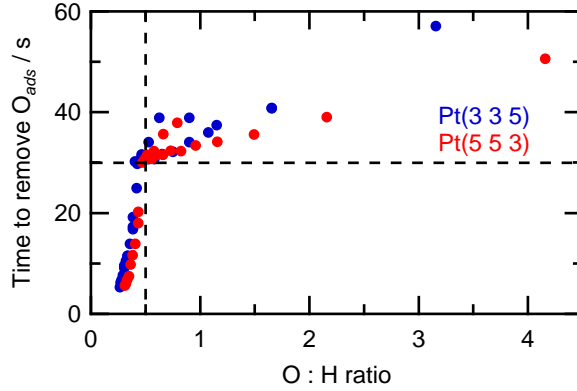


**Figure 5.4:** Reaction time required to remove all  $O_{ads}$  as a function of the oxygen-hydrogen ratio (see text) for Pt(3 3 5) (blue) and Pt(5 5 3) (red).

by the molecular beam. Consequently, a second regime is observed with a diminished slope. There, the hydrogen beam titrates remaining  $O_{ads}$  from the surface.

Figure 5.5 shows  $O_2$  sticking in steady state, just prior to discontinuing the  $O_2$  beam.  $O_2$  reactivity matches  $S_0$  fairly well for both surface under oxygen-lean conditions. As the O:H ratio increases in excess of 0.5,  $O_2$  sticking decreases.

The overall reactivity behavior presented here closely resembles that of earlier titration and Molecular Beam Relaxation Spectroscopy results on Pt(1 1 1).[98, 104]  $H_{ads}$  selectively reacts with  $O_{ads}$  present at the surface. Upon complete  $O_{ads}$  removal, a steady state sets in where any incident  $O_2$  that dissociates is immediately removed by  $H_{ads}$ . Excess  $H_{ads}$  (and  $D_{ads}$ ) undergoes recombinative desorption.

In spite of lower step density, Pt(5 5 3) exhibits higher reactivity than Pt(3 3 5) under oxygen lean conditions. Higher Pt(5 5 3) reactivity towards reaction 5.1 is twofold. First,  $O_2$  sticking under oxygen-lean conditions matches  $S_0$ , which is significantly higher for Pt(5 5 3). Second, higher

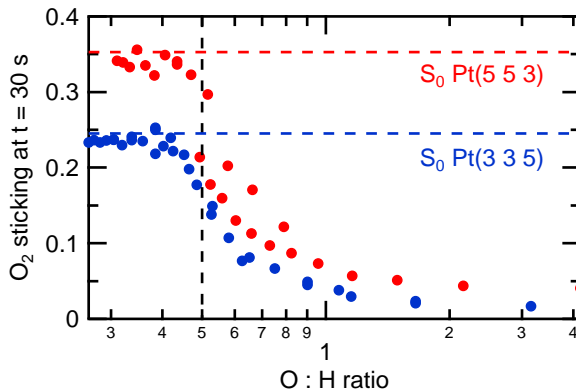


**Figure 5.5:**  $\text{O}_2$  sticking prior to closing the  $\text{O}_2$  flag at 240 s as a function of the oxygen:hydrogen ratio (see text) for  $\text{Pt}(3\ 3\ 5)$  (blue) and  $\text{Pt}(5\ 5\ 3)$  (red).

probabilities for  $\text{O}_2$  sticking on  $\text{Pt}(5\ 5\ 3)$  than  $\text{Pt}(3\ 3\ 5)$  are incorporated in the O:H ratio, yet  $\text{Pt}(5\ 5\ 3)$  is depleted of  $\text{O}_{ads}$  faster than  $\text{Pt}(3\ 3\ 5)$ . This suggests more hydrogen is available at the surface to react with  $\text{O}_{ads}$  to form water. Sticking of  $\text{H}_2$  on O-covered  $\text{Pt}(3\ 3\ 5)$  is lower than the clean surface.[104, 105] This site blocking effect may be smaller for **B-type** steps, but requires further investigation beyond the scope of this study. Clearly, reactivity is structure sensitive.

The similarity of sticking under oxygen lean conditions and initial sticking at the clean surface suggests that little to no  $\text{O}_{ads}$  remains behind at the surface. It seems unlikely that a step edge with subsurface oxygen[98] is the active site, although we cannot completely rule this out. Our results clearly show that defect type is an important consideration in reactivity studies. Such details are currently lacking in the model for  $\text{Pt}(1\ 1\ 1)$  and results in a more complete description of reactivity at Pt surfaces.

Use of a supersonic molecular  $\text{O}_2$  beam calls into question how our results compare to catalysis under realistic conditions. The subset of molecules present in our pure  $\text{O}_2$  beam are certainly available under reaction conditions. However, the narrow energy distribution of our beam necessi-

tate further study considering the energy dependence of the reaction. For example, **Pt(5 5 3)** is more reactive towards  $O_2$  dissociation in the present study at lower  $E_{kin}$ , but **Pt(3 3 5)** becomes significantly more reactive at higher kinetic energy.[101, 102]

Two other issues presented in the Pt(1 1 1) model remain unresolved. First, the model[98] proposes that all water forms at defects. Rate limiting  $O_{ads}$  diffusion towards defects cannot be identified from our results. Our experiments lack the temporal resolution of the Pt(1 1 1) experiments and the use of **Pt(3 3 5)** and **Pt(5 5 3)** single crystals does not allow variation of the step density. Second, the nature of the active site for oxygen reduction remains unresolved. Verheij[98] suggests kinks or oxygen-modified step edges may be responsible. Both issues may be resolved by adapting our apparatus that has combined molecular beam studies (this chapter) and tunable defect density of curved single crystals[27, 79](chapters 3 and 4), to also accommodate scattering experiments. In this manner, Molecular Beam Relaxation Spectroscopy may be performed as a function of **A-** and **B-type** defect density, extracting rate limiting  $O_{ads}$  diffusion[98]. By using two different curved Pt(1 1 1) samples – one with **A-** and **B-type** steps, the other with kinked surfaces – site-specific effective rate constants may be extracted for the three types of sites. This would unequivocally resolve the nature of the active site and how **A-type**, **B-type**, and kink density affects the effective rate constant.

## Conclusion

In conclusion, we measured oxygen reduction reactivity for **Pt(3 3 5)** and **Pt(5 5 3)** using two molecular beams. Our results show that step type impacts reactivity, with higher reactivity for **B-type** steps on **Pt(5 5 3)** than **A-type** steps on **Pt(3 3 5)**. These results highlight the importance of considering every possible reaction site available at the surface. Future studies should focus on the effect of step type and kinks on  $O_{ads}$  diffusion, the effective rate constant, and overall reactivity.





---

**Applying reflection absorption infrared spectroscopy on a curved surface – how do step-type and step density influence CO adsorption on stepped Pt(1 1 1)?**

---

The varying step density of curved single crystal surfaces has many benefits for studying surface structure dependencies in surface science. Vibrational spectroscopy is a powerful tool for identifying reaction intermediates and their binding sites. However, the curved nature of the surface also introduces new experimental challenges when applying vibrational spectroscopy. During Reflection Absorption Infrared Spectroscopy (RAIRS), the curved surface acts as a strongly divergent convex cylindrical mirror. We resolve this problem by placing a concave cylindrical mirror directly downfield of the curved surface, essentially forming an anamorphic beam expander. As proof-of-principle, we apply RAIRS to a curved Pt(1 1 1) surface and resolve how steps influence CO adsorption.

## Introduction

Commercial heterogeneous metal catalysts contain a wide array of surface defects, such as adatoms, steps, and kinks. For several of the largest industrial processes, monatomic steps on catalyst particles are crucial to the kinetics of the overall process.[106, 107] Therefore, fundamental studies using macroscopic single crystals to mimic actual catalyst particles need to include such surface defects. A single crystal can be cut to expose a vicinal plane of well-defined surface structure for this purpose. While low Miller index surfaces are most commonly studied, high Miller index surfaces – which expose regularly spaced straight or kinked steps separated by atomically flat terraces – can also be formed. Studies attempting to bridge the ‘structure gap’ between ordered samples used in surface science and real catalysts were recently reviewed by Vattuone.[29] A variation on this traditional surface science approach is to exploit the variety of step types, step density, and terrace types offered by curved single crystal surfaces. [32]

Simultaneously, vibrational spectroscopy is ideal in identifying molecular adsorbates and reaction intermediates. In reflection absorption infrared spectroscopy (RAIRS), the absorption bandshape and oscillator strength carry information on the structure and chemical environment of adsorbates – most importantly, relative coverage and the nature of adsorption sites can be identified, e.g. high- or low-coordinated on-top, bridge and/or hollow sites.[108, 109] Typically, the traditional surface approach is applied, where a flat single crystal surface is placed between the interferometer and detector of a commercial Fourier Transform Infrared (FTIR) spectrometer. Benefits include ease of instrumentation, rapid acquisition time (commonly less than 30 s), and high energy resolution (typically  $2\text{ cm}^{-1}$ ,  $< 0.1\%$  of a stretching vibration). RAIRS is a prominent surface science technique.[110, 111] However, it cannot be used for curved surfaces without modification, since the curved surface acts as a convex cylindrical mirror.

In the present work, a traditional RAIRS setup is adapted for use with curved single crystal surfaces by forming an anamorphic beam expander

with the curved surface and a gold-coated concave cylindrical mirror. We present a brief literature review of CO adsorption on stepped Pt surfaces before showing proof-of-principle experimental results on the same system. Finally, the experimental results are discussed and improvements to the current setup are suggested.

## Experimental details

The experiments were carried out in Boxfish. The curved Pt single crystal surface and the UHV apparatus are described in chapter 2. Here, we describe the design for performing RAIRS on a curved surface. Figures 6.1a, b, and c illustrate the concept. RAIRS is performed at grazing incidence (roughly  $85^\circ$ ) using p-polarized light, since s-polarized light does not contribute to absorption at a metal surface. We follow the usual implementation by placing the sample at the focus of a paraboloid represented by two  $90^\circ$  off-axis mirror segments ( $f = 203$  mm) outside of the vacuum chamber. One focuses the IR beam onto the sample, while the other re-collimates it for eventual imaging at the detector. The sample is oriented with its cylindrical axis parallel to the horizontal optical axis. Consequently, the sample does not affect imaging in the plane of incidence, i.e. where the sample has an effective focal length ( $f$ ) of infinity. However, the curved surface does scatter optical power out of the plane of incidence ( $f = -7.5$  mm). Therefore, we place a concave cylindrical mirror downfield of the sample to freeze the expansion. The mirror is coaxial with the sample, but has a focal length that is greater ( $f = 8.0$  mm) by the transverse distance separating the sample and mirror, 1.0 mm. The pair therefore act as an anamorphic beam expander. This effectively translates the optical axis by 1.0 mm in the plane of incidence and magnifies the beam by 16/15 normal to the plane of incidence. An advantage of this double-reflection geometry over traditional RAIRS is that the sample introduces no angular deviation to the infrared beam. As a consequence, the spectrometer and detector can be aligned without the sample present. The focus quality on the sample is determined entirely by alignment of the upstream paraboloid. Misalignment of the collimator can at worst distort the source image enough that it

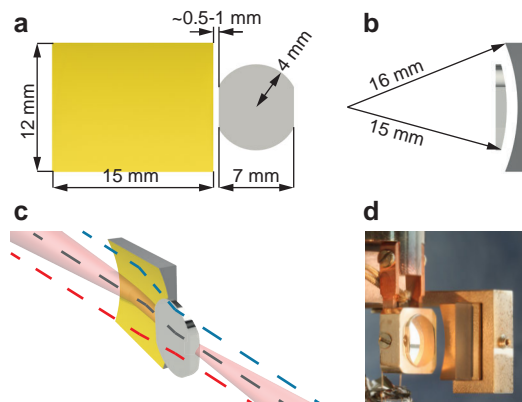


**Figure 6.1:** a) Front view facing the gold coaxial collimator and back of the curved platinum crystal. The gold collimator is placed approximately 0.5 to 1 mm downfield of the sample. b) View of the coaxial collimator and curved crystal surface along the optical axis. The surfaces are separated by 1.0 mm in the radial direction c) A birds-eye view illustrating the optical path after reflecting off different parts of the sample. Starting on the right, IR light passes through an aligned set-up. Extra divergence from the curved platinum surface is "frozen" by the coaxial collimator. Blue, gray, and red dashed lines represent example optical axes reflecting off surfaces containing **A-type** steps, (1 1 1), and **B-type** steps respectively. d) Image of the adapted sample holder facing the curved platinum surface.

spills over the detector element, thereby reducing the infrared throughput and sensitivity. In practice, double-reflection throughput was comparable to no-sample throughput. The mirror is a fused-silica substrate evaporatively coated with gold; an image of the mirror and crystal is shown in figure 6.1d.

Inside the UHV system, the coaxial collimator and sample holder are both connected to the cryostat. Consequently, they move in tandem. The mirror holder is isolated from the sample holder, thereby protecting the coaxial collimator from elevated temperatures. The sample and mirror (12 mm x 15 mm) are offset by approximately 1 mm along the optical axis. Hence, they do not overlap in the surface-normal direction. Alignment of the collimator relative to the surface is performed outside of vacuum using a HeNe laser.

Since the gold coated coaxial collimator is also cooled to cryogenic temperatures, adsorption may occur there as well. Potential contributions from adsorption to the coaxial collimator are monitored by regularly measuring transmission spectra of clean surfaces. For each vicinal surface, transmission is measured before each CO exposure. Since the coaxial collimator is attached directly to the cryostat, CO adsorption on the gold surface during the CO exposure should remain constant throughout the experiment for that vicinal surface. Transmission spectra before and after experiments show no features suggesting CO adsorption on gold within the sensitivity of our experiment.

A reference point at the sample must be found to perform RAIRS at specific surface structures. We find the (1 1 1) apex by placing the sample parallel to the incident IR beam and translating vertically and horizontally while monitoring transmitted IR signal on the detector. When the intensity reaches a sharp minimum with vertical motion, the beam focus is incident at the (1 1 1) apex of the sample. Once the apex is found, vicinal surfaces can be found by simply calculating their position relative to (1 1 1) using the crystal geometry ( $r = 15$  mm) and the angle between the desired Miller index and (1 1 1). In the setup, the position of the manipulator can be adjusted in steps of  $10\text{ }\mu\text{m}$  in the vertical plane and in steps of  $5\text{ }\mu\text{m}$  in the horizontal plane.

Alignment is aided by a selectable tungsten filament light source inside the spectrometer. This source creates a visible-light replica of the IR beam to use for alignment. Figure 6.2 shows three images observed 2.5 m after the exit window of the UHV system. Figure 6.2a shows light traveling through the UHV system without reflecting off the sample or the mirror. This straight-through configuration is observed as a single vertical ellipse. Because the sample is oriented with its cylindrical axis in the optical plane of incidence, the infrared footprint is elongated in the axial direction, along which there is no variation in surface structure. Step density is varied by raising or lowering the entire cryostat/sample/collimator assembly with respect to the optical axis. The beam path does not change once set. The

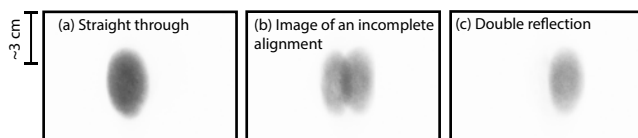


**Figure 6.2:** Gray scale images of the alignment process with the tungsten light source inside the spectrometer. Light exiting the UHV chamber reflects off the collimating parabolic mirror at the exit window and is made visible after 2.5 m. The images show: a) light traveling through the UHV chamber without reflecting off the sample or the coaxial collimator, b) light partially reflecting off both surfaces, c) light reflecting only off both surfaces.

sample is set to the correct height so that the IR beam probes the desired step density. Figure 6.2b shows a portion of the light also reflecting off the sample and collimator; a second ellipse appears alongside the original one. Subsequently, the sample is aligned in the horizontal plane to compensate for the curvature of the surface and to obtain a pure double reflection at each vertical position. This is achieved by translating the sample across the visible beam until only the double reflection can be observed. Figure 6.2c illustrates an exemplary alignment with only the reflected vertical ellipse visible.

While generally unimportant for traditional flat single crystal surfaces, spatial resolution of experimental techniques is a key parameter for curved surfaces. It defines the range of surface structures probed. To determine the spatial resolution, we assume a Gaussian beam profile and measure the beam width at the sample position using the 'knife edge' technique. The sample is replaced by a knife edge placed perpendicular to the optical axis. The spatial resolution can be measured at different positions along the beam path by moving the knife edge into the beam path in steps and measuring the position-dependent transmission.[112] At the sample position, the beam was determined to have a FWHM = 0.72 mm. Consequently, the step density convolution is approximately  $\pm 0.11 \text{ nm}^{-1}$ . This size is a result of the 0.5 mm source pinhole magnified by the collimator within the FTIR ( $f = 100 \text{ mm}$ ) and the sample focus paraboloid ( $f = 203.2 \text{ mm}$ ).

## Literature review of CO adsorbed to platinum surfaces

We now present a short literature review on CO as a basis for the upcoming results. CO adsorption on platinum is a thoroughly studied model system – a prototype for fundamental processes at catalytic metal surfaces.[113, 114] A low CO coverage on Pt(1 1 1) forms a  $(\sqrt{3} \times \sqrt{3})R30^\circ$  structure. CO chemisorbs carbon down at on-top binding sites. As the CO coverage increases, bridge sites also become occupied[115–117] and the structure evolves into a mixed on-top/bridge  $c(4 \times 2)$ . [115, 118] Scanning tunneling microscopy results confirm the formation of  $(\sqrt{3} \times \sqrt{3})R30^\circ$  hexagonal island superstructures and rectangular  $c(4 \times 2)$  domains at low and high CO coverage respectively.[119] In the range of 0.3 to 0.5 ML, RAIRS has played a crucial role in unraveling CO adsorption structures; the absorption peak of on-top adsorbed CO is sensitive to structural homogeneity of the adsorbate overlayer.[120, 121]

On high Miller index surfaces, on-top and bridge sites at step edges are both populated. In contrast to Pt(1 1 1), terraces often do not contain equal bridge and on-top site occupation at saturation on stepped surfaces. Possible superstructures are limited due to the finite terrace size.[122] On-top sites at steps are most favorable for initial adsorption,[122–126] followed by bridge sites at steps.[125] Once bridge and on-top step sites are fully occupied, increasing CO coverage follows the same pattern as Pt(1 1 1). CO adsorbed on Pt(1 1 1) terraces has low diffusion barriers. Consequently, migration of CO from terraces to thermodynamically favorable steps can occur below 100 K, the minimum surface temperature of the present work.

The effect of **A-** and **B-type** steps on bridge and on-top binding energies have been studied with XPS.[125] Tränkenschuh compared Pt(2 2 3) and Pt(5 5 3), which contain five and four atom wide (1 1 1) terraces with differing step types, **A-** and **B-type** respectively.[125] Both bridge and on-top adsorption sites were occupied on **A-type** steps, whereas only on-top sites were observed on **B-type** steps. Accordingly, higher step coverage was observed on **B-type** steps. By temperature programmed desorption (TPD),

it was found that on-top bound CO binds more strongly to **B-type** steps. On **A-type** steps, binding to bridge sites was found to be weaker than to the on-top. Relative occupation for step and terrace sites as a function of coverage and temperature were also found to differ with step type. Little effect was observed on **Pt(5 5 3)**, whereas large changes were observed on **Pt(2 2 3)** with temperature at a given coverage. This can be attributed to contrasting interactions due to binding energy differences on step types.

One previous study of CO adsorption on a curved Pt surface has been reported by Walter.[36] The curved single crystal surface was of a similar design as used throughout this thesis: a rectangular section was cut and polished to expose (1 1 1) at the apex, separating stepped surfaces containing **A-** and **B-type** steps. Using XPS with high spatial resolution (100  $\mu\text{m}$ ), the preferred CO site occupation was observed – i.e. step versus terrace sites and on-top versus bridge sites – confirming the previously reported hierarchy. No change in absolute coverage was found for terrace length or step type as a function of dose. However, the distribution of adsorption sites did change. CO diffusion from terraces to steps was measured as a function of terrace width for different exposures. The curved surface combined with XPS was also used to accurately measure room temperature CO saturation at different exposures.

RAIRS is an especially effective technique for studying CO adsorption on platinum surfaces. The molecule has a strong stretching mode and is sensitive to the manner in which it binds to the surface. As a result, it has strong absorption and distinguishable frequency shifts in combination with the benefit of *ex-situ* optical spectroscopy.[108, 109, 120–122] The experimental parameters (0.72 mm beam waist and 7  $\text{cm}^{-1}$  instrument function) are a compromise between light intensity, spatial resolution, and spectral resolution.



## Results

Figure 6.3a schematically shows the curved Pt single crystal. The (1 1 1) apex separates stepped surfaces containing **A-type** steps at the top (blue) and **B-type** steps (red) at the bottom. LEED was used to verify the surface structure across the curved surface at nine different positions. The LEED pattern of stepped surfaces is determined by the terrace width and step height. By probing along the curved surface with the incident electron beam, the spot splitting to row spacing ratio in the LEED pattern increases with step density.[35] Figure 6.3b shows the spot splitting to row spacing ratio as a function of angle. The spot splitting to row spacing ratios observed agree with those previously reported by van Hove.[127] The Miller indexes are included at their respective angle with (1 1 1). The corresponding step type – blue for **A-type** (or {0 0 1}) and red for **B-type** (or {1 1 0}) – and terrace widths are indicated in figure 6.3c. The RAIRS spectra are shown in figure 6.3d.

Before discussing the transmission spectra, a note on absorption in RAIRS may be helpful. Light attenuation is described with the Beer-Lambert Law,  $I = I_0 e^{-\sigma a}$ .  $I_0$  and  $I$  are transmission intensities through the optical set-up.  $I_0$  measured after reflection off a clean surface and  $I$  measured following reflection off a CO covered surface.  $\sigma$  and  $a$  are the absorption cross-section of CO (in units of  $\text{m}^2$ ) and surface density of CO (in units of  $\text{m}^{-2}$ ). In the case of high or low Miller index surfaces, CO can adsorb in multiple positions, as described above. CO forms an anisotropic distribution on the surface, while the platinum surface is isotropic for both low and high Miller index surfaces. In a simple application of the Beer-Lambert law, the individual contribution of different states is ignored and  $\sigma$  is an effective frequency dependent absorption cross-section, linearly proportional to the sum of individual contributions. Adsorbed CO molecules do not interact and are dispersed over a featureless flat surface. In the case of a curved single crystal, the platinum surface is inhomogeneous perpendicular to the cylindrical axis. Due to the finite size of the IR beam, absorption by CO occurs from a range of surface structures. We apply

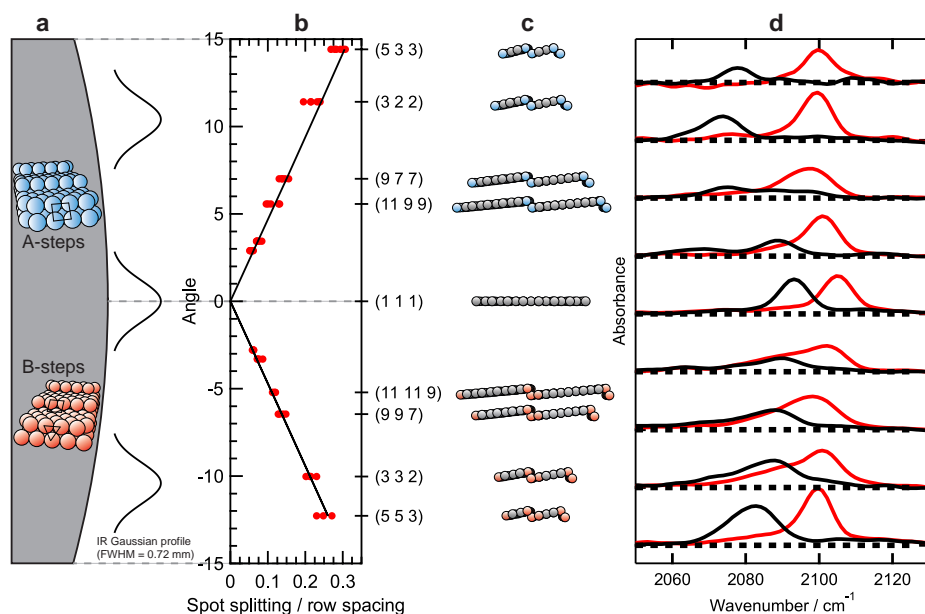


**Figure 6.3:** a) Curved platinum single crystal surface. The (1 1 1) surface is located at the apex of the crystal. On either side are **A-** (blue, top) or **B-type** (red, bottom) steps separated by (1 1 1) terraces (grey). Gaussian profiles indicate the size of the focus of the IR beam. b) LEED spot splitting to row spacing ratio as a function of angle with (1 1 1). c) Corresponding average surface structure at the indicated position. d) RAIRS spectra of on-top adsorbed CO measured at surface structures shown in c). RAIRS spectra were recorded at 100 K for each position after flashing the crystal to 300 K (red) and 400 K (black).

the Beer-Lambert law in the same manner:  $a$  is the surface density of CO on a flat featureless surface and  $\sigma$  is an effective absorption cross section of a non-interacting molecule. However, implicit insight from systematic changes in spectra as a function of step type and step density can be found, such as oscillator strengths and frequency shifts.

Background spectra of the clean surface were obtained at the nine mentioned sample positions from figure 6.3c. The Pt surface was subsequently exposed to 0.75 Langmuir (100 s at  $1 \times 10^{-8}$  mbar) of CO at 100 K. Next, infrared absorption was measured. The sample temperature was increased

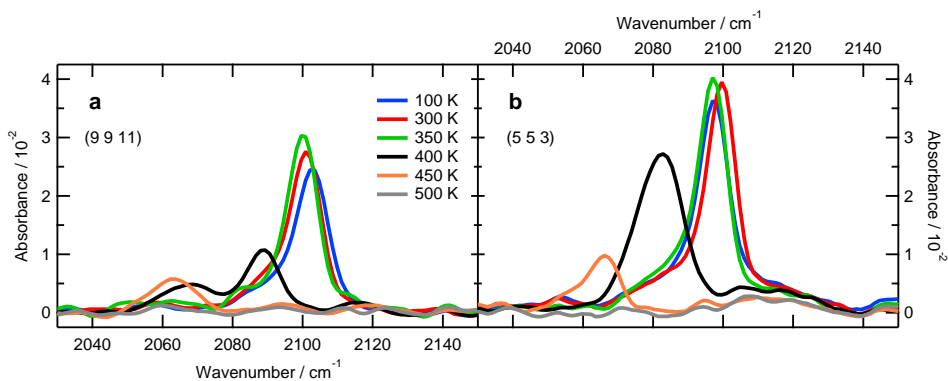


**Figure 6.4:** Absorbance spectra of on-top bound CO on a) (9 9 11) and b) (5 5 3). Spectra were measured after sequentially flashing to 300 K, 350 K, 400 K, 450 K and 500 K. Spectra were recorded at 100 K.

sequentially. A sample spectrum is measured at 100 K between every temperature. Infrared spectra are presented in three separate figures. Figure 6.3d compares absorbance spectra for on-top bound CO after flashing the sample to 300 K (red) and 400 K (black).

Figure 6.4 compares on-top spectra for Pt(9 9 11) and Pt(5 5 3) after annealing and/or desorbing (some of) the CO overlayer by flashing to increasingly higher temperatures. Initially a single band is observed from CO adsorbed to both step and terrace sites. Sequential flashing the sample to higher temperature initially induces CO desorption from terraces. As a consequence, the single band red shifts and a second band appears in case of (9 9 11). A single band is observed at low wavenumbers (2060-2070 cm<sup>-1</sup>) when only step sites are occupied after flashing the sample to 450 K. Figure 6.5 compares spectra with bridge absorbance features for Pt(1 1 1), Pt(11 11 9), and Pt(2 2 3).

### Top-bound CO

On-top terrace and step sites yield different internal vibrational frequencies, separated by 20 cm<sup>-1</sup> in references Yoshinobu et al.[128] and Xu et al.[122] At the step, positive outward dipoles split the molecular orbitals of the

adsorbed CO, resulting in a lowering of the  $2\pi^*$  orbital energy.[123, 129] This increases back donation from Pt to CO, and consequently CO bonded to the step edge has a lower frequency than on the terrace.

Band positions on all surfaces shown in figure 6.3 are located between  $2097\text{ cm}^{-1}$  and  $2104\text{ cm}^{-1}$  after annealing the CO overlayer at 300 K.  $2100\text{ cm}^{-1}$  is the accepted peak position for a saturated Pt(1 1 1) surface.[130–132] Previous studies have reported that both on-top terrace sites and on-top step sites are occupied at high CO coverage.[122, 123, 125, 132] Only single bands are observed at high coverage, however, because transition-dipole/transition-dipole coupling yields delocalized molecular excitons. The majority terrace-site resonance falls within the natural linewidth of the minority step resonance, hence the latter donate their oscillator strength to the single excitonic signal. Step density determines the number of each sub-population contributing to the exciton, and thereby modulates the band frequency and intensity. Additionally, the adsorbed layer is relatively uniform within the typical delocalization distance at the extremes of either no steps or high step density. It yields a narrow resonance. At intermediate step densities with on average 8 and 10 atom-wide terraces, step-adsorbed molecules are effectively defects in the terrace-adsorbed exciton and the resonance broadens. The integrated absorbance (hence infrared oscillator strength) is approximately conserved, but the tilt and modified electronic structure of edge-adsorbed molecules could account for systematic changes.

Flashing the sample to 400 K shows more diversity in the absorbance signals—  $2073\text{ cm}^{-1}$  to  $2093\text{ cm}^{-1}$ —as a function of step density. All vibrational bands shift toward lower frequencies, and in some cases two peaks are resolved. CO desorbs from the overlayer with increasing adsorption energy when flashing the crystal to higher temperatures: terrace bridge sites first, terrace on-top sites after, then **A-** and **B-step** sites.[122, 123, 125] As expected, integrated absorbance at Pt(1 1 1) is reduced slightly by this loss of molecules. The band center also shifts, an indication that the terrace-adsorbed layer is not present as constant-density islands, since the

magnitude of transition-dipole/transition-dipole coupling within such islands would be independent of coverage. Once again, areas of intermediate step density yield broad spectra characteristic of excitons in a non-uniform layer. At high step density and low coverage, the absorption band narrows again. This resonance must represent a molecule uniformly bound to step sites and decoupled from the depopulated terrace-site exciton. Sensitivity permitting, an unambiguous assessment of intermolecular coupling effects would require isotopomeric dilution measurements. Examples of detailed RAIRS analysis can be found in Hollins[132] and Hoffmann.[108] In agreement with the literature, there is a preferential retention of molecules at the strongly-binding **B-type** steps.

Figure 6.4a and b display the absorbance of on-top CO on (9 9 11) and (5 5 3) surfaces, following 0.75 Langmuir exposure at 100 K. Spectra were measured at 100 K, and then sequentially after flashing to 300 K, 350 K, 400 K, 450 K and 500 K. All spectra were recorded at 100 K. Experiments on (9 9 11) clearly show the gradual separation of step and terrace absorbance bands as the latter sites are depopulated. Flashing the (9 9 11) crystal surface to 300 K and 350 K has little effect on the band position, shifting it in steps of  $4\text{ cm}^{-1}$ . This small shift is due to CO desorption from the terrace, resulting in larger intermolecular distances. The integrated absorbance increases, possibly due to ordering of the terrace-bound layer.[123] After flashing to 400 K, and the presumed loss of most terrace-bound molecules, two distinct red-shifted bands appear. Only a single band at  $2063\text{ cm}^{-1}$  remains after flashing to 450 K, indicating that only step sites are populated. After flashing to 500 K the coverage falls below the detection sensitivity of our experiment.

The band position at 100 K for Pt(5 5 3) is closer to the on-top step singlet frequency than (9 9 11). There, higher step density results in stronger on-top step dipoles compared to the terrace sites. The behavior of (5 5 3) on-top spectra follows the same pattern as (9 9 11), except after flashing to 400 K. The band position shifts to the red, but no distinct on-top step

band is observed and the band width increases only slightly. This behavior may reflect the greater similarity of **B-type** steps to a (1 1 1) terrace.

### Bridge-bound CO

CO in a bridge position has a smaller infrared cross section than CO in an on-top position.[122, 123] Figure 6.5 compares absorbance spectra measured on Pt(1 1 1), **Pt(11 11 9)** and **Pt(2 2 3)** at 100 K. Figure 6.5a shows the absorbance of a (1 1 1) surface, on which 50% of CO molecules occupy bridge sites.[115, 133] The integrated absorbance of the bridge-bound population is at least four times smaller than the on-top signal. After annealing the (1 1 1) surface to 350 K, the bridge signal remains. Subsequent annealing to 400 K removes the bridge signal completely, as previously reported. Figure 6.5b shows CO adsorbed to the **(11 11 9)** surface. Here, the bridge signal appears broader than (1 1 1) due to transition-dipole/transition-dipole coupling between CO adsorbed to steps and terraces. The terraces are depleted by annealing the surface to 350 K. The bridge band narrows accordingly. After annealing to 400 K, the bridge-bound signal falls below the experimental sensitivity.

Figure 6.5c shows absorbance spectra for the **Pt(2 2 3)** surface. In spite of previous reports,[125] bridge bound CO is not detected at all on the **(2 2 3)** surface or the three other highest step density surfaces shown in figure 6.3c. First, this may be caused by CO reorganization on shorter terraces, resulting in lower bridge site density. Second, absorption coefficients on the shorter terraces may be weaker as a result of adsorbed CO molecules tilting away from the surface normal. This reduces the transition dipole strength perpendicular to the surface. Integrated absorbance is thereby lowered and increasing step density may increase the density of such tilted bridging molecules. Third, bridge signals on narrower terraces have been observed previously. Tapering of the crystal also limits the surface area available for RAIRS. We speculate that bridge bound CO for our higher step density vicinal surfaces may be too few to be observed in the current setup.

A number of steps can be taken to improve the experiment. The signal-to-noise ratio may benefit from several changes for a RAIRS setup dedicated to resolving the influence of step density using curved single crystal surfaces. First, to increase the area being investigated without increasing the range of vicinal surfaces being probed, a slit aperture can be used as a light source instead of the current pinhole. The greater surface area of the slit increases IR throughput with no loss in spatial resolution. Second, sensitivity can be improved by a more intense IR source, such as a water-cooled globar. Third, the curved crystal can be fashioned as a rectangular section rather than circular (see figure 6.1). This would limit the effect of tapering of the sample and increase the surface area available for RAIRS at high step density. Finally, experiments are currently performed using a liquid nitrogen cooled MCT detector. Depending on the bandwidth of interest, a liquid nitrogen cooled InSb detector may significantly increase the signal.

For curved single crystal surfaces, spatial resolution is essential. The spatial resolution of our RAIRS setup is limited by focus of our IR probe:  $\text{FWHM} = 0.72 \text{ mm } (\pm 0.11 \text{ nm}^{-1})$ . Higher spatial resolution can be achieved. First, the simplest improvement is to focus IR light of the globar on a smaller pinhole. Second, the shape of the focus can be improved by removing the image of the globar. This is achieved by focusing light of the globar onto an optical fiber, instead of a pinhole. The focus of the light exiting the optic fiber is better defined than it would be for a pinhole of the same size. Third, the current setup was not initially designed for RAIRS on curved samples. As a consequence, the f-number of the off-axis parabolic mirrors used for RAIRS are relatively large due to the large size of the main UHV chamber (275 mm) do not match the f-number of the collimating mirror inside the FTIR. A tighter focus and better spatial resolution can be achieved by using off-axis parabolic mirrors with a smaller f-number. A smaller main chamber or placing parabolic mirrors inside the vacuum would then be required.

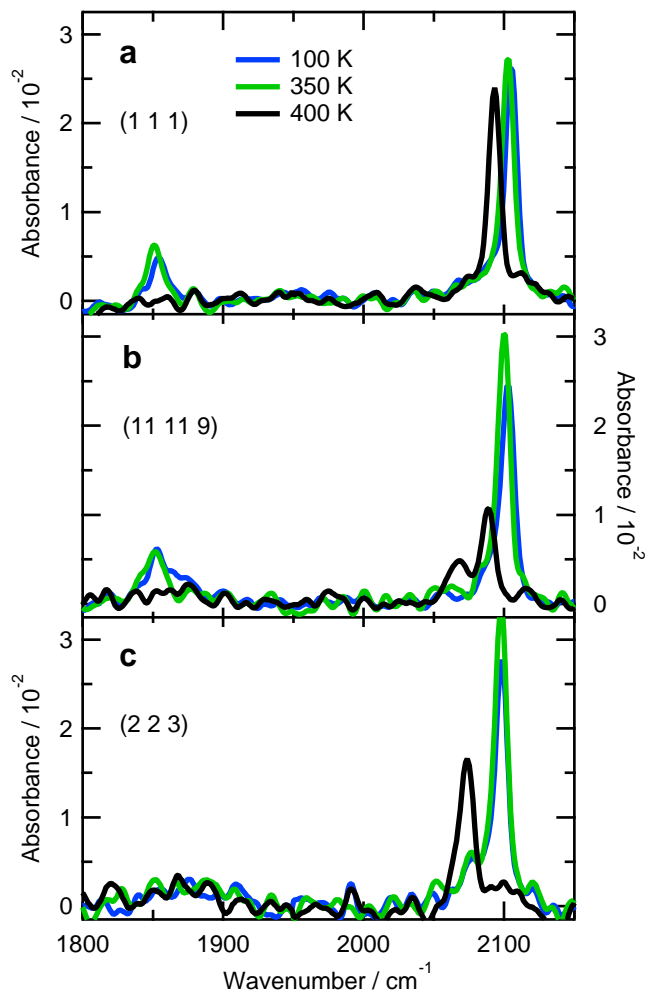


**Figure 6.5:** Absorbance spectra of CO including signals attributed to on-top and bridge bound CO to a) Pt(1 1 1), b) Pt(11 11 9) and c) Pt(2 2 3). Each surface was exposed to 0.75 L CO at 100 K. Spectra were measured directly after dosing and sequentially after flashing to 350 K and 400 K. All spectra were recorded at 100 K.



## Conclusion

Curved single crystals provide a continuous range of low and high Miller index surfaces on one single crystal. Yet the use of these curved samples for surface science can present new experimental challenges. The majority of diagnostic tools were developed for flat surfaces, where spatial resolution is relatively unimportant. The use of RAIRS is particularly hindered by the curved surface, as it also acts as a convex cylindrical mirror. By placing a coaxial collimating mirror in the UHV behind the sample, we have modified a standard UHV RAIRS setup for using curved surfaces. The collimator is aligned to minimize the expansion of the infrared beam created by the curved crystal surface. We have presented proof-of-principle experiments on a curved Pt(1 1 1) crystal containing surfaces with A- or B-type steps separated by (1 1 1) terraces. Spectra were measured for a variety of CO coverages on nine different Miller index surfaces. Four terrace widths (4, 5, 8 and 10 atoms wide), both with A- and B-type steps, were investigated in addition to the (1 1 1) surface. Both on-top and bridge bound CO were observed. Their behavior as a function of temperature was generally consistent with published work on this classic system. We have made suggestions for further improvements on the technique to improve both signal-to-noise and spatial resolution.



---

**Outlook – CO<sub>2</sub> spectroscopy and state-preparation for state-resolved dissociation experiments**

---

During this PhD work, we started a new project to study state-resolved CO<sub>2</sub> dissociation. To this end, an optical setup was developed to vibrationally excite CO<sub>2</sub> in the supersonic molecular beam. This line of research will be continued within our research group. As an outlook, we provide a basic description of CO<sub>2</sub> spectroscopy and subsequently explain how we prepare CO<sub>2</sub> in an excited state in the beam.

## CO<sub>2</sub> spectroscopy

Spectroscopic observations and interpretation thereof using quantum mechanics has been essential in much of our current understanding of molecules and their structure and energy levels. Here, we present a short introduction into the spectroscopy of CO<sub>2</sub> to provide a foundation for later work. The first half of this chapter is a summary of sections concerning linear molecules from *Molecular Spectra and Molecular Structure: II Infrared and Raman Spectra of Polyatomic Molecules* by Gerhard Herzberg.[134]

Electromagnetic radiation (photons) can be absorbed or emitted by molecules. The energies of these photons take discrete values that match energy level differences between the initial and final state. On photon absorption, molecules are electronically, vibrationally, and/or rotationally excited. The goal of the experiment is activation of CO<sub>2</sub> by absorption of mid-infrared radiation and subsequent reaction. After excitation, CO<sub>2</sub> will be impinged on a Ni(1 1 7) catalytic surface for state-resolved dissociation, but this is unfortunately beyond the scope of this thesis. Thorough understanding of the experimental results will necessitate a basic understanding of CO<sub>2</sub> spectroscopy, which we provide here. We focus on spectroscopic concepts relevant for the results in this thesis: rotations, vibrations, and combination thereof; so-called rovibrations. Excitation follows selection rules that are governed by symmetry considerations. Therefore, we first delve into the symmetry of linear molecules. Rotations, vibrations, rovibrations are subsequently described. Finally, deviations from these model descriptions are also discussed.

## Symmetry

The symmetry of molecules is described by group theory. In group theory, two point groups describe the possible types of linear molecules: D<sub>∞h</sub> and C<sub>∞v</sub>. Molecules with a center of inversion belong to the first, e.g. C<sup>16</sup>O<sub>2</sub>, whereas molecules without a center of inversion belong to the second, e.g. OCS or C<sup>16</sup>O<sup>18</sup>O. In other words, molecules described by D<sub>∞h</sub> have no permanent dipole moment, while those with C<sub>∞v</sub> do. The spectroscopy for

these two types of linear molecules is different. Symmetry governs whether transitions are infrared and/or Raman active and which rotational states are allowed. From now on, CO<sub>2</sub> refers to the most common isotope, C<sup>16</sup>O<sub>2</sub>, unless specified otherwise.

Character tables are used to describe how symmetry species of a point group change upon symmetry operations. Different characteristics of molecules may be of the same symmetry species. The character table for CO<sub>2</sub>, D<sub>∞h</sub>, is shown in table 7.1. Here, the z-axis is defined as the intermolecular axis. Ground state CO<sub>2</sub> has  $\Sigma_g^+$  character, i.e. it is symmetric (+1) to all symmetry operations.

CO<sub>2</sub> has 3N=9 degrees of freedom: 3 translations, 2 rotations, and 4 vibrations. T<sub>x</sub>, T<sub>y</sub>, and T<sub>z</sub> are translations in the x, y, and z directions. R<sub>x</sub>, R<sub>y</sub>, and R<sub>z</sub> are rotations around the x, y, and z axes respectively. Translation, rotation or vibrational excitation may alter the molecular symmetry so that it is anti-symmetric (-1) to some symmetry operations.  $\nu_1$ ,  $\nu_2$ , and  $\nu_3$  are the three normal modes with  $\Sigma_g^+$ ,  $\Pi_u$ , and  $\Sigma_u^+$  character. The  $2\nu_2$  overtone is added to the character table due to the Fermi resonance discussed below.

Table 7.1:  $D_{\infty h}$  character table

$D_{\infty h}$	I	$2C_{\infty}^{\phi}$	$2C_{\infty}^{2\phi}$	...	$\sigma_h$	$\infty C_2$	$\infty \sigma_v$	$2S_{\infty}^{\phi}$	$2S_{\infty}^{2\phi}$	...	$S_2 \equiv i$	
$\Sigma_g^+$	+1	+1	+1	...	+1	+1	+1	+1	+1	...	+1	$\nu_1, 2\nu_2 \ell = 0$
$\Sigma_u^+$	+1	+1	+1	...	-1	-1	+1	-1	-1	...	-1	$T_z, \nu_3$
$\Sigma_g^-$	+1	+1	+1	...	+1	-1	-1	+1	+1	...	+1	$R_z$
$\Sigma_u^-$	+1	+1	+1	...	-1	+1	-1	-1	-1	...	-1	
$\Pi_g$	+2	$2\cos\phi$	$2\cos 2\phi$	...	-2	0	0	$-2\cos\phi$	$-2\cos 2\phi$	...	+2	$R_x, R_y$
$\Pi_u$	+2	$2\cos\phi$	$2\cos 2\phi$	...	+2	0	0	$+2\cos\phi$	$+2\cos 2\phi$	...	-2	$T_x, T_y, \nu_2$
$\Delta_g$	+2	$2\cos 2\phi$	$2\cos 4\phi$	...	+2	0	0	$+2\cos 2\phi$	$+2\cos 4\phi$	...	+2	$2\nu_2 \ell = 2$
$\Delta_u$	+2	$2\cos 2\phi$	$2\cos 4\phi$	...	-2	0	0	$-2\cos 2\phi$	$-2\cos 4\phi$	...	-2	
$\Phi_g$	+2	$2\cos 3\phi$	$2\cos 6\phi$	...	-2	0	0	$-2\cos 3\phi$	$-2\cos 4\phi$	...	+2	
$\Phi_u$	+2	$2\cos 3\phi$	$2\cos 6\phi$	...	+2	0	0	$+2\cos 3\phi$	$+2\cos 4\phi$	...	-2	
...	...	...	...	...	...	...	...	...	...	...	...	

## Rotations

Rotation of linear molecules in the electronic ground state is well-described by the rigid rotor model. In this model, bond angles and lengths are fixed. Rotational energy levels are approximated using:

$$E_{\text{rot}} = B \cdot J(J + 1) \quad (7.1)$$

where B and J are the rotational constant and total angular momentum quantum number (or rotational quantum number).

We exclude a minor correction to account for centrifugal distortions with increasing rotational states. We require quantum mechanics to describe the allowed total angular momentum. The total eigenfunction of a molecule is the product of the electronic, vibrational, and rotational wavefunctions:

$$\Psi = \Psi_{\text{nucl}} \Psi_{\text{elec}} \Psi_{\text{vib}} \Psi_{\text{rot}} \quad (7.2)$$

The wavefunctions for the rigid rotor,  $\Psi_{\text{rot}}$  can be approximated by spherical harmonics[135] (also called the particle on a sphere), which closely resemble electronic wavefunctions of <sup>1</sup>H. For any molecule, the total angular momentum is comprised of the vibrational angular momentum quantum number  $\ell$ , magnetic quantum number M, and spin quantum number  $M_s$  (if  $M_s = \frac{1}{2}$ ). CO<sub>2</sub> does not have nuclei with nuclear spin, thereby excluding any hyperfine splitting by  $M_s$ . J then only has a 2J+1 degeneracy where M can be -J, -J+1 ... J-1, J. The degenerate wavefunctions for J = 0 to J = 3 are shown in figure 7.1.

Rotations have  $\Pi_g$  character. Note center of inversion operation i for  $\Pi_g$ ; the sign of the wavefunction cannot change upon inversion. Examination of the rotational wavefunctions in figure 7.1 shows that the even rotational states, J = 0 and J = 2, are symmetric to the inversion operation. In contrast, all odd rotational states are antisymmetric to inversion. As a consequence, all odd rotational states are missing in the vibrational ground state for molecules with point group D<sub>∞h</sub>. Odd rotational levels do exist

for excited states containing odd quanta of asymmetric stretch or quanta of bend vibration.

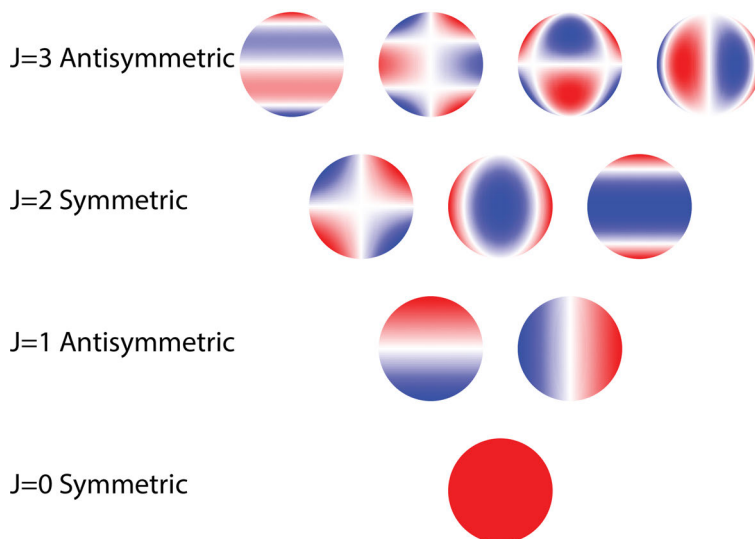


**Figure 7.1:** Spherical harmonics for  $J = 0$  to  $3$  with degeneracies  $M = 0$  to  $+J$  shown from left to right. Even (odd)  $J$  states are (anti)symmetric to the inversion operation.

Generally, pure rotational Raman transitions occur if there is a change in polarizability, while pure rotational infrared transitions are only observed if the molecule has a permanent dipole moment. Pure rotational transitions have the following general selection rules:

$$\begin{aligned}\Delta J_{\text{infrared}} &= \pm 1 \\ \Delta J_{\text{Raman}} &= \pm 2\end{aligned}\tag{7.3}$$

where  $J$  has an integer number of  $h/2\pi$ . As such, molecules of the  $D_{\infty h}$  point group only show a pure rotational Raman spectrum. The previously discussed symmetry considerations prohibit odd rotational states in the vibrational ground state. As for  $H_2$  and  $D_2$ , conversion of the symmetric (even) to antisymmetric (odd) rotational levels (or vice versa) is forbidden. A pure infrared rotational spectrum is only observed for  $CO_2$  isotopologues with a permanent dipole, i.e.  $CO_2$  molecules with the  $C_{\infty v}$  point group.



The energy level of rotational states can be approximated with:

$$E_{\text{rot}} = \frac{hJ(J+1)}{8\pi^2 c \Sigma m_i r_i^2} \quad (7.4)$$

where  $h$ ,  $c$ ,  $m_i$ , and  $r_i$  are Planck's constant, the speed of light, the mass, and distance from the center of mass of particle  $i$ . The resulting rotational energy is quantized and increases quadratically with  $J$ . The energy difference between two levels, which is observed in absorption experiments, can be calculated by:

$$\begin{aligned} \Delta E &= \Delta E_{\text{final}} - \Delta E_{\text{initial}} \\ \Delta E &\propto (J + \Delta J) \cdot (J + \Delta J + 1) - J \cdot (J + 1) \end{aligned} \quad (7.5)$$

Pure rotational Raman transitions yield S-branches ( $\Delta J = 2$ ) and O-branches ( $\Delta J = -2$ ), which yield equidistant lines with  $8B$  difference. For pure rotational infrared transitions, the energy difference is  $2(J+1)$  for R-branches ( $\Delta J = +1$ ) or  $-2J$  for P-branches ( $\Delta J = -1$ ). The resulting rotational spectrum yields equidistant lines with  $4B$  increments. While pure rotational infrared transitions are symmetry forbidden for CO<sub>2</sub>, rotational excitation is allowed in combination with vibrational excitation. Equidistant rotational lines are observed for rotation vibration (rovibration) excitation. Before we go into rovibrations, we shall first introduce pure vibrations (also called normal modes or fundamentals).

## Vibrations

Molecular vibrations are described reasonably well by the harmonic oscillator model: atoms within the molecule are masses attached to one another through springs. Bonded atoms are held together by strong springs. Unbonded atoms are connected through weaker springs to relax the molecule back to the overall molecular shape. Under the assumption that the amplitude of the vibration is infinitesimal, the energy level of the harmonic oscillator is described by:

$$E_{\text{vib}} = h\nu_i \left( v_i + \frac{1}{2} \right) \quad (7.6)$$

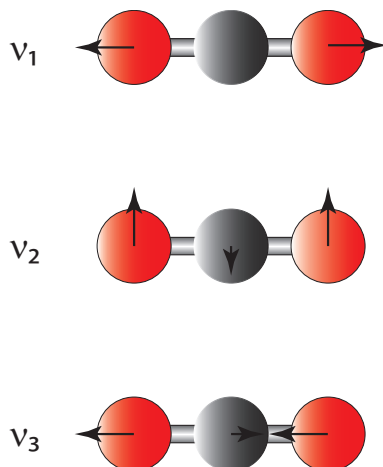


**Figure 7.2:** The  $\nu_1$  symmetric stretch, degenerate  $\nu_2$  bend, and  $\nu_3$  asymmetric stretch vibrations.

where  $\nu_i$  and  $v_i$  are the frequency and vibrational quantum number of normal mode (or fundamental vibration)  $i$ . The energy level of the harmonic oscillator increases linearly with  $v_i$ .

CO<sub>2</sub> has 4 vibrational degrees of freedom:  $\nu_1$ , double degenerate  $\nu_2$ , and  $\nu_3$ . These three normal modes are shown in figure 7.2. Ground state CO<sub>2</sub> has  $\Sigma_g^+$  character. The symmetry of the molecule may change upon excitation of one or more quanta of vibration, in which case the transition is infrared active.

$\nu_1$  is the symmetric stretch vibration with  $\Sigma_g^+$  character. In this fundamental, the oxygen atoms move in phase towards and away from the carbon atom in the center of mass. There is no change in symmetry and therefore no change in dipole moment. This mode is only Raman active. The transition occurs at approximately  $1388\text{ cm}^{-1}$ .

$\nu_2$  is the double degenerate bend vibration with  $\Pi_u$  character. In this mode, vibrationally excited CO<sub>2</sub> bends so that the OCO bond angle is not  $180^\circ$  anymore. The oxygen atoms move orthogonal to the intermolecular

axis, while the carbon atom moves in the opposite direction to conserve the center of mass. Excitation of the bend vibration results in a superposition of the two degenerate modes and generates vibrational angular momentum ( $\Delta\ell = \pm 1$ ). This degeneracy and angular momentum gives rise to rotation around the bond axis on excitation of the bend vibration. There is a change in symmetry and dipole moment on excitation of the bend vibration. Consequently, this mode is infrared active. The transition occurs at approximately  $667\text{ cm}^{-1}$ .

$\nu_3$  is the asymmetric stretch vibration with  $\Sigma_u^+$  character. The oxygen atoms move out of phase along the bond axis. Here, the carbon atom moves along the intermolecular axis to preserve the center of mass. The change in dipole moment means that this mode is infrared active. The transition occurs at approximately  $2350\text{ cm}^{-1}$ .

### Rovibrational transitions

The selection rules for exciting a vibration in a CO<sub>2</sub> molecule depend on the symmetry and vibrational angular momentum  $\ell$  of the initial and final state. The selection rules are also consequential for the spacing between the rotational lines; they determine whether odd rotational levels exist or not. The following selection rules apply for D<sub>∞h</sub> molecules:

1.  $\Delta\ell = 0$ ,  $\Delta J = \pm 1$  (i.e.  $\Sigma - \Sigma$  transitions)
2.  $\Delta\ell = \pm 1$ ,  $\Delta J = 0$  or  $\pm 1$  (e.g.  $\Pi - \Sigma$ ,  $\Delta - \Pi$  transitions)
3.  $\Delta\ell = 0$  and  $\ell \neq 0$ ,  $\Delta J = 0$  or  $\pm 1$  (e.g.  $\Pi - \Pi$  transitions)

The first selection rule is exemplified by the  $\nu_3$  rovibrational transition in CO<sub>2</sub>; i.e. the transition of interest for this work. Excitation of this rovibration results in a P-, and R-branch, but no Q-branch ( $\Delta J = 0$ ). As  $\ell$  remains 0 and  $\Delta J = \pm 1$ , excitation of the  $\nu_3$  vibration changes the vibrational and rotational quantum numbers  $v$  and  $J$  by 1. The rotational lines show a 4B separation.

The second selection rule constitutes a change in  $\ell$ , which occurs for the  $\nu_2$  bend vibration in  $\text{CO}_2$ . Here,  $\Delta J$  may be 0 or  $\pm 1$ . Consequently, excitation of the  $\nu_2$  rovibration exhibits a P-, Q-, and R-branch. Quantum numbers  $v$  and  $\ell$  are changed with 1, while  $J$  may remain the same or change by 1. These rotational lines also show a 4B separation.

$\ell$  does not change for the final selection rule, but the initial state is already vibrationally excited (hot band transitions) with vibrational angular momentum. This is the case for  $\text{CO}_2$  on excitation of the  $\nu_3$  vibration with one or more quanta of  $\nu_2$  in the initial state. Excitation may occur from both odd and even initial rotational states, due to P-, Q-, and R-branches being available for bend vibrations. The rotational line spacing for these rovibrational transition is therefore 2B.

### Anharmonicity of rovibrations

We started off on the premise that normal modes have different symmetry and that these vibrations can be described by the harmonic oscillator model. The harmonic oscillator model assumes that vibrations can be disentangled into normal vibrations. However, the harmonic oscillator model fails when mixing and coupling occurs between the different normal modes under certain conditions. The three main sources for deviations from the harmonic oscillator model for linear molecules are:  $\ell$ -type doubling, Fermi resonance, and Coriolis coupling.

$\ell$ -type doubling occurs for overtones of the bend vibration of  $\text{CO}_2$ . As mentioned previously,  $\nu_2$  excitation changes the vibrational angular momentum  $\ell$ .  $\ell$  has two possible directions when  $\Delta\ell = \pm 1$ .  $1\nu_2$  has  $\ell = +1$  or  $\ell = -1$ , which are identical in energy. However, overtones of the  $\nu_2$  are degenerate and cause  $\ell$ -type doubling; e.g. for  $2\nu_2$  the vibrational levels split for  $\ell = 0$  and  $\ell = \pm 2$ .

An additional anharmonicity occurs for overtones of the bend vibration with  $\ell = 0$ .  $2\nu_2$  with  $\ell = 0$  has the same symmetry ( $\Sigma_g^+$ ) and very similar energy as the  $\nu_1$  symmetric stretch vibration. Consequently, the  $2\nu_2$  overtone

with  $\ell = 0$  and  $\nu_1$  fundamental are in Fermi resonance. These vibrational states mix and are indistinguishable. In addition, the energy levels that are in Fermi resonance are perturbed; i.e. the separation between the energy levels is much larger than expected. Two peaks are observed in Raman for the  $\nu_1$  vibration due to the Fermi resonance with  $2\nu_2$ . While we would expect  $2\nu_2$  to be roughly twice the  $\nu_2$  normal mode, both Raman peaks are separated significantly from the expected  $2\cdot 667\text{ cm}^{-1}$  for the  $2\nu_2$  vibration due to the perturbation.

The previous anharmonicities deal with the symmetric stretch and bend vibrations. The Coriolis effect affects the asymmetric stretch and bend vibrations. During a pure normal mode vibration without rotation, the atoms move linearly as shown in figure 7.2. Vibrational and rotational motion induces vibrational anharmonicity due to the Coriolis effect. This concept is visualized in figure 7.3. Consider the normal vibrations shown in figure 7.3a. The linear motion of the atoms relative to the center of mass during vibration is indicated in black. Counter-clockwise rotation of the molecule is shown with blue arrows. The linear motion due to vibration in the rotating frame gives rise to a fictitious Coriolis force perpendicular and proportional to the velocity of the vibration. These Coriolis forces are shown in figure 7.3a as green arrows. The Coriolis force direction for the various normal modes shows that some normal modes couple to one another in the rotating frame. This is shown in figure 7.3b with white arrows tracing the motion of the atoms. The  $\nu_1$  vibration itself does not exhibit Coriolis coupling to other normal modes; it couples to rotation. However, the  $\nu_2$  and  $\nu_3$  vibrations do couple to one another and mixing of the two occurs. The  $\nu_2$  bend vibration of rotating CO<sub>2</sub> also exhibits some  $\nu_3$  asymmetric stretch vibration with the frequency of  $\nu_2$ . Similarly,  $\nu_3$  induces a  $\nu_2$  bend vibration with the frequency of the  $\nu_3$  vibration.

### **State preparation of CO<sub>2</sub> in the supersonic molecular beam**

Now that we have immersed ourselves in the spectroscopy of CO<sub>2</sub>, we focus on experimentally preparing a CO<sub>2</sub> supersonic molecular beam in a specific

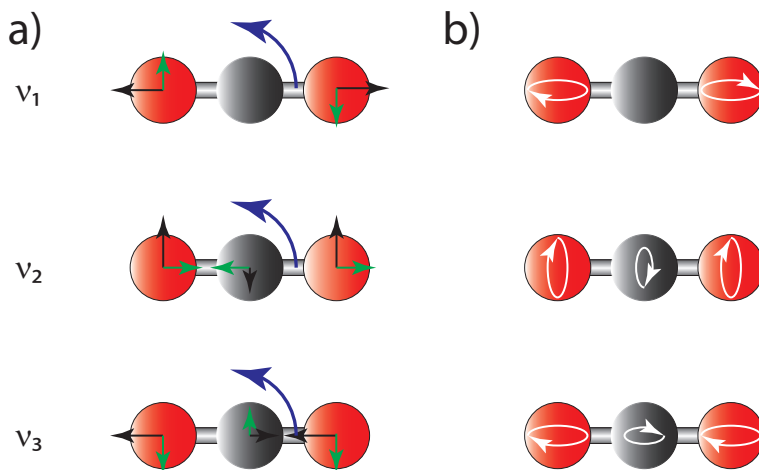


**Figure 7.3:** The Coriolis effect for the  $\nu_1$  symmetric stretch,  $\nu_2$  bend, and  $\nu_3$  asymmetric stretch vibrations. a) Molecular rotation, motion of the atoms, and the Coriolis force is indicated with blue, black, and green arrows respectively. b) Motion of the atoms in the rotating frame is shown with the white arrows in the right set of figures.

rovibrational state. The UHV apparatus is described in detail in chapter 2. For excitation, infrared (IR) radiation from a continuous wave (CW) light source is crossed with the CW supersonic molecular beam. The excitation scheme is based on that developed by Bruce Yoder[136] from the group of Rainer Beck. Excitation of  $\text{CO}_2$  occurs if IR radiation is resonant with the optical transition: the  $\nu_3$  asymmetric stretch vibration at approximately  $2350 \text{ cm}^{-1}$ .

The optical setup is shown in figure 7.4. The setup is built up on a laser table and enclosed in an aluminum box that is purged with dry nitrogen. Approximately 300 mW of tunable IR radiation is generated by a commercial Optical Parametric Oscillator(OPO, Lockheed Martin Aculight, Argos Model 2400, SF-15, Module D). Of the 300 mW, 50% is sent to the UHV chamber for state-preparation. The other 50% is used for characterization and stabilization. A  $\text{CaF}_2$  window samples a small amount (5%) for the wavemeter ( $\lambda$ ). The remainder is retroreflected through a  $\text{CO}_2$  gas cell for Lamb dip spectroscopy for actively stabilizing the OPO.

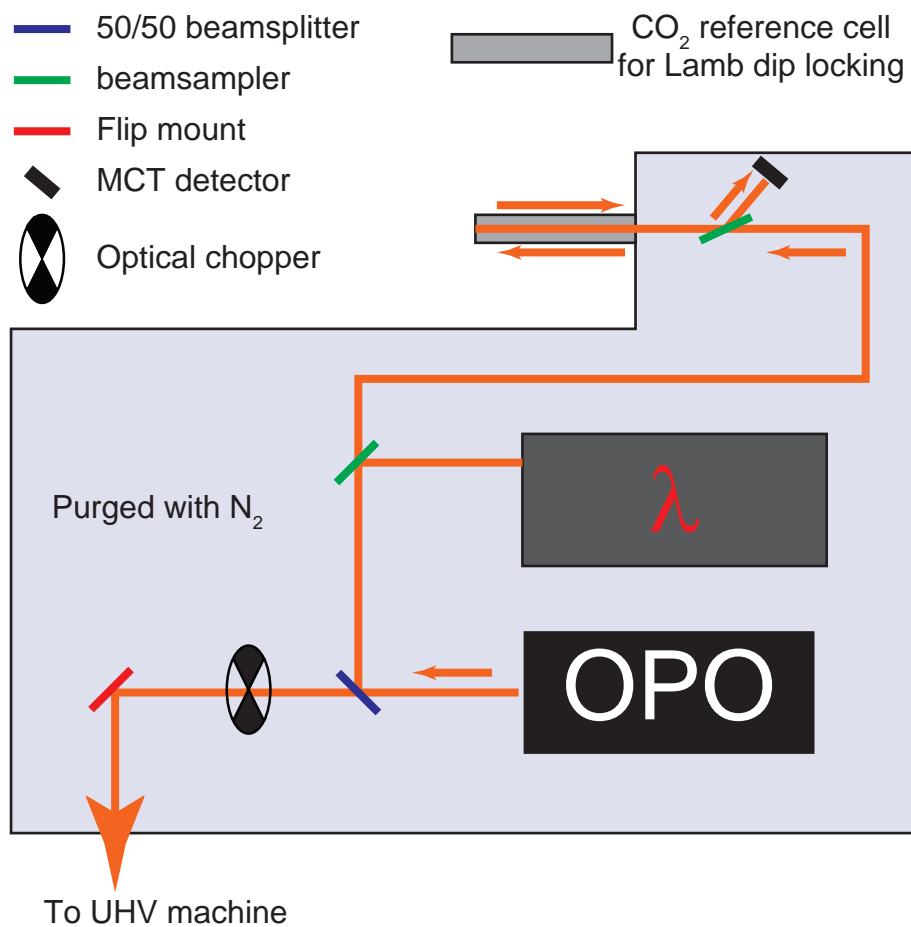


**Figure 7.4:** Optical setup used to characterize and actively stabilize the OPO.

We prepare CO<sub>2</sub> in a specific rovibrational state using single mode CW tunable infrared radiation. The light source of choice is a commercial Optical Parametric Oscillator. An OPO converts high energy photons into two lower energy photons. Total energy is conserved:

$$E_{\text{pump}} = E_{\text{signal}} + E_{\text{idler}} \quad (7.7)$$

For historical reasons, the two low energy photons produced are called signal and idler, of which the latter is lowest in energy. Four different available OPO modules offer the Argos system a broad spectral range from 2.3 – 4.6  $\mu\text{m}$  (4348 – 2147  $\text{cm}^{-1}$ ). Our D module gives access to: 3.9 – 4.6  $\mu\text{m}$ . (2564 – 2147  $\text{cm}^{-1}$ )

The OPO module is pumped by a 15 W amplified (IPG Photonics) 1064 nm Yb-doped seed laser (NKT-photonics) that is part of the Argos system. The OPO module consists of two parts: a periodically-poled lithium niobate (PPLN) nonlinear crystal placed within a bowtie etalon as optical resonator. Periodic poling of the nonlinear crystal determines the  $E_{\text{signal}}:E_{\text{idler}}$  ratio. Upon exceeding a threshold power, idler and signal photons are generated. The signal beam is resonant within the etalon and builds up power within the resonator cavity. The photon conversion process is thereby amplified, increasing the idler output power.

The  $\nu_3$  R(0) transition for CO<sub>2</sub> occurs at an idler wavelength of approximately 4255 nm. From equation 7.7 and a 1064 nm pump wavelength, we calculate a signal wavelength of 1419 nm. The resulting signal and idler wavelengths present the first problem. The two most abundant infrared absorbers in air – H<sub>2</sub>O and CO<sub>2</sub> – absorb signal and idler power respectively. Idler absorption lowers the available power for CO<sub>2</sub> excitation and OPO stabilization. Signal absorption by H<sub>2</sub>O presents a bigger challenge: the signal power within the cavity can drop below the power threshold and stop the OPO from oscillating altogether. Consequently, the OPO becomes unstable when the signal is absorbed by water. Absorption by these air constituents requires purging the entire optical setup with dry nitrogen.



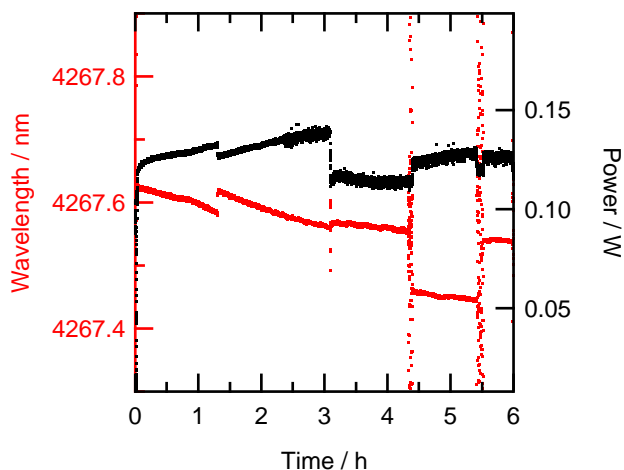


**Figure 7.5:** Idler wavelength (red, left axis) and power (black, right axis) as a function of time, exemplifying drift of the OPO.

The second problem to overcome is common for state-selective molecular beam experiments using a tunable light source. The linewidth of the light source and the natural linewidth of CO<sub>2</sub> in the supersonic molecular beam are extremely narrow. State-resolved experiments require reliable CO<sub>2</sub> excitation, i.e. the wavelength of the OPO preferably matches the transition for hours. Figure 7.5 shows the idler wavelength and power as a function of time, as measured using the wavemeter (Bristol, 621B-IR) and calibrated power meter (Thorlabs, PM100D). Three notable features are observed. First, the idler wavelength drifts substantially over time. Second, discrete jumps are observed, showing mode hops. Third, the wavemeter reading goes off scale at approximately 4 hours due to a drop in power. The overall wavelength drift of the OPO shows that active stabilization is required for long term experiments. Mode hops generally disappear or lower in frequency as the OPO stabilizes. Active stabilization cannot completely prevent these.

The idler wavelength can be tuned in three ways. Rough tuning uses the varying periodic poling across the crystal. By vertically translating the

PPLN crystal, the periodic poling experienced by the pump laser changes. Alternatively, the crystal temperature can be changed to the same effect. However, temperature is not recommended for active tuning. Intermediate tuning alters the signal wavelength resonant in the cavity by changing the etalon angle. The idler wavelength changes accordingly. Fine tuning alters the 1064 nm pump wavelength. The pump, idler and signal wavelengths are blue-shifted by straining the seed laser optical fiber with piezo tuning (0 — 200 V).

Figure 7.6 shows calculated spectral line intensities from HITRAN[137] for exciting the  $\nu_3$  vibration at gas temperatures of 298 K and 5 K. For room temperature  $\text{CO}_2$ , the P- and R-branches are observed. The Q-branch is absent, as explained by the selection rules. In addition to the  $\nu_3$  fundamental, a weaker  $v = 1 (\nu_2) \rightarrow v = 2 (\nu_2 + \nu_3)$  hot band transition overlaps with the fundamental. It is blue shifted to higher wavenumbers compared to the fundamental. However, molecules prepared in the supersonic molecular beam are rotationally and translationally cold. The rotational state distribution in the molecular beam is illustrated by the calculated line intensities at 5 K shown in the top zoomed in panel. Rotationally cold  $\text{CO}_2$  mostly resides in  $J = 0, 2$ , and 4. The bottom panel shows idler power as a function of wavenumber measured on two separate days by slowly ( $1.2 \text{ Vmin}^{-1}$ ) scanning the seed laser piezo. The power is measured after passing the idler through a 1.5 m long gas cell.

We point out two notable things. First, the spacing between the hot band transitions is approximately half that of the fundamental. For the hot band transition, the lower level has one quantum of  $\nu_2$  with symmetry. Second, there is a small offset ( $\sim 0.02 \text{ cm}^{-1}$ ) between the HITRAN database and our measured absorption peaks. This offset likely results from a slight misalignment of the idler beam entering the wavemeter. However, the offset is not relevant for our experiments as the wavemeter is only used to find the optical transition. Active stabilization is necessary for stability, since the wavemeter does not have the required accuracy.

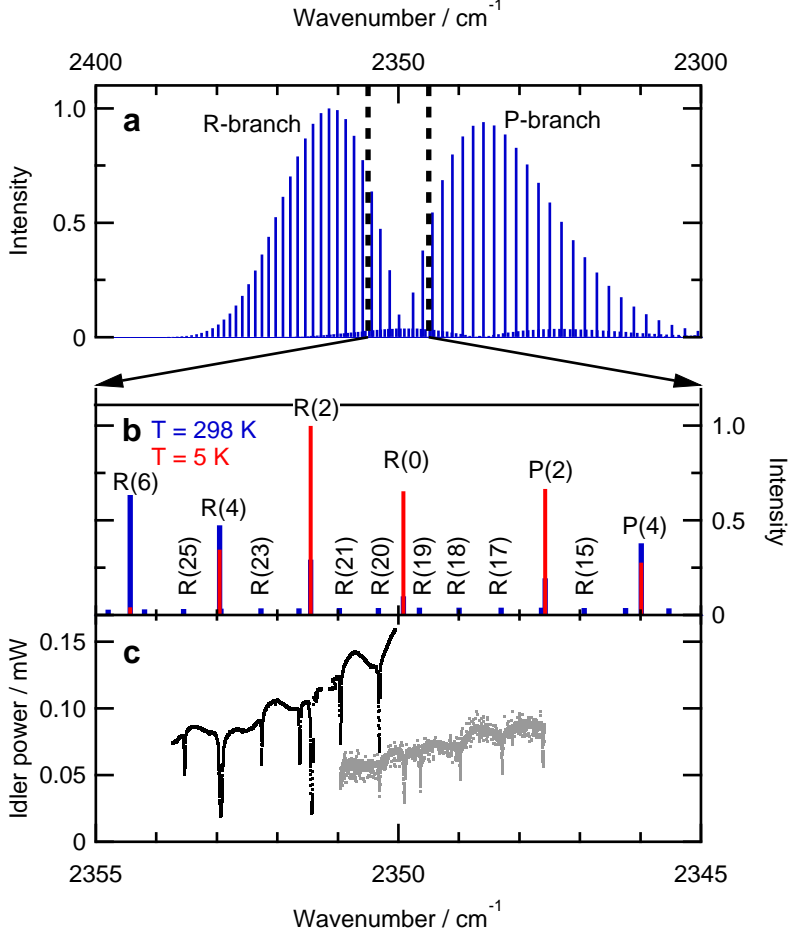


**Figure 7.6:** Transition line intensities for CO<sub>2</sub> at 298 K (blue) and 5 K (red) extracted from HITRAN.[137] The bottom panel shows two scans of the idler power measured on separate days. The power is measured after passing through a 1.5 m long gas cell containing 100 mbar (black) or 50 mbar (gray) of air.

In practice, setting the OPO to a specific wavelength is an iterative process of the following steps. The wavelength is set slightly red-shifted of the transition of interest using rough crystal tuning. Subsequently, the etalon angle is changed to maximize the idler output power. When a suitable amount of idler power is measured near the optical transition, the idler is tuned to the actual transition using piezo tuning.

To account for drift, we stabilize the OPO by locking onto the Lamb dip of the rovibrational transition.[136] We first explain the nature of the Lamb dip. Earlier in this chapter, we showed that absorption of radiation is quantized; i.e. a photon may be absorbed if the photon energy matches the energy difference between the initial and final state. In practice, absorption peaks in spectroscopy are broadened through various mechanisms, one of which is Doppler broadening. Doppler broadening occurs if absorbing molecules contain a velocity component along the propagation axis of the incident radiation. Those molecules then observe radiation with a frequency  $\nu$  instead of  $\nu_0$ :

$$\nu = \frac{c \pm v_i}{c} \nu_0 \quad (7.8)$$

where  $c$  and  $v_i$  are the speed of light and the velocity of absorbing particle i.

Figure 7.7 illustrates the concept of the Lamb dip. Panel a shows a Doppler broadened absorption profile. As high power monochromatic radiation pumps an optical transition slightly off resonance, a significant fraction of molecules with velocity  $v_i$  is excited. Panel b shows that the ground state population with  $+v_i$  is reduced compared to panel a. The hole burnt in the population distribution for  $-v_i$  is called a Bennett hole [138, 139], named after William Ralph Bennett Jr. The Bennett hole can be observed in absorption by crossing a probe beam of monochromatic radiation with the pump. A second Bennett hole is burnt in the population distribution when retroreflecting the pump beam through the gas cell in panel c. Finally, as the pump beam is tuned on-resonance with the transition in panel d, the forward and reflected beam probe the same subset of molecules: molecules

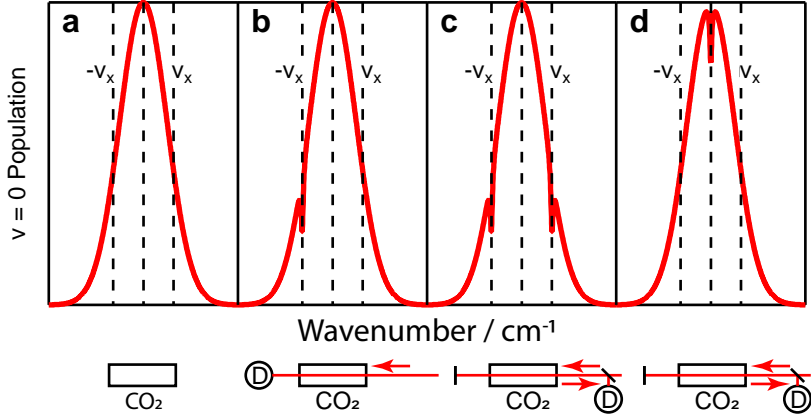


**Figure 7.7:** Illustration of Bennett holes and the resulting Lamb dip upon retroreflecting off and on resonance monochromatic radiation.

with  $v_i = 0 \text{ ms}^{-1}$ . As the forward beam saturates the transition, fewer ground state molecules are available with  $v_i = 0 \text{ ms}^{-1}$  for the retroreflecting probe beam. Consequently, a dip is observed in the absorbance spectrum. This Lamb dip[140] is named after Nobel laureate Willis Eugene Lamb Jr.

We use the Lamb dip to stabilize the OPO onto the optical transition, similar to Yoder et al.[136] Doppler broadened absorption peaks with and without Lamb dip are compared with a measured Lamb dip in figure 7.8. We measure the derivative of the absorption features using phase sensitive detection. The width of the Doppler broadened signal and its weak derivative signal near the transition limits its use for stabilization. However, the narrow Lamb dip feature and its strong derivative signal near the optical transition is ideal for active stabilization. The derivative provides the feedback with a sharp feature to lock onto.

We measure the reflected beam with a room temperature DC-coupled MCT detector (PDAVJ8, Thorlabs). Like Yoder et al., we use the Lase-lock (TEM-Messtechnik) for active stabilization. It combines all electronics required: a signal generator, the Lock-in amplifier, and a PID controller.

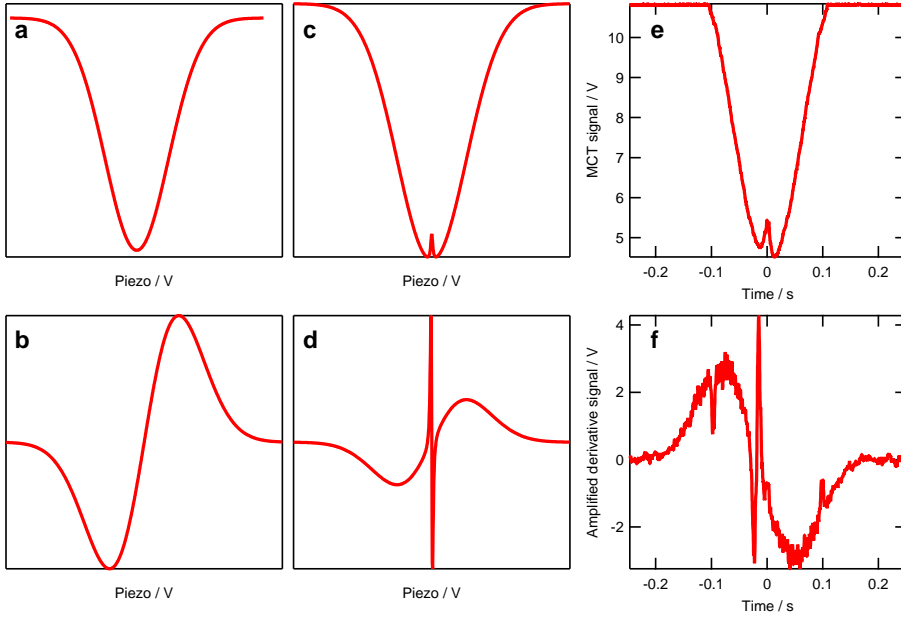


**Figure 7.8:** a) Simulated Doppler broadened absorption peak with b) its derivative signal. c) Simulated Doppler broadened absorption peak with a Lamb dip and d) its derivative signal. e) Measured Doppler broadened absorption peak with a Lamb dip and f) its derivative signal.

The signal generator applies a 4.8 mV (0.02%), 4 kHz dither to the seed laser piezo, resulting in a 0.17 pm (2.8 MHz) wavelength dither. The 4 kHz signal is sent to the lock-in amplifier as its reference input. The signal generator can superimpose a linearly sweep onto the dither to scan over an absorption line. In this way, the spectrum and its derivative in figure 7.8e and f are measured. The offset of the scan is set such that the absorption peak is centered. After observing a suitable Lamb dip, the scan generator is switched off and the PID regulator is switched on. The Laselock regulates the piezo so that the derivative of the Lamb dip is 0 V. Figure 7.9 illustrates the wavemeter reading while the idler is actively stabilized to the Lamb dip in this manner. In contrast to the instability and drift observed in figure 7.5, the wavelength is stable for over 30 hours, after which a mode hop breaks the stabilization. During stabilization, there is some drift in the measured wavelength. We attribute this to pressure and/or temperature

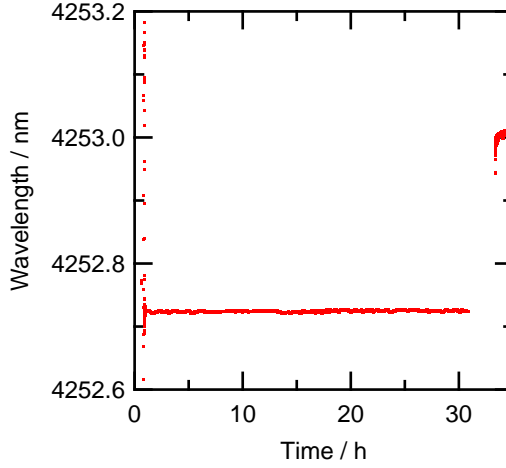


**Figure 7.9:** Idler stability during active stabilization of the R(4) transition.

fluctuations in the purge box influencing the wavemeter.

With the OPO stabilized to the vibrational transition, we may cross the idler with the supersonic molecular beam containing CO<sub>2</sub>. The idler beam sent to the main chamber is periscoped up to the supersonic molecular beam. Two protected silver mirrors aid in steering the idler through the molecular beam at 90°. Normally, the transition is saturated if 50% of molecules are pumped to an excited state. However, by using Rapid Adiabatic Passage (RAP), population inversion can be achieved.[141] In RAP, defocusing of monochromatic radiation causes absorbing molecules to experience a frequency sweep due to curved wavefronts. To this end, we use a CaF<sub>2</sub> cylindrical lens ( $f = 200$  mm, Thorlabs) to defocus the idler.[136, 141]

Finally, we require a method of detecting excited CO<sub>2</sub> molecules in the molecular beam. We use pyroelectric detection (PED) (406M39, Eltec Instruments), similar to that used by the groups of Art Utz and Rainer Beck.[136, 142] The PED works through the pyroelectric effect. A change in temperature polarizes the detector material, inducing a voltage over the detector element. As the temperature reaches steady state, the voltage

across the detector element is negated by current leaking from one side to another. Consequently, these detectors are AC-coupled and require a modulated signal.

First, we align the PED to the supersonic molecular beam. We use a diode laser to align the single crystal surface to the molecular beam. By retracting the molecular beam nozzle, the diode laser follows the same path through the skimmers as the molecular beam. The single crystal surface is aligned to the molecular beam by reflecting the diode laser back onto the sliding valve orifice. Here, we use this diode laser to align the PED as well, as the absolute signal from the diode laser is much larger than that of the molecular beam.

Figure 7.10 shows an overview of the UHV machine (Lionfish) in the top panel. It shows the modulated diode laser passing through the various skimmers before striking the PED. The PED is on a swivel so that it can rotate in and out of the molecular beam. The color of the PED traces shown in this and following figures in this chapter use modulation from the matching colored annotation. The bottom panel shows the raw PED data in red. We chop the laser with 11 Hz using the optical chopper (MC2000, Thorlabs). The optical chopper has a built in photodiode as reference output, shown in black. Note that there is a phase difference between the PED results and the reference output because the diode laser does not pass the chopper blade at the photodiode. The resulting PED signal is a 11 Hz triangular wave with an amplitude of approximately 68 mV. Modulated signals can be extracted with high signal-to-noise ratio with lock-in amplification. Using the lock-in amplifier, we extract the amplitude of the PED signal.

During beam experiments, we can modulate the molecular beam using the first beam flag, second beam flag, or the mechanical chopper. The mechanical chopper has two different slot sizes. This restricts its application for lock-in amplification, because the lock-in amplifier cannot extract the reference frequency. Meanwhile, the two beam flags can only modulate the



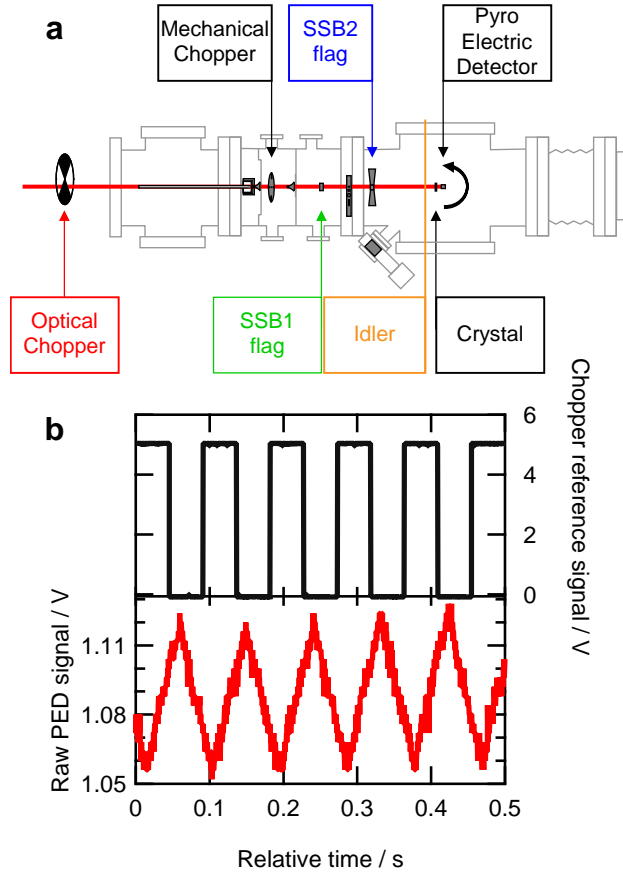


**Figure 7.10:** a) Schematic overview of the UHV machine, indicating the position of: the pyroelectric detector (PED), crystal, two beam flags, mechanical chopper, optical chopper, idler beam crossing the CO<sub>2</sub> beam during excitation. b) The PED transient is measured by modulating the diode laser with the optical chopper at 11 Hz.

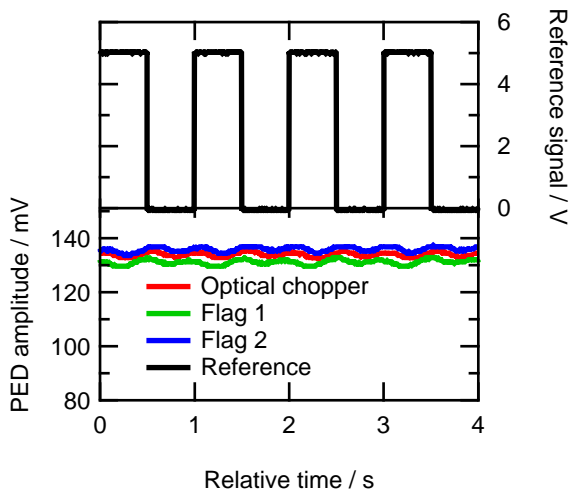


**Figure 7.11:** Amplitude of PED transients, as measured with the lock-in amplifier. The diode laser is modulated at 1 Hz using the optical chopper (red), first beam flag (green), or second beam flag (blue).

molecular beam with approximately 1 Hz. Figure 7.11 compares the signal amplitude when modulating the diode laser with the optical chopper, first flag, or second flag at 1.0 Hz. Overall, the amplitudes for the optical chopper and second beam flag are relatively similar. The first flag amplitude is slightly lower as a result of its gating function. It is a spring-loaded solenoid valve that opens faster than it closes, resulting in a slightly lower amplitude. The difference is minimal though.

With the PED working properly with the three methods of modulation, we can impinge a pure  $\text{CO}_2$  beam expanded from a room temperature nozzle onto the detector. Both methods of modulation worked properly for the diode laser. Upon measuring the  $\text{CO}_2$  beam, flag 2 modulation exhibited a significant amount of crosstalk (3 mV). While this was resolved by shielding the PED cables, results presented here were measured with flag 1 modulation without shielding. Figure 7.12 presents the PED amplitude measured with the lock-in amplifier. Flag 2 is either continuously open (green) matching flag 1 modulation or continuously closed (blue). Flag

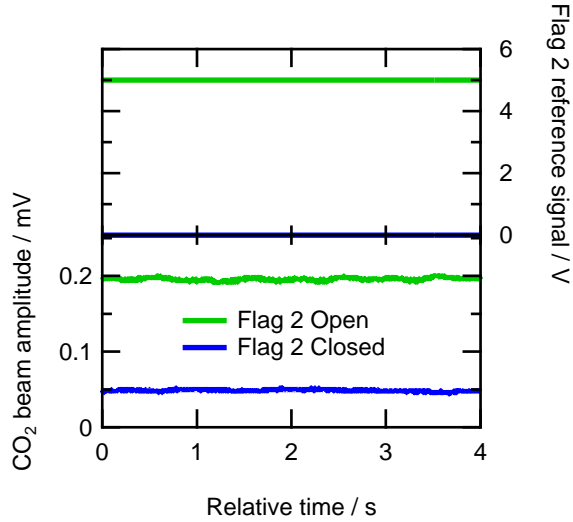


**Figure 7.12:** PED amplitude measured with the lock-in amplifier. The CO<sub>2</sub> molecular is modulated at 1 Hz using the first beam flag. Flag 2 is either continuously open (green) or continuously closed (blue).

2 being closed is a measure for crosstalk and CO<sub>2</sub> molecules striking the detector after scattering off flag 2. When flag 2 is open, the only difference is that CO<sub>2</sub> molecules can directly impinge onto the detector. We observe a 150  $\mu$ V amplitude as a result, showing CO<sub>2</sub> molecules impinging the detector with 1.0 Hz.

Finally, we can move on to attempt detecting vibrationally excited CO<sub>2</sub> molecules in the supersonic molecular beam. Ordinarily, the best way to do this is by modulating the idler before it crosses the CO<sub>2</sub> beam and using lock-in amplification. For us, this presented a problem because we observe photons scattering off the CaF<sub>2</sub> windows. Instead, we take a similar approach as we did for detecting the CO<sub>2</sub> beam. We now compare the PED amplitude of actively stabilized idler radiation with off-resonance idler radiation. We emphasize that the idler is continuously on, while the lock-in amplifier detects only modulating signals. By modulating the CO<sub>2</sub> beam with 1 Hz, we either increase the internal energy of the CO<sub>2</sub> beam when the idler is resonant, or the internal energy remains the same. Figure 7.13 presents

the results. Figure 7.10a schematically shows where the idler crosses the CO<sub>2</sub> beam. Simultaneously with the PED amplitude, idler power is measured with the calibrated power meter after exiting the UHV. Two observations points towards CO<sub>2</sub> excitation in the molecular beam. First, the average PED amplitude for actively stabilized idler ( $189.6 \pm 0.10$   $\mu$ V) is higher than for off-resonance idler ( $186.2 \pm 0.10$   $\mu$ V). Second, idler power is slightly lower when it is resonant with CO<sub>2</sub> ( $26.5 \pm 0.5$  mW) than when the idler is tuned off-resonance ( $27.7 \pm 0.4$  mW), suggesting absorption by the beam.

We now discuss these results and their implications. Figure 7.13 shows that when the idler is stabilized, we observe a larger PED amplitude and lower idler power than when the idler is off-resonance. This is a consequence of vibrationally excited CO<sub>2</sub> in the molecular beam. The next step in the experiment is to determine the fraction of excited CO<sub>2</sub> by varying the idler power using the attenuator (Altechna, Watt Pilot). However, the amplitude increase for excited CO<sub>2</sub> (3.4  $\mu$ V) is rather small. By comparison,  $E_{kin}$  from the pure room temperature CO<sub>2</sub> beam gives approximately 50 times more signal. From time of flight, we measure that  $E_{kin}$  is approximately 80 meV, while the rovibrational transition is 291 meV. There is a large discrepancy between the energy difference and the measured result. There are three explanations why there may be very little signal. First, the idler may not be adequately locked to the rovibrational transition. Second, the power may be too low for sufficient vibrational excitation (or the angle of the idler with the molecular beam is not 90°). Third, CO<sub>2</sub> may not be transferring its vibrational energy to the PED as efficiently as CH<sub>4</sub> does in the experiments by the groups of Art Utz and Rainer Beck. The first explanation is difficult to confirm if the third explanation is also part of the problem. Ideally, we confirm a good lock by using the pyroelectric detector signal. The second explanation seems unlikely, as Miller [143] used approximately 10 mW to show vibrational excitation of an HF beam. Similarly, Juurlink et al.[142] measured vibrational excitation of a CH<sub>4</sub> beam using just 2 mW of power. The third explanation may actually be the most plausible. For a 0.35 eV CH<sub>4</sub> beam, Yoder et al.[136] measure

1.5 V from the PED, after 10 x amplification. By comparison, we observe only 0.1% of this for our pure CO<sub>2</sub> beam. It has less  $E_{kin}$  to deposit, but more molecules to do so.

New experiments can ascertain the validity of these explanations. The first explanation is difficult to test on its own. Extra time focused on achieving a tighter lock may prove in vain. The second explanation can be confirmed or disproven by measuring PED signal as a function of idler power. The third explanation can be tested by using a different molecule, preferably with a rovibrational transition in range of our OPO module, and comparing its absolute PED signal to that of CO<sub>2</sub>. Methane or acetylene are viable options that may not require purging, thereby making it easier to setup the experiments. Without excitation, the former enables direct comparison to results from the groups of Utz and Beck. If CH<sub>3</sub>D or CD<sub>4</sub> is available, the quality of the lock can be verified by respectively exciting the  $\nu_1$  or  $\nu_3$  vibration. The PED signal can then also be compared to those from Utz et al. and Beck et al. for different isotopes.

The alternative to methane, acetylene, is a linear molecule with point group D<sub>∞h</sub>, similar to CO<sub>2</sub>. It is likely to be more reactive than CO<sub>2</sub>, thereby possibly generating more signal at the PED. When using the C<sub>2</sub>D<sub>2</sub> isotope, the OPO can access the  $\nu_3$  asymmetric stretch vibration for comparison to the CO<sub>2</sub> PED signal. This could potentially set up future experiments that look at state-resolved acetylene dissociation, ideally using RAIRS to identify adsorbed species. Comparison of vibrational efficacies for the two linear molecules – CO<sub>2</sub> and C<sub>2</sub>D<sub>2</sub> – would be an interesting venture for understanding gas-surface dynamics of linear polyatomic molecules. CO<sub>2</sub> is rather stable with a Gibbs free energy of -394.4 kJ/mol, while the latter is somewhat unstable with +209.2 kJ/mol.[144] To what extent asymmetric stretch vibrational energy assists in dissociating the two molecules may prove insightful in understanding dissociation of linear polyatomic molecules at catalytic surfaces.

In conclusion, we presented the basics of  $\text{CO}_2$  spectroscopy and the initial steps for state-resolved  $\text{CO}_2$  dissociation. Vibrationally excited  $\text{CO}_2$  was detected in the supersonic molecular beam. Quantifying the amount of excitation in the molecular beam requires more signal at the PED. However, it is unclear why the absolute PED signal is so low. Suggestions are made for future experiments to identify the cause. One suggestion for new experiments involves using acetylene, a different linear molecule, and to eventually compare state-resolved dissociation experiments for  $\text{CO}_2$  and acetylene.

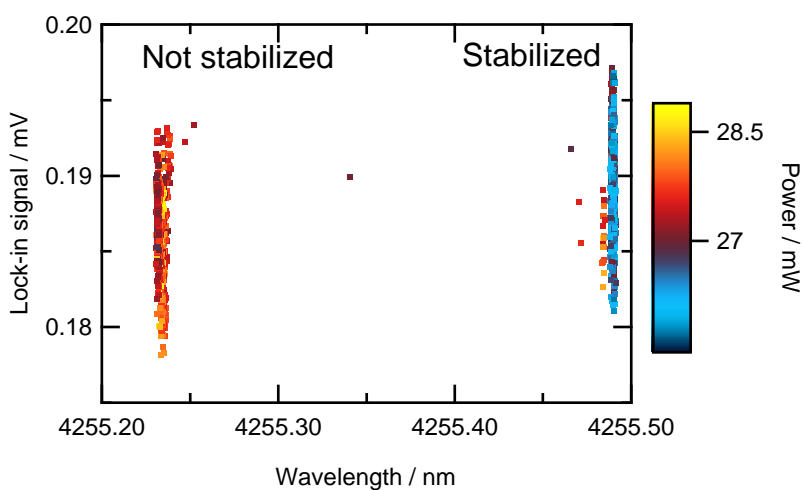


**Figure 7.13:** PED amplitude measured as a function of wavelength. The CO<sub>2</sub> molecular is modulated at 1.0 Hz using the first beam flag. Flag 2 is continuously open. The idler crosses the CO<sub>2</sub> molecular beam continuously, but is either frequency stabilized onto the R(0) transition or the stabilization is switched off so that the idler is off resonance.





---

**Summary and conclusion**

---

Platinum is one of the best heterogeneous catalysts for hydrogenation and oxidation reactions. Throughout the first half of this thesis, we investigated how step edges at platinum surfaces influence surface reactivity. To this end, experimental techniques were adapted for use with curved single crystal surfaces. The chapters involve various steps relevant to oxygen reduction: hydrogen dissociation (chapter 3), hydrogen recombination (chapter 4), and overall oxygen reduction (chapter 5).

Chapter 3 investigates hydrogen dissociation on platinum. As one of the simplest heterogeneous catalytic reactions, hydrogen dissociation on Pt(1 1 1) has been described by two dynamical models that are fundamentally at odds. Whereas one model assumes predominant indirect dissociation at defects via diffusion, the other is based on direct or local dissociation at the site of impact. In chapter 3, we resolve this dispute by quantifying how reactivity depends on surface structure. We do this by employing a spatially resolved molecular beam in conjunction with a curved Pt single crystal surface with varying step density. We observe that reactivity varies linearly with step density and is step-type dependent. Only the model that relies on dissociation localized at the point of impact is consistent with these results and enables us to extract step-type specific reaction cross sections. These absolute reaction cross sections are a direct measure for dissociation at the clean surface.

In chapter 4, we discuss the simplest heterogeneously catalyzed reaction possible: isotopic scrambling of hydrogen. On Pt, this reaction occurs by dissociative adsorption of  $\text{H}_2$  and  $\text{D}_2$ , mixing of H and D atoms on the surface, and recombination to form the three isotopologues,  $\text{H}_2$ ,  $\text{D}_2$ , and HD.

Full isotopic scrambling would lead to a product ratio of approximately 1:1:2. Step edges are well-known to enhance dissociative adsorption, especially at low impact energies. However, it is unknown whether subsequent diffusion and desorption only occurs along the steps or involves diffusion onto terraces. We study this by combining supersonic molecular beam techniques with a curved Pt single crystal surface with straight **A-** and **B-type** step edges, c-Pt(1 1 1)[1  $\bar{1}$  0]31°. At a high surface temperature, we probe HD formation along the curved surface by dissociating equal amounts of low energy H<sub>2</sub> and D<sub>2</sub>. HD formation tracks the trend in dissociation: higher step densities yield higher HD formation. However, HD formation is not enhanced at steps to the same extent as the dissociation probability. We explain why extended (1 1 1) terraces are more selective toward HD formation than highly stepped surfaces. At (1 1 1), diffusion is fast and isotropic. In contrast, diffusion at steps is slower and anisotropic. Consequently, steps exhibit lower selectivity in isotopic scrambling. A simple model that assumes isotropic mixing at terraces and anisotropic mixing at steps agrees well with our results.

In chapter 5, we investigate the step-type dependence for the overall oxygen reduction reaction using a double molecular beam system. We compare how overall oxygen reduction reactivity varies with the oxygen hydrogen ratio provided to the surface. Our results show that oxygen reduction on Pt is also step-type dependent. Under oxygen-lean conditions, oxygen dissociation probabilities are significantly higher at **B-type** steps than **A-type** steps. Despite higher reactivity for oxygen dissociation, the surface with **B-type** steps is depleted of adsorbed oxygen before the surface containing **A-type** steps. We argue that higher reactivity with **B-type** steps results from higher reaction probabilities for all relevant reactants: oxygen, hydrogen, and deuterium.

The second half of this thesis develops experimental techniques aimed at studying state-resolved CO<sub>2</sub> dissociation. First, chapter 6 adapts Reflection Absorption Infrared Spectroscopy (RAIRS) for use on curved single crystal surfaces. The curved sample and a coaxial collimator form an anamorphic beam expander. As proof-of-principle, we investigate how steps influence

CO adsorption on Pt. Initially, both wide and narrow terraces show narrow single absorption peaks, while intermediate widths exhibit broad features. These features are attributed to absorption by on-top bound CO at terrace and step sites. We explain our results in terms of single excitons that absorb IR radiation.  $(1\ 1\ 1)$  and high step density surfaces form constant density islands that absorb at a single frequency. In contrast, the constant density island of the  $(1\ 1\ 1)$  terrace are interrupted by steps for intermediate terrace widths, thereby broadening the absorbance features. Further improvements to the technique are suggested.

Chapter 7 presents an outlook for performing state-resolved  $\text{CO}_2$  dissociation experiments. We provide a basic explanation of  $\text{CO}_2$  spectroscopy and develop an optical excitation setup. The optical setup resolves around an Optical Parametric Oscillator that is actively stabilized to the Lamb dip of the transition of interest. We present initial results that show excited  $\text{CO}_2$  in the molecular beam.

The work throughout this thesis paves the way for future work studying dynamics at surfaces. By combining curved single crystal surfaces with molecular beams, we can extract absolute reaction cross sections for defects. Thus far, we have only applied this to low kinetic energy hydrogen dissociation. In future work, this combination can be used to resolve the kinetic energy dependence of hydrogen dissociation at defects. This combination can be applied to other model systems as well. Curved surfaces are particularly well-suited to investigate whether specific reactions require diffusion toward an active site. The absolute reaction cross sections that are extracted from this technique provide new benchmarks for DFT. In particular, they test how well van der Waals corrections work for these model system.

Double beam experiments are similarly powerful, but were only applied to flat single crystal surfaces in this thesis. We highlight four questions that remain unanswered. First, the kinetic energy dependence for the two reactants was not touched upon in this work. Studies involving oxygen dissociation suggest that the step-type dependence inverts at higher  $\text{O}_2$  incidence energy. Second, OH and OOH intermediates have been suggested

for the reaction. Reflection Absorption Infrared Spectroscopy may be employed to perform *in operando* catalysis under UHV conditions, potentially identifying these key intermediates and their adsorption site. Thirdly, the effect of step density has not been resolved in this work, nor have we been able to study the actual overall kinetics of the reaction. If Molecular Beam Relaxation Spectroscopy can be applied to curved surfaces, we can resolve how the overall oxygen reduction kinetics depend on step density. Our previous results from desorption experiments suggest **B-type** steps are kinetically favorable. These experiments can unequivocally confirm this, as well as the nature of the active site. Finally, this combination can resolve whether diffusion towards an active site is rate limiting, as is suggested in literature.

The work presented throughout this thesis also open up a great number of experiments involving CO<sub>2</sub>. In addition to the combination of techniques discussed above, we also have control over the quantum state of CO<sub>2</sub>. This opens up many new possibilities of studying gas-surface dynamics. Mechanistic insights made for methane can also be investigated for CO<sub>2</sub>. We highlight five notable experiments for future work. First and foremost, we can compare the kinetic and vibrational energy dependence of CO<sub>2</sub> dissociation to extract the vibrational efficacy. Reactivity is expected to be quite low, so RAIRS can be applied to quantify reactivity. Second, RAIRS can identify the reaction site(s) (steps vs terraces). Third, experiments that rotate the polarization of the infrared radiation can resolve whether CO<sub>2</sub> dissociation depends on vibrational alignment of the molecule. Fourth, state-resolved CO<sub>2</sub> scattering is of interest as well. We know that methane scattering is non-adiabatic. Vibrational energy is efficiently redistributed from the antisymmetric stretch to the symmetric stretch in the collision. These vibrational modes are separated by only 131 cm<sup>-1</sup>. (3025.5 cm<sup>-1</sup> vs 3156.8 cm<sup>-1</sup>) Similar experiments would be of great interest for CO<sub>2</sub>. The antisymmetric stretch vibration for CO<sub>2</sub> is significantly higher in energy than the other two normal modes. (Chapter 7) Finally, state-resolved experiments can be applied to other polyatomic molecules. Of particular interest is acetylene, C<sub>2</sub>H<sub>2</sub>, which is also a linear molecule. Unlike

CO<sub>2</sub> however, it has more vibrational degrees of freedom than CO<sub>2</sub> and is thermodynamically unstable. Direct comparison between state-to-state scattering of these two molecules would give fundamental insight in how energy is redistributed during gas-surface collisions.



---

**Nederlandse samenvatting**

---

Platina is één van de beste heterogene katalysatoren voor hydrogenering en oxidatie reacties. In de eerste helft van dit proefschrift hebben we onderzocht hoe reactiviteit wordt beïnvloed door stapranden aan platina oppervlakken. Derhalve hebben we experimentele methoden voor gebruikelijk vlakke kristallen aanpast voor gekromde éénkristallijne oppervlakken. Hoofdstukken 3, 4 en 5 buigen zich over verschillende aspecten van zuurstof reductie: waterstof dissociatie (hoofdstuk 3), waterstof recombinitie (hoofdstuk 4), en de complete zuurstof reductie reactie (hoofdstuk 5).

In hoofdstuk 3 onderzoeken we waterstof dissociatie aan platina oppervlakken. Waterstof dissociatie is één van de meest eenvoudige oppervlakte reacties. Desondanks wordt deze reactie beschreven door twee tegenstrijdige dynamische modellen. Het eerste model neemt aan dat dissociatie verloopt via een indirect dissociatie mechanisme waarbij moleculen wrijvingsloos naar de katalytisch actieve stapranden diffunderen. Het tweede model stelt dat dissociatie direct en lokaal is. In hoofdstuk 4 lossen we deze discussie op door de structuurafhankelijke reactiviteit van een gekromd platina oppervlak te kwantificeren. Dit doen we door een moleculaire  $D_2$  bundel te combineren met de variërende stapdichtheid van een gekromd éénkristallijn oppervlak. We zien dat reactiviteit proportioneel is met stapdichtheid. Daarnaast is de reactiviteit ook stap-type afhankelijk. Alleen het model dat reactiviteit beschrijft als directe en lokale dissociatie is consistent met deze resultaten. Vervolgens kunnen we uit onze data stap-type afhankelijke reactie dwarsdoorsneden afleiden. Deze absolute reactie dwarsdoorsneden zijn een directe maat voor dissociatie aan het schone platina oppervlak.

In hoofdstuk 4 bestuderen we de meest simpele heterogeen gekatalyseerde reactie: isotoop uitwisseling van waterstof. Aan platina verloopt deze reactie als een standaard Langmuir Hinshelwood mechanisme: waterstof en deuterium dissociatie, menging van geadsorbeerde waterstof en deuterium atomen aan het oppervlak, en recombinatie om drie isotopen te vormen ( $\text{H}_2$ ,  $\text{D}_2$ , en  $\text{HD}$ ). Bij volledige isotoop uitwisseling zal een product verhouding van 1:1:2 vormen. Stap randen staan er om bekend dat ze dissociatieve adsorptie bevorderen, in het bijzonder bij lage kinetische energie. Het is echter niet bekend hoe diffusie en product vorming beïnvloed worden door stap randen. We bestuderen dit door een gelijke hoeveelheid  $\text{H}_2$  en  $\text{D}_2$  te dissociëren aan een éénkristallijn gekromd platina oppervlak door middel van een moleculaire bundel. We meten de  $\text{HD}$  vorming langs het gekromde kristal bij hoge oppervlak temperaturen. Hoewel de  $\text{HD}$  vorming de algemene trend van  $\text{H}_2$  en  $\text{D}_2$  dissociatie volgt, zijn stapranden niet zo reactief als verwacht op basis van de dissociatie waarschijnlijkheden. We verklaren vervolgens waarom langere (1 1 1) terrassen klaarblijkelijk selectiever zijn voor  $\text{HD}$  vorming dan gestapte oppervlakken. Diffusie van waterstof en deuterium atomen aan (1 1 1) terrassen is snel en isotroop. Daarentegen zijn diffusie barrières aan stapranden significant hoger. Hierdoor verhinderen stapranden menging van waterstof en deuterium atomen aan het oppervlak. We presenteren een simpel model waarbij waterstof en deuterium isotroop mengen aan terrassen, maar niet efficiënt mengen aan stapranden. Het model reproduceert de trend in de selectiviteit van  $\text{HD}$  vorming.

In hoofdstuk 5 bestuderen we de stap-type afhankelijk van zuurstof reductie met behulp van twee moleculaire bundels. We vergelijken hoe de reactiviteit voor zuurstof reductie varieert met de zuurstof waterstof verhouding die wordt aangeboden aan het oppervlak. Onze resultaten tonen aan dat zuurstof reductie aan platina ook gevoelig is voor stap-type. Bij een ondermaat zuurstof is het oppervlak met **B-type** stapranden reactiever dan het oppervlak met **A-type** stapranden. Ondanks deze hogere reactiviteit voor zuurstof dissociatie is zuurstof alsnog sneller van het oppervlak met **B-type** stapranden verwijderd. We verklaren dat de hogere reactiviteit van



**B-type** stapranden een gevolg is van hogere dissociatie waarschijnlijkhe-  
den voor alle betrokken reactanten in de reactie: zuurstof, waterstof, en  
deuterium.

De twee helft van dit proefschrift beschrijft experimentele technieken  
die ontwikkeld zijn om toestands-geselecteerde  $\text{CO}_2$  dissociatie te bestud-  
eren. Allereerst beschrijft hoofdstuk 6 hoe we reflectie absorptie infra-  
rood spectroscopie toe kunnen passen aan gekromde oppervlakken. Het  
gekromde oppervlak en een coaxiale collimator vormen een anamorfe bun-  
del vergroter. We bestuderen hoe stapranden aan een platina oppervlak  
CO adsorptie beïnvloeden als vuurdoop voor de techniek. Zowel brede  
als smalle terrassen vertonen een enkele smalle absorptie piek. Gemiddelde  
terras breedten vertonen echter bredere absorptie pieken. We verklaren  
deze resultaten in termen van een enkele exciton die infrarode straling  
absorbeert. Bij smalle en brede terrassen vormen CO eilanden met een  
uniforme oppervlakte structuur. Bij de gemiddelde terrassen worden de  
structuren die bij  $(1\ 1\ 1)$  vormen onderbroken door de stapranden. Dit  
verbreedt de resulterende absorptie pieken. Ten slotte worden verbeterin-  
gen voorgesteld voor de techniek.

Hoofdstuk 7 presenteert een vooruitzicht op toestands-geselecteerde  
 $\text{CO}_2$  dissociatie. We beschrijven de spectroscopie van  $\text{CO}_2$  en een op-  
stelling om  $\text{CO}_2$  rovibraties aan te slaan in de moleculaire bundel. De  
excitatie opstelling maakt gebruik van een optische parametrische oscil-  
lator, welke actief gestabiliseerd wordt op de Lamb dip van de optische  
transitie. Ten slotte presenteren we de eerste resultaten die aantonen dat  
 $\text{CO}_2$  in de moleculaire bundel vibrationeel aangeslagen is.



---

**IGOR Pro procedures**


---

This appendix contains IGOR Pro procedures that were used to simulate and/or analyze experimental data.

**Beam profile simulation: orifice**

The following procedure calculates the fractional overlap between two circles as a function of on-axis translation. The center of the two circles lie on this common axis. It is used in the beam profile experiments in chapter 2. It generates the solid lines in figure 2.7.

```
function circlecircle_intersection (r1, r2, d0, dmax, deltad)
Variable r1, r2, d0, dmax, deltad
Make /O /N=(abs((d0 - dmax) / deltad)+2) Overlap, d
variable i
deltad = (d0 - dmax) / (numpnts(Overlap)-1)
for (i=0; i < numpnts(Overlap); i+=1)
  d[i] = d0 - i*deltad
  if (abs(d[i]) <= abs(r1-r2) && r1 >= r2)
    Overlap[i] = pi*r2^2
  elseif (abs(d[i]) <= abs(r1-r2) && r1 < r2)
    Overlap[i] = pi*r1^2
  else
    Overlap[i] = r1^2*acos((d[i]^2+r1^2-r2^2)/(2*abs(d[i])*r1)) +
      r2^2*acos((d[i]^2+r2^2-r1^2)/(2*abs(d[i])*r2)) -
      0.5*sqrt( (-abs(d[i])+r1+r2)*(abs(d[i])+r1-r2) *
        (abs(d[i])-r1+r2) * (abs(d[i])+r1+r2) )
```

```
    endif
endfor
wavestats /q Overlap
Overlap = Overlap / v_max
End
```

**Beam profile simulation: slit (vertical translation)**

The following IGOR Pro procedure calculates the overlap between a rectangle and a circle as a function of on-axis translation. The centers of the circle and the rectangle lie on this common axis. The rectangle is wider than the circle diameter. It is used in the beam profile experiments in chapter 2. It generates the solid black line (vertical translation) in figure 2.8.

```
function circlerectangle_intersection (r1, x2, y2, d0, dmax, deltad)
Variable r1, x2, y2, d0, dmax, deltad
Make /O /N=(abs((d0 - dmax) / deltad)+2) Overlap, d
variable i
deltad = (d0 - dmax) / (numpnts(Overlap)-1)
for (i=0; i < numpnts(Overlap); i+=1)
  d[i] = d0 - i*deltad
  if ( abs(d[i]) >= (r1 + 0.5*y2) )
    //no overlap
    Overlap[i] = 0
  elseif ( y2 > 2*r1 && abs(d[i]) < abs(0.5*y2-r1) )
    //rectangle is longer and wider than circle diameter (complete overlap)
    Overlap[i] = pi*r1^2
  elseif ( abs(d[i]) > (r1 - 0.5*y2) )
    //Rectangle falls off the circle edge
    Overlap[i] = r1^2 * acos( (abs(d[i]) - 0.5*y2) / r1) -
      (abs(d[i])-0.5*y2)*sqrt( r1^2 - (abs(d[i])-0.5*y2)^2 )
  else
    //The circle extends past the rectangle on both sides.
    Overlap[i] = ( r1^2 * acos( (abs(d[i]) - 0.5*y2) / r1) -
      (abs(d[i])-0.5*y2)*sqrt( r1^2 - (abs(d[i])-0.5*y2)^2 ) ) -
      (r1^2 * acos( (abs(d[i]) + 0.5*y2) / r1) -
      (abs(d[i]) + 0.5*y2)*sqrt( r1^2 - (abs(d[i]) + 0.5*y2)^2 ) )
  endif
endfor
```

```
Overlap = Overlap / (pi*r1^2)  
End
```

**Beam profile simulation: orifice (horizontal translation)**

The following IGOR Pro procedure calculates the overlap between a rectangle and a circle as a function of on-axis translation. The centers of the circle and the rectangle lie on this common axis. The rectangle is narrower than the circle diameter. It is used in the beam profile experiments in chapter 2. It generates the solid red line (horizontal translation) in figure 2.8.

```
function circirectang_leintersection2 (r1, x2, y2, d0, dmax, deltad)
Variable r1, x2, y2, d0, dmax, deltad
Make /O /N=(abs((d0 - dmax) / deltad)+2) Overlap, d
variable i
deltad = (d0 - dmax) / (numpnts(Overlap)-1)
for (i=0; i < numpnts(Overlap); i+=1)
  d[i] = d0 - i*deltad
  if ( abs(d[i]) >= (r1 + 0.5*x2) )
    //rectangle is not crossing the circle
    Overlap[i] = 0
    Overlap[i] = r1^2 * asin(0.5*y2/r1) - 0.5*y2*sqrt(r1^2 - (0.5*y2)^2) +
    y2 * (sqrt(r1^2-(0.5*y2)^2) - (abs(d[i]) - 0.5*x2))
  elseif ( abs(d[i]) < (r1 + 0.5*x2) ) &&
    0.5*y2 < sqrt(r1^2 - (abs(d[i]) - 0.5*x2)^2) &&
    -sqrt( r1^2 - (0.5 * y2)^2) > (abs(d[i] - 0.5*x2)) > - r1 )
    Overlap[i] = pi * r1^2 - 2 * ( r1^2*acos(0.5*y2/r1) -
    0.5*y2*sqrt(r1^2 - (0.5*y2)^2)) -
    (r1^2 * acos( (abs(d[i]) - 0.5*x2) /r1) -
    (abs(d[i]) - 0.5*x2)*(sqrt( r1^2 - (abs(d[i])-0.5*x2)^2)))
  else
    Overlap[i] = pi * r1^2 - 2 * ( r1^2*acos(0.5*y2/r1) -
    0.5*y2*sqrt(r1^2 - (0.5*y2)^2))
  endif
endfor
Overlap = Overlap / (pi*r1^2)
```

End



## Chopper gating function simulation

The following IGOR Pro procedure generates the IGOR Pro fit function used for Time of Flight analysis. The slit in the chopper blade generates a pulse of molecules. The length of this pulse broadens the peaks in the time of flight. We account for this broadening effect by broadening the fit function with the chopper gating function. The following IGOR Pro procedure uses a similar approach as vertical translation for the slit-shaped orifice. However, it calculates the gating function with the same temporal resolution as the time of flight data.

```
function chopper (freq)
//chopper frequency
variable freq
variable r1, Y2, d0, dmax, deltad, r_chopper, i, dap
// beam radius at chopper
r1 = 0.23
// slit width
Y2 = 0.85
//travel distance of chopper runs from d0 - > dmax
d0 = -(0.23*2 + 0.85)/2
// travel distance of chopper runs from d0 - > dmax
dmax = (0.23*2 + 0.85)/2
// chopper radius (to where it chops the molecular beam)
r_chopper = 55.992
// datapoint time constant
dap = 5*10^-7
deltad = 2*pi*dap * r_chopper * freq //
make /O /N=(round(abs((d0-dmax) / deltad))+3) gating
make /O /N=(round(abs((d0-dmax) / deltad))+3) timing
make /O /N=(round(abs((d0-dmax) / deltad))+3) d
dmax = (round(abs((d0-dmax)/deltad))+2)*2*pi*dap*r_chopper*freq/2
d0 = -dmax
deltad = (d0 - dmax) / (numpnts(d)-1)
```

```

string/G TMBstr = "TMB="
for (i=0; i < numpnts(d); i+=1)
  d[i] = d0 + i*2*pi*dap * r_chopper * freq
  if ( abs(d[i]) >= (r1 + 0.5*y2) )
    //No overlap
    gating[i] = 0
  elseif ( y2 > 2*r1 && abs(d[i]) < abs(0.5*y2-r1) )
    //circle is smaller than rectangle and completely overlaps
    gating[i] = pi*r1^2
  elseif ( abs(d[i]) > (r1 - 0.5*y2) )
    //Rectangle is narrower than circle and only partially overlaps circle
    gating[i] = r1^2 * acos( (abs(d[i]) - 0.5*y2) / r1) -
      (abs(d[i])-0.5*y2)*sqrt( r1^2 - (abs(d[i])-0.5*y2)^2)
  else
    //Rectangle intersects circle
    gating[i] = (r1^2 * acos( (abs(d[i]) - 0.5*y2) / r1) -
      (abs(d[i])-0.5*y2)*sqrt(r1^2-(abs(d[i])-0.5*y2)^2)) -
      (r1^2 * acos( (abs(d[i]) + 0.5*y2) / r1) -
      (abs(d[i])+0.5*y2)*sqrt(r1^2-(abs(d[i])+0.5*y2)^2)))
  endif
  gating[i] /= (pi*r1^2)
  timing[i] = d[i] / (2*pi*55.992*253)*1000
//Write the TOF fit function:
if (i < (numpnts(d) - 1))
  TMBstr += num2str(gating[i]) +
    "(w[3]/(t-"+num2str(timing[i])+"-w[4]-delta))^4 *
    exp(-(w[3]/(t-"+num2str(timing[i])+"-w[4]-delta) -
    (w[3]/(w[5]-delta)))^2)/(alfa^2))+"
else
  TMBstr += num2str(gating[i]) +
    "(w[3]/(t-"+num2str(timing[i])+"-w[4]-delta))^4 *
    exp(-(w[3]/(t-"+num2str(timing[i])+"-w[4]-delta) -
    (w[3]/(w[5]-delta)))^2)/(alfa^2))"

```

```
endif  
endfor  
print TMBstr  
End
```



All experiments were performed in a homebuilt supersonic molecular beam ultra-high vacuum (UHV) apparatus. The base pressure of the UHV chamber is  $<1\cdot10^{-10}$  mbar. The UHV chamber contains, amongst others, low energy electron diffraction (LEED) / Auger electron spectroscopy (AES) optics (BLD800IR, OCI Vacuum Microengineering), a quadrupole mass spectrometer (QME200, Pfeiffer vacuum) for residual gas analysis and King and Wells (KW) measurements, and an on-axis quadrupole mass spectrometer (UTI-100C) for time-of-flight (TOF) experiments.

The UHV chamber holds our curved Pt single crystal (Surface Preparation Lab). It is cooled using a liquid nitrogen cryostat and heated by radiative heating and electron bombardment using a filament. The Pt single crystal was cleaned with repeated cycles of sputtering ( $6\cdot10^{-6}$  mbar Ar, Messer 5.0, 0.5 kV, 1.3  $\mu$ A, 910 K, 50°, 5 min), oxidation ( $3.5\cdot10^{-8}$  mbar O<sub>2</sub>, Messer 5.0, 910 K), and *in vacuo* annealing (1200 K). For the final cleaning cycle, the Pt crystal is only sputtered and annealed at 910 K. Surface quality was verified using LEED and AES.

The double differentially pumped supersonic beam of D<sub>2</sub> is formed by expanding a gas mixture from a W nozzle with a 28  $\mu$ m orifice. The center of the expansion is selected using a skimmer. A second skimmer and a sliding valve with different orifices create the molecular beam of variable size and shape within the UHV chamber. For the measurements, we use a slit as the defining orifice in the sliding valve. The molecular beam can be modulated by a mechanical chopper for time of flight spectroscopy or a pair of flags for King and Wells experiments.[11]

## Time of Flight

The kinetic energy ( $E_{kin}$ ) of the  $D_2$  beam is varied by seeding in  $H_2$  or anti-seeding in Ar. TOF spectra are measured at 6 different on-axis mass spectrometer positions. The resulting TOF spectra are fitted with the functional form for a density-sensitive detector:[54]

$$f(t) = \left(\frac{l}{t}\right)^4 \cdot e^{-\left(\frac{\frac{l}{t} - \frac{l}{t_0}}{\alpha}\right)^2} \quad (B.1)$$

where  $l$  is the neutral flight path,  $t$  is the neutral flight time,  $t_0$  is the stream flight time and  $\alpha$  is the width of the distribution. There are several offsets between the measured time and the actual neutral flight time. To determine the total offset,  $t_{offset}$ , TOF spectra are measured at 6 different QMS positions and fitted with a Gaussian function. We use linear regression on the resulting peak positions to extrapolate to  $l = 0$  to extract  $t = t_{offset}$ . We subtract  $t_{offset}$  from the measured time, leaving only the neutral flight time  $t$  expressed in equation B.1. The TOF spectra are subsequently fitted with equation B.1. After redimensioning the fits using the appropriate Jacobian for transformation,[54] we obtain the two energy distributions in figure B.1.

## Model 1 predictions

The predictions by model 1[61, 62] shown in figure 3.3 for the zero coverage limit are calculated by:

$$\tau = \frac{h}{k_B T_s} e^{\left(\frac{\eta E_W}{k_B T_s}\right)} \quad (B.2)$$

$$S_0 = S_{0nL} \frac{\nu \tau}{L_d} \left(1 - e^{\left(-\frac{L_d}{\nu \tau}\right)}\right) + 0.24 \theta_d \quad (B.3)$$

The residence time  $\tau$  depends on the precursor well depth  $E_W$ , and  $T_s$ .  $S_0$  is the summation of two terms. The first term multiplies the probability of capture into the physisorbed state ( $S_{0nL}$ ) with the probability of reaching a defect. The latter probability depends on  $\tau$ , the incident velocity ( $\nu$ ), and the average distance between defects ( $L_d$ ). The second term quantifies a minor contribution, i.e. the probability of dissociation through direct

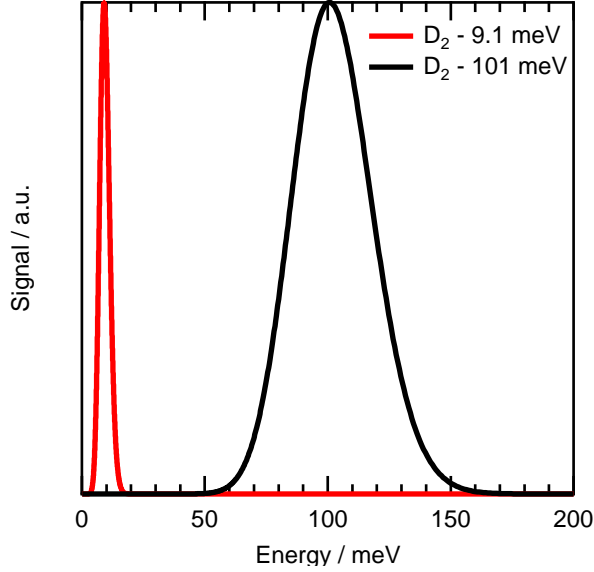


**Figure B.1:** Fitted flux-weighted energy distributions for the  $D_2$  beams used in chapter 3, showing a most probable  $E_{kin}$  (FWHM) of 9.1 (4.7) meV and 101 (38) meV.

impact on defects. It equals 0.24 times the fractional defect density ( $\theta_d$ ). The fractional step density can be converted to step density in  $\text{nm}^{-1}$  by dividing by the Pt-Pt row distance for (1 1 1): 0.277 nm.[62] The value obtained for Pt(3 3 5) in this manner agrees with values used by Poelsema et al.[62] Besides Planck's constant ( $h$ ), and Boltzmann's constant ( $k_B$ ), the model requires an additional fit parameter ( $\eta$ ) and assumes a  $\theta_d$  dependence for  $E_W$ . [62]

The absolute values used in the model 1 predictions were extracted from the original publications by Poelsema et al.[61, 62] The values are shown in table B.1.

Table B.1: Model 1 simulation parameters.

$S_{0nL}$	0.09
$\eta$	$\frac{1}{1.35}$
$E_W$ (eV)	$0.15L_d^{\left(\frac{0.13F}{N_A}\right)}$
$L_d$	$\frac{0.277}{\theta_D}$
$\nu$	$676.4 \text{ ms}^{-1}$
$T_s$	155 K or 300 K

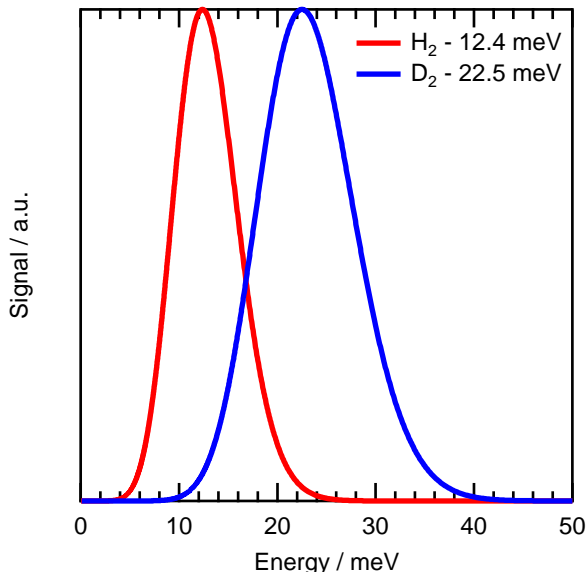


All experiments were performed in Lionfish; an ultra-high vacuum system described previously.[79] Hydrogen and deuterium were mixed with argon and expanded from a room temperature nozzle into the vacuum. Time of flight analysis was performed as described in chapter 2. The kinetic energy distributions resulting from fits to the data are shown in figure C.1 for  $\text{H}_2$  and  $\text{D}_2$ .

### Extracting results for the facettted surface

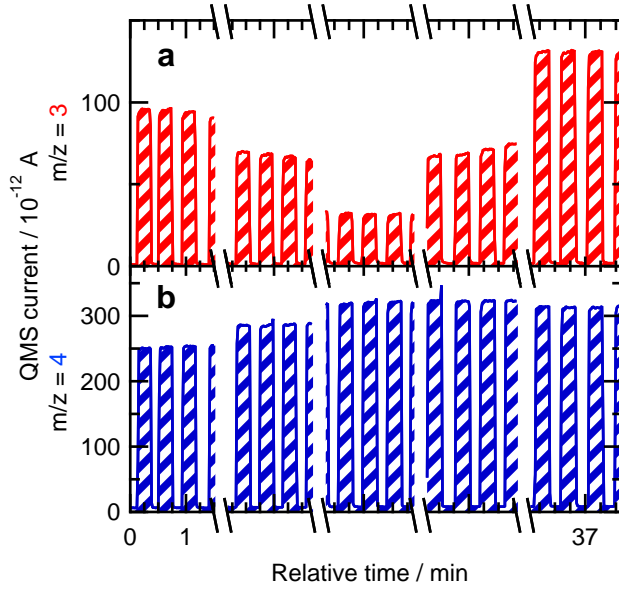
The experiments performed on the facettted Pt surface did not employ the standard King and Wells method. In contrast to the data presented in figure 4.1, the second beam flag (which resides in the UHV) remained open throughout the experiment. As a consequence, HD formation and  $\text{D}_2$  consumption by the facettted Pt(1 1 1) surface cannot be extracted with the standard King and Wells[11] method detailed in chapter 2. For the facettted surface, we use the mass balance between consumed  $\text{D}_2$  and produced HD for normalization. We explain our method in this section.

Figure C.2 shows the data for the reconstructed surface with the same temporal resolution as figure 4.1. First, we discuss the similarities to the raw data already shown in chapter 4. The measured  $\text{D}_2$  pressure is highest at intermediate times, when the beam impinges near the (1 1 1) surface. In contrast, the HD pressure is high at the stepped surface at low and high relative times. There, measured  $\text{D}_2$  pressures are somewhat lowered compared to the intermediate time. It is also clear that the sum of the HD and  $\text{D}_2$  signal gradually increases throughout the experiment.



**Figure C.1:**  $\text{H}_2$  and  $\text{D}_2$  flux-weighted kinetic energy distributions determined from fits to the time of flight. The most probable  $E_{kin}$  (FWHM) for  $\text{H}_2$  and  $\text{D}_2$  are 12.4 (7.6) meV and 22.5 (11.4) meV respectively.

The experiments shown here exhibit significantly higher HD and  $\text{D}_2$  pressures (approximately 20-30 times higher than for figure 4.1). This is a consequence of the larger slit size used to shape the molecular beam for these experiments (0.065 mm vs 0.250 mm). The beam is also open for a shorter period of time (12.5 s total compared to 30 s used previously). The biggest difference to the experiments shown in chapter 4 is that beam flag 2 remained open throughout the entire experiment. Due to missing the convenient normalization factor from scattering off the inert flag, we instead need to extract HD production and  $\text{D}_2$  consumption probabilities by using the mass balance: the HD pressure increase is proportional to the  $\text{D}_2$  pressure drop by the stoichiometry of the reaction. Variations in the ionization energy result in a change in the expected scaling factor. This scaling factor depends on the mass spectrometer settings and are best determined empirically. Fortunately, we have ample data for  $\text{D}_2$  consumption and HD production to do this from the main experimental results in chapter 4.



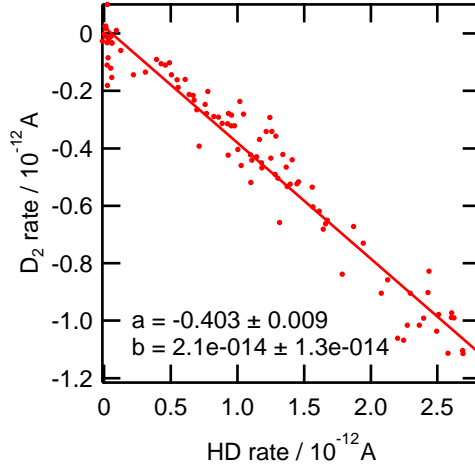
**Figure C.2:** The  $\text{H}_2\text{-D}_2$  beam impinges different parts of the sample. From these data, structure dependent HD production and  $\text{D}_2$  consumption are extracted.

Figure C.3 shows the drop in  $\text{D}_2$  QMS current as a function of the increase in HD QMS current. A clear linear trend is observed. The slope represents the scaling factor between HD and  $\text{D}_2$ . Having determined the scaling factor, we calculate the total current attributed to D atoms present throughout the experiment and normalize to the initial total current. In addition, from the  $\text{D}_2$ , HD and total currents we calculate position (and step density) dependent  $\text{D}_2$  consumption probabilities.

### HD efficacy model

Chapter 4 detailed a simple model predicting HD selectivity at stepped  $\text{Pt}(1\ 1\ 1)$  surfaces. We explain here how equation 4.15 is calculated. We apply the same approach used for  $\text{D}_2$  sticking in chapter 3 and Groot et al.[70] In chapter 4, we were left with:

$$\bar{S}_0 = \alpha \cdot S_0^S + (1 - \alpha) \cdot S_0^T \quad (\text{C.1})$$



**Figure C.3:** Scaling between the D<sub>2</sub> pressure drop and the HD pressure increase.

and

$$\bar{C}_0 = \frac{\alpha}{4} \cdot S_0^S + \left( \frac{1-\alpha}{2} \right) \cdot S_0^T \quad (\text{C.2})$$

These are substituted into equation 4.11:

$$\eta = \frac{\frac{\alpha}{4} \cdot S_0^S + \left( \frac{1-\alpha}{2} \right) \cdot S_0^T}{\alpha \cdot S_0^S + (1-\alpha) \cdot S_0^T} \quad (\text{C.3})$$

This can be simplified to the right hand side of equation 4.15 by realizing that:

$$S_0^S = 32 \cdot S_0^T \quad (\text{C.4})$$

This results in:

$$\eta = \frac{\frac{\alpha}{4} \cdot 32S_0^T + \left( \frac{1-\alpha}{2} \right) \cdot S_0^T}{\alpha \cdot 32S_0^T + (1-\alpha) \cdot S_0^T} = \frac{8 \cdot \alpha + \frac{1}{2} - \frac{\alpha}{2} \cdot S_0^T}{32 \cdot \alpha + 1 - \alpha} = \frac{7.5 \cdot \alpha + \frac{1}{2}}{31 \cdot \alpha + 1} \quad (\text{C.5})$$

To calculate  $\alpha$ , we need to know what surface area can be considered a step edge or a terrace. To resolve this conundrum, we refer to our results in chapter 3. In chapter 3, we reported low energy D<sub>2</sub> sticking probabilities for the curved Pt(1 1 1) crystal. The results were fitted with a linear function, where the offset quantified reactivity at the (1 1 1) surface. We

showed that the slope represents the reaction cross section for the  $D_2$  molecules impinging A- and B-type step edges. In chapter 4, we present a model that predicts HD formation as a function of step density. It assumes diffusive mixing at terraces and no diffusion at steps. We assume no exchange between the two different sites. Dissociation and HD exchange are governed by the relative abundance of step and terrace sites. Calculating the relative abundance of the terrace and step sites require the size of the step edge and the size of the unit cell. The latter can be calculated from the crystal position relative to the (1 1 1) surface. The first is determined from the reaction cross sections, by extrapolating our fits to reach unit sticking probability. Within error bars, extrapolated fits for A- and B-type steps closely resemble step densities for the (1 1 3) and (3 3 1) surface, respectively. These are surfaces that consist only of sites attributed to step edges and no terraces. Consequently, we describe the steps as {1 1 3} and {3 3 1} microfacets.

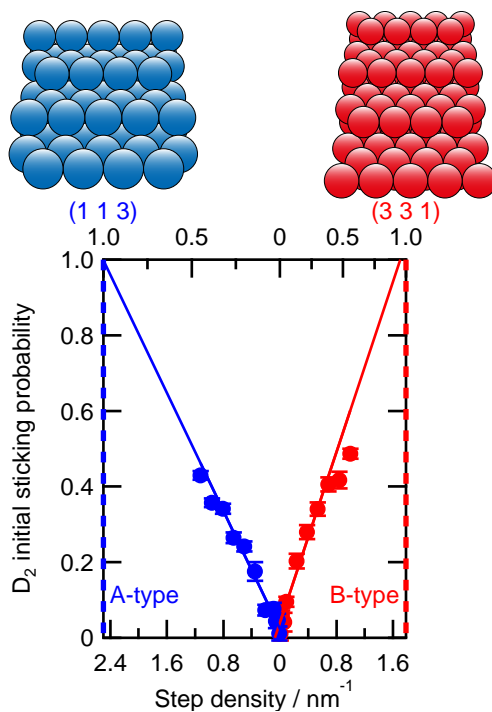


**Figure C.4:** Experimental fits from figure 3.2f extrapolated to  $(1\ 1\ 3)$  and  $(3\ 3\ 1)$ . The top axis represent  $(1-\alpha)$ , showing the surface fraction that contributes to steps.

Experiments were performed using Lionfish; an ultra-high vacuum (UHV) system with a base pressure lower than  $10^{-10}$  mbar. The system is equipped with a double differentially pumped supersonic molecular beam (SSB), a single differentially pumped effusive beam (EB), a fixed quadrupole mass spectrometer (QMS, Balzers QMA 200), and a quadrupole mass spectrometer (UTI-100C) that can be translated along the SSB axis for time of flight measurements.

### Forming the two molecular beams

The SSB is formed by expanding a constant flow (4 ml/min) of O<sub>2</sub> (Hoekloos, 5.0) from a tungsten nozzle with a 35  $\mu$ m orifice. The expansion is subsequently shaped by two skimmers and an orifice, resulting in a 3.6 mm diameter circular oxygen beam (see chapter 2). The SSB can be modulated with two inert stainless steel beam flags and a mechanical chopper. The first differentially pumped stage houses the mechanical chopper, which is used for both reducing the amount of O<sub>2</sub> by the 16% duty cycle and time of flight experiments. Figure D.1 shows the kinetic energy distribution of the O<sub>2</sub> beam, as determined from fits to experimental data. The first O<sub>2</sub> flag is controlled using Labview and resides in the second differentially pumped stage. The second O<sub>2</sub> flag is a stepper motor controlled beam flag with a 50% duty cycle placed inside the UHV system. These O<sub>2</sub> beam flags are used in conjunction with two EB flags to perform King and Wells[11] type reactivity experiments between two or more reactants.

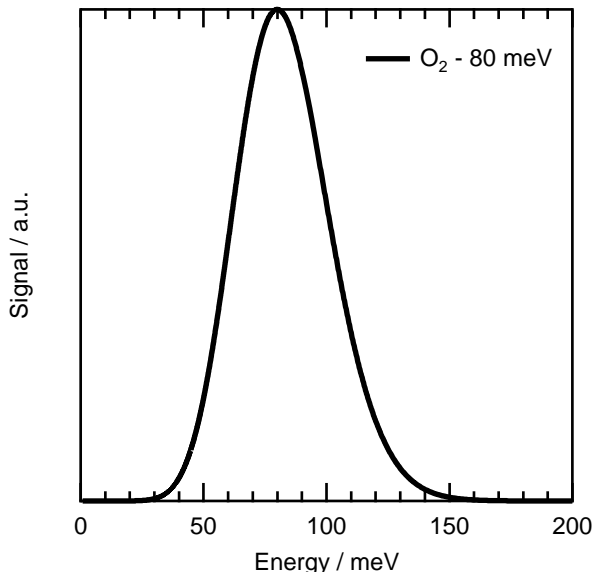


**Figure D.1:** Flux-weighted kinetic energy distribution of the  $\text{O}_2$  supersonic beam, as determined from fits to the time of flight. The most probable  $E_{kin}$  (FWHM) is 80 (44) meV.

The effusive beam is formed by expanding varying flows ( $0.8\text{--}9.6\text{ ml min}^{-1}$ ) of 1:1 mixed  $\text{H}_2\text{:D}_2$  from a 0.2 mm nozzle. The beam is shaped by a skimmer and an orifice. The resulting hydrogen beam is approximately 7.7 mm in diameter at the sample and can be blocked by two beam flags. The first hydrogen flag is a manual gate valve that separates the differentially pumped stage from the UHV. Upon opening this flag, an effusive hydrogen load from the differentially pumped stage enters the UHV chamber. The second beam flag is a beam block on a manual rotation stage. This flag either blocks the hydrogen beam or admits it directly into the main chamber and onto the sample.  $\text{H}_2\text{O}$  and  $\text{D}_2\text{O}$  are contaminants in the UHV and the beam. In combination with the long vacuum time constant of water, this makes it challenging to even qualitatively measure that water formation occurs at our Pt samples. To partially circumvent this, we instead use a 1:1 mixture of  $\text{H}_2$  and  $\text{D}_2$  in the effusive beam. While  $\text{HDO}$  is also a contaminant in the beam, it is small compared to  $\text{D}_2\text{O}$  and  $\text{H}_2\text{O}$ .



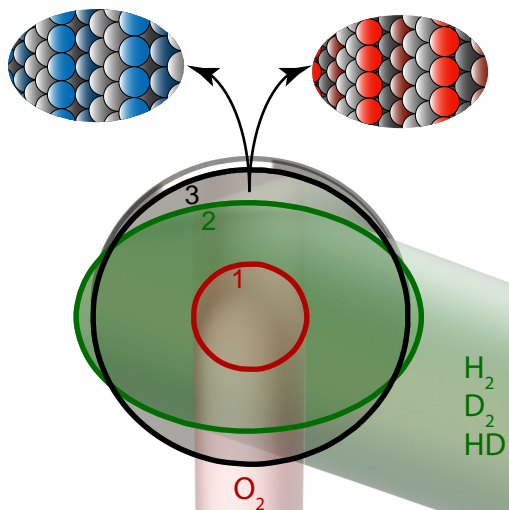


**Figure D.2:** Schematic overview of the experiment, where area 1 of the surface is pre-covered with the supersonic  $\text{O}_2$  beam (red), and the effusive  $\text{H}_2/\text{D}_2$  beam (green) subsequently reacts with the adsorbed oxygen. Experiments are performed on  $\text{Pt}(3\ 3\ 5)$  (left) and  $\text{Pt}(5\ 5\ 3)$  (right) surfaces at a surface temperature of 500 K.

since reactions in the background involving all three reactants -  $\text{O}_2$ ,  $\text{H}_2$ , and  $\text{D}_2$  - are less likely. The HDO signal shown here provides qualitative evidence of water formation.

## Design of experiment

Figure D.2 schematically shows the experiment. The two molecular beams cross at  $45^\circ$  at the single crystal surface. The  $\text{Pt}(3\ 3\ 5)$  and  $\text{Pt}(5\ 5\ 3)$  crystals are 10 mm in diameter and cut and polished to within  $0.1^\circ$ . The crystals are oriented in the vacuum at normal incidence to the  $\text{O}_2$  beam. The samples are cleaned by Ar sputtering (Messer, 5.0; 15 mA, 5 min.), oxidation (900 K, Messer, 5.0;  $3.5 \cdot 10^{-8}$  mbar, 3 min.), and *in vacuo* annealing (1200 K) cycles. After each experiment, the sample is flashed to 1200 K to remove any remaining oxygen from the sample. Throughout the experiments, the surface temperature is regulated to 500 K.

## Two typical experiments

Two typical experiments on Pt(3 3 5) are shown in figures D.3 and D.4. They are performed with excess hydrogen and excess oxygen, respectively. The four previously mentioned beam flags are manually operated at 30 s intervals. Panel a of figures D.3 and D.4 indicates the state of the oxygen and hydrogen flags. The effusive loads of the O<sub>2</sub> and hydrogen beams, resulting from the respective first flags, are shown as hatched red and hatched green backgrounds. The direct O<sub>2</sub> and hydrogen beams are depicted to scale in red and green respectively. The partial pressure of O<sub>2</sub>, HD, and HDO are measured using the fixed QMS and presented in panels c, d, and e respectively. O-coverages are shown in panel b for guidance in the surface reactions at play. We estimate the initial maximum O-coverage by integrating the O<sub>2</sub> dissociative sticking results on the clean surface from 60-90 s, fitting it with an exponential function, and assuming 0.25 monolayers is reached upon extrapolating to its asymptote. The O-coverages throughout the remainder of the experiment are approximated from the coverage-dependent O<sub>2</sub> sticking. In the following sections, we will now explain the experiments in full and indicate notable features in the data.

### 0 - 120 s – O<sub>2</sub> sticking

At the start of each experiment, all flags are closed and both molecular beams are contained to their respective differentially pumped stages. Background pressures for O<sub>2</sub>, HD, and HDO are measured for 30 s. First, oxygen is adsorbed to the surface in a standard King and Wells[11] type experiment. At 30 s, the first O<sub>2</sub> flag is retracted and the O<sub>2</sub> beam enters the main chamber. Upon entering the UHV, the O<sub>2</sub> beam scatters off the second O<sub>2</sub> flag and increases the background pressure. This is indicated in panel a with the red hatch. The second flag is retracted at 60 s. The O<sub>2</sub> beam directly impinges onto the sample, whereupon the O<sub>2</sub> partial pressure drops due to O<sub>2</sub> dissociative sticking. After covering the surface with O<sub>ads</sub>, the second flag is closed at 90 s. The O<sub>2</sub> background signal returns to its original value. The modulated O<sub>2</sub> beam is well-suited

for measuring time-dependent sticking and determining the initial sticking probability. These are extracted by normalizing the measured pressure to the initial background pressure ( $t = 30\text{-}60$  s), inverting, and subsequently signal-averaging with experiments performed under identical conditions. This yields the experimental results in figure 5.2.

## 120 - 210 s – Employing the $\text{H}_2/\text{D}_2$ beam

After (partially) covering the surface in oxygen (panel b) and measuring the background pressure for an additional 30 s, the effusive beam is employed at  $t = 120$  s to react hydrogen with  $\text{O}_{ads}$ . Three notable things happen. First, the hydrogen beam is still contained to the differentially pumped stage, as shown in panel a. However, an effusive hydrogen flux already enters the UHV, as depicted by the green hatch in panel a. As a consequence of this hydrogen flux, the HD pressure in panel d increases. Second, the HDO pressure in panel e increases. Third, the  $\text{O}_2$  pressure in panel c decreases. The effusive hydrogen flux reacts in the background, forming nascent HD and water. The background reaction with  $\text{O}_2$  causes a fractional decrease in the  $\text{O}_2$  QMS signal. As a consequence,  $\text{O}_2$  sticking probabilities need to be calculated using  $\text{O}_2$  background pressures measured under identical conditions, i.e. with the same hydrogen pressures.

In addition to background reactivity, the effusive hydrogen flux also reacts at the Pt surface. Throughout the experiment, the HD background pressure gradually increases. An additional increase in HD pressure is observed in excess hydrogen, exemplified by the inset at 157 s in figure D.3. The increase in HD pressure observed in the inset occurs earlier with increasing hydrogen flux. The HD pressure drops back to the initial level upon readsorbing  $\text{O}_2$  at 180 s. Experiments that reveal this HD drop, also exhibit an  $\text{O}_2$  sticking probability at 180 s that resembles the initial sticking probability for the clean surface. This shows that the  $\text{O}_{ads}$  was depleted in these experiments. In contrast, this increase in HD pressure is not observed for excess oxygen in figure D.4. The  $\text{O}_2$  sticking probability at 180 s is lower than  $S_0$  observed in figure 5.2, but higher than  $\text{O}_2$  sticking

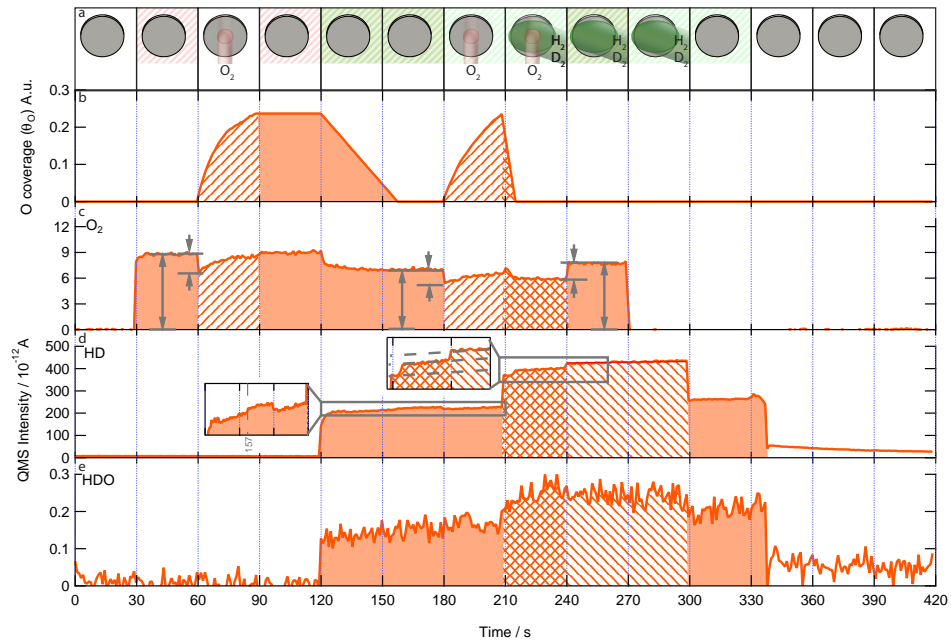


**Figure D.3:** Typical HDO formation experiment with excess hydrogen on Pt(3 3 5) at  $T_s = 500$  K.

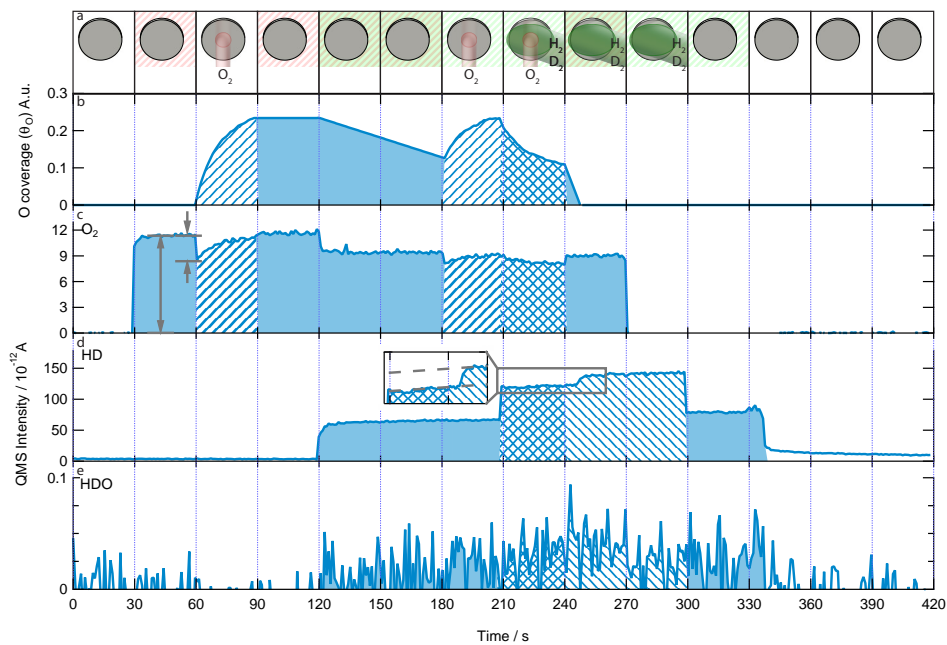


**Figure D.4:** Typical HDO formation experiment with limiting hydrogen on  $\text{Pt}(3\ 3\ 5)$  at  $T_s = 500$  K.

at 150 s. Therefore, the O-coverage has decreased, but  $O_{ads}$  is not fully depleted. Consequently, we can already qualitatively state that reaction 5.1 occurs in the presence of  $O_{ads}$  and hydrogen at the expense of reaction 5.2.

The  $O_2$  beam impinges onto the surface once more. The removed  $O_{ads}$  is replenished from 180 s until 210 s.  $O_2$  sticking results measured at this point in the experiment are discussed in more detail in appendix D.

### 210 s – Direct reaction of $O_2$ , $H_2$ , and $D_2$

At 210 s, the second hydrogen flag is retracted. In figure 5.3, this point in the experiment is defined as time = 0. As indicated by panel a in figures D.3 and D.4, the oxygen and hydrogen beams both directly impinge onto the surface from 210 s until 240 s. Consequential to the incident hydrogen beam, three notable things occur.

First, the  $O_2$  pressure in panel c increases upon impinging the hydrogen beam for high hydrogen fluxes, as shown in figure D.3, but remains the same for low hydrogen fluxes exemplified figure D.4. The  $O_2$  pressure increase appears to result from a change in background reactivity, as indicated by the higher  $O_2$  background pressure after 240 s than before 210 s in figure D.3.

Second, the HD pressure in panel d increases at 210 s due to reaction 5.2 from the hydrogen beam occurring in area 2 in figure D.2.

Third, the HDO pressure increases from two contributions. Additional HDO contamination enters the UHV chamber with the effusive beam or forms in the background. However, figure D.3 clearly shows a higher HDO pressure before 240 s than after. This qualitatively shows HDO forms at the Pt surface as a result of the  $O_2$  and hydrogen beams. From 240 s onward, all valves are sequentially closed with the expected behavior for the partial pressure of  $O_2$ , HD, and HDO.

## Analysis – HD deconvolution

At this point, we have given a full description of the different steps taken throughout the experiment. The most interesting features in the data are revealed by area 1 in figure D.2 — this is where  $\text{O}_2$  reacts with  $\text{H}_2$  and  $\text{D}_2$ . However, this is but a minor feature in the HD data. We now deconvolute the various contributions to the HD signal, so that we can extract reactivity in area 1 of figure D.2.

We start with the effusive flux that emerges from the effusive beam upon opening the EB1 gate valve at 120 s. Upon opening EB1, the EB2 beam flag remains closed until 210 s; i.e. the effusive beam does not yet enter the main chamber. The HD pressure increases significantly due to effusive load of  $\text{H}_2$ ,  $\text{D}_2$ , and HD from the differentially pumped stage. The various contributions to this HD signal are disentangled in figure D.5. This effusive load consists of at least four separate contributions: HD contamination in the beam, HD formed in the expansion, HD formed in the UHV from various catalytic surfaces e.g. filaments, and HD formed by the sample. We quantify the first three by replacing the catalytically-active Pt surface with an inactive Au(1 1 1) surface, shown in dark gray. These contributions generate approximately 1/3 of the HD signal.

A clue to the influence of area 1 in figure D.2 is revealed at 140 s in figure D.5 and 157 s in the previously mentioned inset in figure D.3. There, the HD signal increases by approximately 4.4 % of the total amount. This 4.4% increase in HD partial pressure is observed for all relatively high flux  $\text{H}_2/\text{D}_2$  beams on Pt(3 3 5). A similar increase is observed for Pt(5 5 3). Upon admitting oxygen to the sample at 180 s, the HD partial pressure instantaneously drops back to the initial pressure. This pressure drop is quantified and shown for both Pt(3 3 5) and Pt(5 5 3) in figure D.6. Additionally, the drop in HD appears independent of O-coverage. Three conclusions can be drawn from this behavior. First, dissociated hydrogen and deuterium are consumed by adsorbed oxygen, instead of forming HD. Second, the area covered by the oxygen beam is constant throughout the experiments.

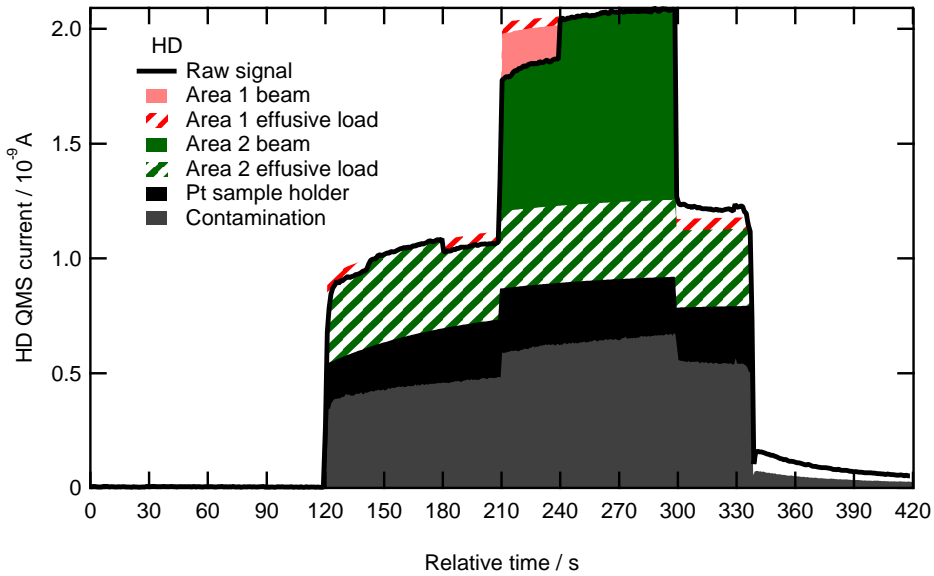


**Figure D.5:** The measured HD signal is convolved by various contributions that are generalized into contributions from the effusive load or the direct beam.

Third, the beam profile of the effusive beam is independent of flux. With these observations, HD produced by the sample can be disentangled by the following assumption: if (reactive) oxygen is present at the surface, adsorbed hydrogen reacts with oxygen to form water instead of recombinatively desorbing as HD.

This assumption first enables us to quantify the relative surface area of clean surface with respect to the O-covered surface — the sizes of which are independent of the oxygen or hydrogen flux. An effusive flux through an orifice should result in an isotropic hydrogen flux covering the entire sample and sample holder. Since the oxygen beam covers approximately 13% of the sample, the pressure drop is 13% (pink) of the total amount of HD produced by the sample (green) in figure D.5. This holds true for both the effusive flux (hatch) and direct beam (solid fill). A residual amount of HD is produced from a separate source not present in the Au(1 1 1)



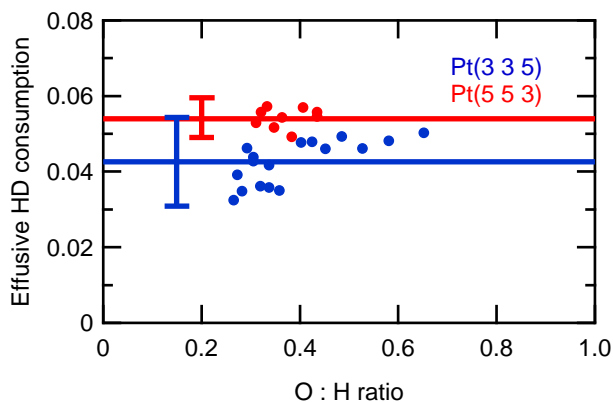


**Figure D.6:** Effusive HD pressure drop for different O:H ratios.

measurements (black) in figure D.5. This HD most likely forms on the side of sample or the Pt ribbon used to attach the sample to the sample holder.

### Analysis - Area 1 reactivity

After deconvoluting the HD signal, we fully attribute changes in the HD pressure after  $t = 210$  s to area 1 in figure D.2. For the hydrogen poor experiment in figure D.4, the HD pressure remains constant from 210 s until 245 s. In contrast, the hydrogen rich experiment in figure D.3 exhibits two HD pressure increases: at 215 s and 240 s. Here, the  $O_2$  sticking probability quickly approximates  $S_0$  in figure 5.2. We attribute the first observed pressure increase in figures D.3 and D.4 after 210 s to depletion of  $O_{ads}$ . Depletion of  $O_{ads}$  occurs while both molecular beams remain active for excess hydrogen in figure D.3 (see panel a). Consequently, a steady state sets in. There, all available  $O_{ads}$  from dissociative  $O_2$  sticking is consumed first in reaction 5.1. Any remaining hydrogen recombinatively desorbs according to reactions 5.2. At 240 s, the  $O_2$  beam stops directly impinging the sample and HD formation maximizes.

Figure D.7 presents an alternative view of figure 5.3. It includes the reaction probabilities before 210 s, i.e. before 0 s in figure 5.3. Panels a and b

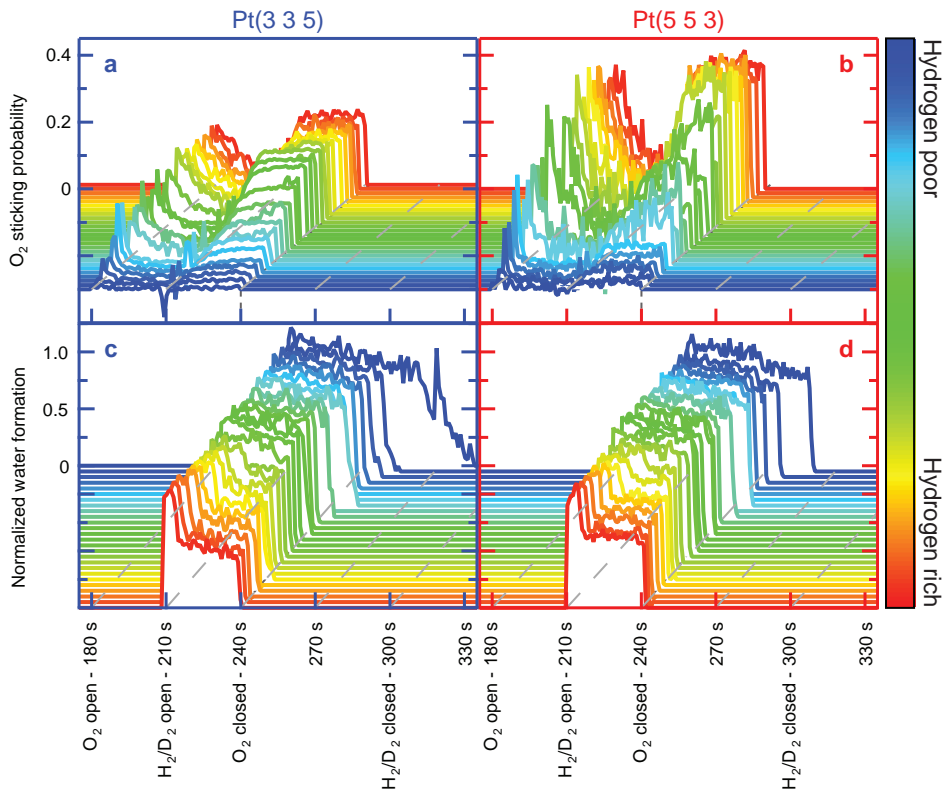


**Figure D.7:** Normalized water production, as measured from HD formation (see text), and O<sub>2</sub> consumption from the direct molecular beams in area 1 for Pt(3 3 5) (blue axes) and Pt(5 5 3) (red axes).

of figure D.7 show the O<sub>2</sub> sticking probability for Pt(3 3 5) and Pt(5 5 3) from 180 s onward, i.e. upon readmitting the O<sub>2</sub> beam. Two observations clearly point toward O<sub>ads</sub> consumption by a surface reaction from hydrogen present in the background. First, dissociative O<sub>2</sub> sticking is clearly higher for both surfaces at 180 s than at  $t = 30$  s in figure 5.2, showing that the O<sub>ads</sub> coverage has lowered between 30 and 180 s. Second, the initial O<sub>2</sub> sticking probability at 180 s in figure D.7 increases with hydrogen flux. It is noteworthy that the O<sub>2</sub> sticking probabilities measured at 180 s are higher for Pt(5 5 3) than Pt(3 3 5), despite higher O-coverage for Pt(5 5 3). These data show that the Pt(5 5 3) surface with B-type step edges is more reactive under these conditions, despite Pt(5 5 3) having lower step density

than Pt(3 3 5). ( $0.96 \text{ nm}^{-1}$  vs  $1.13 \text{ nm}^{-1}$ , respectively)

The  $O_{ads}$  coverage has replenished at 210 s after the  $O_2$  beam has impinged onto the sample for 30 s, as indicated by the low  $O_2$  sticking probabilities. The main results occur from 210 s onward and are elaborated on in chapter 5.

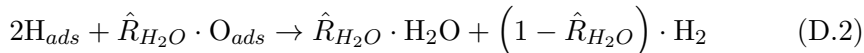
### Extracting the O:H surface ratio

Figure D.7 already presents a wealth of information. Figure 5.3 makes an even more quantitative comparison by also plotting reactivity against the ratio of the reactive fluxes. Here, we explain how we extract the reactive flux ratio from the data. We define the reactive fluxes as the respective molecular fluxes multiplied with their initial sticking probability:

$$\begin{aligned}\phi_O &= 2S_{0,O_2} \cdot \phi_{O_2} \\ \phi_H &= 2S_{0,H_2} \cdot \phi_{H_2} \\ \phi_D &= 2S_{0,D_2} \cdot \phi_{D_2}\end{aligned}\tag{D.1}$$

where  $\phi$  is the flux and  $S_{0,i}$  the sticking probability for molecule  $i$ . Absolute fluxes are challenging to extract, but the ratio of the reactive fluxes can be extracted directly from the data.

We have stated in chapter D that for the  $O_{ads}$  limited situation, a steady state situation sets in. In steady state,  $\hat{R}_{H_2O}$  is a direct measure of the ratio of reactive  $O_2$  and the  $H_2/D_2$  fluxes. If we disregard any isotope dependencies, we may write this limiting reagent problem as:



The  $O_2$  flow to the supersonic beam remains constant throughout the experiment. The  $O_2$  beam is attenuated by chopping the beam with the mechanical chopper so that lower O:H ratio's could be achieved. We vary the relative flux of the two beams by changing the  $H_2/D_2$  flow to the effusive beam using the flow controller. Chapter 2 showed that flux is proportional

to flow (and nozzle pressure) for the supersonic beam. We assume the same applies for the effusive beam, although scaling of flow and flux will differ compared to the supersonic molecular beam. Consequently, the flux ratio is proportional to the mass flow ratio applied by the flow controllers:

$$\dot{m}_{rel} = \frac{\dot{m}_{O_2}}{\dot{m}_{H_2} + \dot{m}_{D_2}} \propto \frac{\phi_{O_2}}{\phi_{D_2} + \phi_{H_2}} \quad (D.3)$$

where  $\dot{m}_i$  and  $\phi_i$  are the flow and flux of compound  $i$  respectively.  $\hat{R}_{H_2O}$  requires including the reaction probabilities. Under  $O_{ads}$  limited steady state conditions, the O-coverage is low and reaction probabilities resemble that of the clean surface. Under these conditions, the relative molecular fluxes scale with the relative reactive fluxes:

$$\frac{\phi_{O_2}}{\phi_{D_2} + \phi_{H_2}} \propto \frac{S_{0,O_2}\phi_{O_2}}{S_{0,D_2}\phi_{D_2} + S_{0,H_2}\phi_{H_2}} \quad (D.4)$$

Figure D.8 compares the  $\hat{R}_{H_2O}$  with the relative flow,  $\dot{m}_{rel}$ , and confirms our premise that  $\hat{R}_{H_2O}$  in steady state is proportional to the relative oxygen flow. While the measured  $\hat{R}_{H_2O}$  cannot exceed 1, the actual O:H ratio can. We use least squares fitting for the **Pt(3 3 5)** and **Pt(5 5 3)** data in figure D.8. Subsequently, we extract the scaling between  $\hat{R}_{H_2O}$  and the relative flow under the  $O_{ads}$  limited steady state condition, i.e. where  $O_2$  sticking is constant. We then extrapolate the fit to excess  $O_2$  data, where  $\theta_O$  exceeds 0, to allow us to quantify the relative fluxes shown by equation D.4. We emphasize here that higher  $O_2$  sticking for **Pt(5 5 3)** than **Pt(3 3 5)** is incorporated in the O:H ratio; the slope for **Pt(5 5 3)** exceeds that of **Pt(3 3 5)** in figure D.8.

### Additional evidence of increased hydrogen reactivity

While we measure  $O_2$  sticking directly, we did not do the same for hydrogen or deuterium. We disregard isotope effects in the following discussion. However, the slopes presented in figure D.8 provide clues to the reactivity differences. As shown by equation D.4, the slopes in figure D.8 are a direct consequence of the  $O_2$  reactive flux and the  $H_2$  and  $D_2$  reactive fluxes. If we assume the molecular fluxes are identical for the two experiments, then any

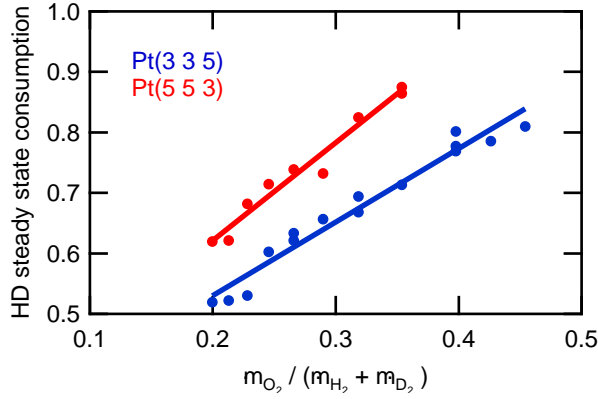


**Figure D.8:** HD consumption at steady state.

difference in slope in figure D.8 is a consequence of the sticking probabilities. With 0.35 compared to 0.25, the initial  $O_2$  sticking probability for **Pt(5 5 3)** exceeds that of **Pt(3 3 5)**.

An interesting observation may be made here: the ratio of the slopes in figure D.8 is lower than the  $O_2$   $S_0$  ratio, with 1.33 compared to 1.4. Error bars may be partially responsible for the difference. If we ignore error bars, this also suggests that hydrogen is more reactive at **Pt(5 5 3)** than **Pt(3 3 5)** under these conditions. We explain our reasoning.

The slopes are described by the right hand side of equation D.4. The ratio of the two slopes then represent:

$$\frac{\left( \frac{S_{0,O_2}^{5\ 5\ 3} \phi_{O_2}}{S_{0,D_2}^{5\ 5\ 3} \phi_{D_2} + S_{0,H_2}^{5\ 5\ 3} \phi_{H_2}} \right)}{\left( \frac{S_{0,O_2}^{3\ 3\ 5} \phi_{O_2}}{S_{0,D_2}^{3\ 3\ 5} \phi_{D_2} + S_{0,H_2}^{3\ 3\ 5} \phi_{H_2}} \right)} = 1.33 \quad (D.5)$$

The relative flows, and hence the molecular fluxes, used in the experiment are identical. If we simplify the equation and assume no isotope dependence

for  $S_0$  for  $H_2$ :

$$\frac{\left(\frac{S_{0,O_2}^{5\ 5\ 3}}{S_{0,H_2}^{5\ 5\ 3}}\right)}{\left(\frac{S_{0,O_2}^{3\ 3\ 5}}{S_{0,H_2}^{3\ 3\ 5}}\right)} = 1.33 \quad (D.6)$$

From the data in figure 5.2, we extracted  $S_0$  for the **A-** and **B-type** surfaces of 0.25 and 0.35. respectively. Substitution and isolation of the hydrogen reactivity yields:

$$\frac{S_{0,H_2}^{3\ 3\ 5}}{S_{0,H_2}^{5\ 5\ 3}} = \frac{S_{0,O_2}^{5\ 5\ 3}}{S_{0,O_2}^{3\ 3\ 5}} \cdot 1.33 = 0.95 \quad (D.7)$$

These results suggest that **Pt(5 5 3)** is 5% more reactive for hydrogen dissociation. Higher reactivity for **Pt(5 5 3)** than **Pt(3 3 5)** qualitatively agrees with our previous results on  $D_2$  dissociation. However, the results presented here assumes that the  $O_2$  flux was equal for both experiments. The experiments for **Pt(3 3 5)** and **Pt(5 5 3)** were measured 7 months apart. While the same  $O_2$  flow was applied to the nozzle during the experiments, the nozzle pressure increased from the **Pt(5 5 3)** experiments to the **Pt(3 3 5)** experiments. We do not believe the flux was affected, but cannot completely rule it out either. The O:H ratio is unaffected as these are calculated from the separate data sets. Similarity of the data suggests that the absolute fluxes were similar.

---

## Bibliography

---

- [1] Davy, H. *Philos. Trans. R. Soc.* **107**, 77–85 (1817).
- [2] Berzelius, J. J. *Ann. Chim. Phys.* **61**, 146–151 (1836).
- [3] Henry, W. *Philos. Trans. R. Soc.* **114**, 266–289 (1824).
- [4] Brønsted, J. N. and Pedersen, K. *Z. Phys. Chem. Stoechiom. Verwandtschaftsl.* **108**(185) (1924).
- [5] Langmuir, I. *Nobel Lectures* (1932).
- [6] Davisson, C. J. and Germer, L. H. *Proc. Natl. Acad. Sci. U.S.A.* **14**, 317–322 (1928).
- [7] de Broglie, L. *Recherches sur la théorie des quanta*. PhD thesis, Université Paris-Sorbonne, (1924).
- [8] Davisson, C. and Germer, L. H. *Phys. Rev.* **30**, 705–740 (1927).
- [9] Davisson, C. *Nobel Lectures* (1937).
- [10] Stern, O. *Nobel Lectures* (1946).
- [11] King, D. A. and Wells, M. G. *Surf. Sci.* **29**, 454–482 (1972).
- [12] Auerbach, D. J., Pfnür, H. E., Rettner, C. T., Schlaegel, J. E., Lee, J., and Madix, R. J. *J. Chem. Phys.* **81**, 2515–2516 (1984).
- [13] D’evelyn, M. P., Hamza, A. V., Gdowski, G. E., and Madix, R. J. *Surf. Sci.* **167**, 451–473 (1986).

- [14] Luntz, A. C., Williams, M. D., and Bethune, D. S. *J. Chem. Phys.* **89**, 4381–4395 (1988).
- [15] Lee, M. B., Yang, Q. Y., Tang, S. L., and Ceyer, S. T. *J. Chem. Phys.* **85**, 1693–1694 (1986).
- [16] Rettner, C. T., Pfnür, H. E., and Auerbach, D. J. *Phys. Rev. Lett.* **54**, 2716–2719 (1985).
- [17] Rettner, C. T., Pfnür, H. E., and Auerbach, D. J. *J. Chem. Phys.* **84**, 4163–4167 (1986).
- [18] Luntz, A. C., Brown, J. K., and Williams, M. D. *J. Chem. Phys.* **93**, 5240–5246 (1990).
- [19] Gostein, M., Parhikhteh, H., and Sitz, G. O. *Phys. Rev. Lett.* **75**, 342–345 (1995).
- [20] Juurlink, L. B. F., McCabe, P. R., Smith, R. R., DiCologero, C. L., and Utz, A. L. *Phys. Rev. Lett.* **83**, 868–871 (1999).
- [21] Hundt, P. M., Jiang, B., van Reijzen, M. E., Guo, H., and Beck, R. D. *Science* **344**(6183), 504–507 (2014).
- [22] Juurlink, L. B. F., Killelea, D. R., and Utz, A. L. *Prog. Surf. Sci.* **84**, 69–134 (2009).
- [23] Beck, R. D., Maroni, P., Papageorgopoulos, D. C., Dang, T. T., Schmid, M. P., and Rizzo, T. R. *Science* **302**(5642), 98–100 (2003).
- [24] Killelea, D. R., Campbell, V. L., Shuman, N. S., and Utz, A. L. *Science* **319**, 790–793 (2008).
- [25] Kurahashi, M. and Yamauchi, Y. *Phys. Rev. B* **85**, 161302 (2012).
- [26] Ueta, H. and Kurahashi, M. *Angew. Chem. Int. Ed.* **56**, 4174–4177 (2017).
- [27] Cao, K., van Lent, R., Kleyn, A. W., Kurahashi, M., and Juurlink, L. B. F. *Proc. Natl. Acad. Sci. U.S.A.* **116**, 13862–13866 (2019).



- 
- [28] Somorjai, G. A. *Catal. Lett.* **7**(1-4), 169 (1990).
- [29] Vattuone, L., Savio, L., and Rocca, M. *Surf. Sci. Rep.* **63**, 101–168 (2008).
- [30] Hahn, C., Shan, J., Liu, Y., Berg, O., Kleyn, A. W., and Juurlink, L. B. F. *J. Chem. Phys.* **136**, 114201 (2012).
- [31] Vesper, G., Thiel, P. A., and Imbihl, R. *J. Phys. Chem.* **98**, 2148–2151 (1994).
- [32] Sander, M., Imbihl, R., and Ertl, G. *J. Chem. Phys.* **97**, 5193–5204 (1992).
- [33] Lawton, T. J., Pushkarev, V., Wei, D., Lucci, F. R., Sholl, D. S., Gellman, A. J., and Sykes, E. C. H. *J. Phys. Chem. C* **117**, 22290–22297 (2013).
- [34] Gellman, A. J., Tysoe, W. T., and Zaera, F. *Catal. Lett.* **145**, 220–232 (2015).
- [35] Mom, R. V., Hahn, C., Jacobse, L., and Juurlink, L. B. F. *Surf. Sci.* **613**, 15–20 (2013).
- [36] Walter, A. L., Schiller, F., Corso, M., Merte, L. R., Bertram, F., Lobo-Checa, J., Shipilin, M., Gustafson, J., Lundgren, E., Brión-Ríos, A. X., Cabrera-Sanfeliix, P., Sánchez-Portal, D., and Ortega, J. E. *Nat. Commun.* **6**, 8903 (2015).
- [37] Janlamool, J., Bashlakov, D., Berg, O., Praserthdam, P., Jongsomjit, B., and Juurlink, L. B. F. *Molecules* **19**, 10845–10862 (2014).
- [38] Arulmozhi, N., Esau, D., Lamsal, R. P., Beauchemin, D., and Jerkiewicz, G. *ACS Catal.* **8**, 6426–6439 (2018).
- [39] Besocke, K., Krahel-Urban, B., and Wagner, H. *Surf. Sci.* **68**, 39–46 (1977).
- [40] Liu, H. T., Armitage, A. F., and Woodruff, D. P. *Surf. Sci.* **114**, 431–444 (1982).

- [41] Armitage, A. F., Liu, H. T., and Woodruff, D. P. *Vacuum* **31**, 519–522 (1981).
- [42] Corso, M., Schiller, F., Fernández, L., Cordón, J., and Ortega, J. E. *J. Phys. Condens. Matter* **21**(35), 353001 (2009).
- [43] De Alwis, A., Holsclaw, B., Pushkarev, V. V., Reinicker, A., Lawton, T. J., Blecher, M. E., Sykes, E. C. H., and Gellman, A. J. *Surf. Sci.* **608**, 80–87 (2013).
- [44] Ortega, J. E., Corso, M., Abd-el Fattah, Z. M., Goiri, E. A., and Schiller, F. *Phys. Rev. B* **83**, 085411 (2011).
- [45] Blomberg, S., Zetterberg, J., Zhou, J., Merte, L. R., Gustafson, J., Shipilin, M., Trincherro, A., Miccio, L. A., Magaña, A., Ilyn, M., Schiller, F., Ortega, J. E., Bertram, F., Grönbeck, H., and Lundgren, E. *ACS Catal.* **7**, 110–114 (2017).
- [46] Füchsel, G., Cao, K., Er, S., Smeets, E. W. F., Kleyn, A. W., Juurlink, L. B. F., and Kroes, G. J. *J. Phys. Chem. Lett.* **9**, 170–175 (2018).
- [47] Neugebahren, J., Borodin, D., Hahn, H. W., Altschäffel, J., Kandratzenka, A., Auerbach, D. J., Campbell, C. T., Schwarzer, D., Harding, D. J., Wodtke, A. M., and Kitsopoulos, T. N. *Nature* **558**, 280–283 (2018).
- [48] Chadwick, H., Guo, H., Gutiérrez-González, A., Menzel, J. P., Jackson, B., and Beck, R. D. *J. Chem. Phys.* **148**, 014701 (2018).
- [49] Bernasek, S. L., Siekhaus, W. J., and Somorjai, G. A. *Phys. Rev. Lett.* **30**, 1202–1204 (1973).
- [50] Lang, B., Joyner, R. W., and Somorjai, G. A. *Surf. Sci.* **30**, 440–453 (1972).
- [51] van der Niet, M. J. T. C., den Dunnen, A., Juurlink, L. B. F., and Koper, M. T. M. *J. Chem. Phys.* **132**, 174705 (2010).

- 
- [52] Weisstein, E. W. <http://mathworld.wolfram.com/Circle-CircleIntersection.html>. Accessed: 2019-09-05.
- [53] Cao, K. *Structure dependence of molecular reactions on surfaces*. PhD thesis, Leiden University, (2018).
- [54] Auerbach, D. J. In *Atomic Molecular Beam Methods*, Scoles, G., editor, chapter 14, 362–379. Oxford Univ. Press, Oxford (1988).
- [55] Haberland, H., Buck, U., and Tolle, M. *Review of Scientific Instruments* **56**, 1712–1716 (1985).
- [56] Groot, I. M. N. *The fight for a reactive site*. PhD thesis, Leiden University, (2009).
- [57] Gergen, B., Nienhaus, H., Weinberg, W. H., and McFarland, E. W. *Science* **294**, 2521–2523 (2001).
- [58] Meyer, J. and Reuter, K. *Angew. Chemie Int. Ed.* **53**, 4721–4724 (2014).
- [59] Kroes, G. J. *Science* **321**(5890), 794–797 (2008).
- [60] Diaz, C., Pijper, E., Olsen, R. A., Busnogo, H. F., Auerbach, D. J., and Kroes, G. J. *Science* **326**, 832–834 (2009).
- [61] Poelsema, B., Lenz, K., and Comsa, G. *J. Phys. Condens. Matter* **30**(22), 304006 (2010).
- [62] Poelsema, B., Lenz, K., and Comsa, G. *J. Chem. Phys.* **134**, 074703 (2011).
- [63] Cowin, J. P., Yu, C. F., Sibener, S. J., and Wharton, L. *J. Chem. Phys.* **79**, 3537–3549 (1983).
- [64] Sanz, A. S. and Miret-Artés, S. *Phys. Rep.* **451**, 37–154 (2007).
- [65] McCormack, D. A., Olsen, R. A., and Baerends, E. J. *J. Chem. Phys.* **122**(19), 194708 (2005).

- [66] Gee, A. T., Hayden, B. E., Mormiche, C., and Nunney, T. S. *J. Chem. Phys.* **112**, 7660–7668 (2000).
- [67] Salmeron, M., Gale, R. J., and Somorjai, G. A. *J. Chem. Phys.* **67**, 5324–5334 (1977).
- [68] Groot, I. M. N., Schouten, K. J. P., Kleyn, A. W., and Juurlink, L. B. F. *J. Chem. Phys.* **129**, 224707 (2008).
- [69] Groot, I. M. N., Kleyn, A. W., and Juurlink, L. B. F. *Angew. Chemie Int. Ed.* **50**, 5174–5177 (2011).
- [70] Groot, I. M. N., Kleyn, A. W., and Juurlink, L. B. F. *J. Phys. Chem. C* **117**, 9266–9274 (2013).
- [71] Walsh, A. J., van Lent, R., Auras, S. V., Gleeson, M. A., Berg, O. T., and Juurlink, L. B. F. *J. Vac. Sci. Technol. A Vacuum, Surfaces, Film.* **35**(3), 03E102 (2017).
- [72] Samson, P., Nesbitt, A., Koel, B. E., and Hodgson, A. *J. Chem. Phys.* **109**, 3255–3264 (1998).
- [73] Nour Ghassemi, E., Wijzenbroek, M., Somers, M. F., and Kroes, G. J. *Chem. Phys. Lett.* **683**, 329–335 (2017).
- [74] Cao, K., van Lent, R., Kleyn, A. W., and Juurlink, L. B. F. *Chem. Phys. Lett.* **706**, 680–683 (2018).
- [75] Luppi, M., McCormack, D. A., Olsen, R. A., and Baerends, E. J. *J. Chem. Phys.* **123**(16), 164702 (2005).
- [76] Lu, K. E. and Rye, R. R. *Surf. Sci.* **45**, 677–695 (1974).
- [77] Christmann, K., Ertl, G., and Pignet, T. *Surf. Sci.* **54**, 365–392 (1976).
- [78] Salmeron, M., Gale, R. J., and Somorjai, G. A. *J. Chem. Phys.* **70**(6), 2807 (1979).

- 
- [79] van Lent, R., Auras, S. V., Cao, K., Walsh, A. J., Gleeson, M. A., and Juurlink, L. B. F. *Science* **363**(6423), 155–157 (2019).
- [80] Christmann, K. and Ertl, G. *Surf. Sci.* **60**, 365–384 (1976).
- [81] Graham, A. P., Menzel, A., and Toennies, J. P. *J. Chem. Phys.* **111**, 1676–1685 (1999).
- [82] Kristinsdóttir, L. and Skúlason, E. *Surf. Sci.* **606**, 1400–1404 (2012).
- [83] Olsen, R. A., Kroes, G. J., and Baerends, E. J. *J. Chem. Phys.* **111**, 11155–11163 (1999).
- [84] Jardine, A. P., Lee, E. Y. M., Ward, D. J., Alexandrowicz, G., Hedge-land, H., Allison, W., Ellis, J., and Pollak, E. *Phys. Rev. Lett.* **105**, 136101 (2010).
- [85] Bădescu, Ș. C., Salo, P., Ala-Nissila, T., Ying, S. C., Jacobi, K., Wang, Y., Bedürftig, K., and Ertl, G. *Phys. Rev. Lett.* **88**, 136101 (2002).
- [86] Zheng, C. Z., Yeung, C. K., Loy, M. M. T., and Xiao, X. *Phys. Rev. B* **70**, 205402 (2004).
- [87] Zheng, C. Z., Yeung, C. K., Loy, M. M. T., and Xiao, X. *Phys. Rev. Lett.* **97**, 166101 (2006).
- [88] Olsen, R. A., Bădescu, Ș. C., Ying, S. C., and Baerends, E. J. *J. Chem. Phys.* **120**, 11852–11863 (2004).
- [89] Hahn, E., Schief, H., Marsico, V., Fricke, A., and Kern, K. *Phys. Rev. Lett.* **72**, 3378–3381 (1994).
- [90] den Dunnen, A. *Surface-structure dependencies in catalytic reactions*. PhD thesis, Leiden University, (2015).
- [91] Comsa, G., Mechttersheimer, G., and Poelsema, B. *Surf. Sci.* **97**(1), L297 – L303 (1980).

- [92] Balmes, O., Prevot, G., Torrelles, X., Lundgren, E., and Ferrer, S. *ACS Catal.* **6**(2), 1285–1291 (2016).
- [93] Calle-Vallejo, F., Loffreda, D., Koper, M. T. M., and Sautet, P. *Nat. Chem.* **7**, 403–410 (2015).
- [94] Calle-Vallejo, F., Tymoczko, J., Colic, V., Vu, Q. H., Pohl, M. D., Morgenstern, K., Loffreda, D., Sautet, P., Schuhmann, W., and Bandarenka, A. S. *Science* **350**, 185–189 (2015).
- [95] Stephens, I. E. L., Bondarenko, A. S., Grønbjerg, U., Rossmeisl, J., and Chorkendorff, I. *Energy Environ. Sci.* **5**, 6744–6762 (2012).
- [96] Ertl, G. *Angew. Chem. Int. Ed.* **47**(19), 3524–3535 (2008).
- [97] Nørskov, J. K., Bligaard, T., Logadottir, A., Bahn, S., Hansen, L. B., Bollinger, M., Bengaard, H., Hammer, B., Sljivancanin, Z., Mavrikakis, M., Xu, Y., Dahl, S., and Jacobsen, C. J. H. *J. Catal.* **209**(2), 275–278 (2002).
- [98] Verheij, L. K. and Hugenschmidt, M. B. *Surf. Sci.* **416**(1-2), 37–58 (1998).
- [99] Michely, T. and Comsa, G. *Surf. Sci.* **256**, 217 – 226 (1991).
- [100] Bondü, C. J., Calle-Vallejo, F., Figueiredo, M. C., and Koper, M. T. M. *Nat. Catal.* **2**, 243–250 (2019).
- [101] Gee, A. T. and Hayden, B. E. *J. Chem. Phys.* **113**, 10333–10343 (2000).
- [102] Jacobse, L., den Dunnen, A., and Juurlink, L. B. F. *J. Chem. Phys.* **143**, 014703 (2015).
- [103] van der Niet, M. J. T. C., den Dunnen, A., Juurlink, L. B. F., and Koper, M. T. M. *Angew. Chem. Int. Ed.* **49**(37), 6572–6575 (2010).
- [104] Verheij, L. K., Hugenschmidt, M. B., Poelsema, B., and Comsa, G. *Surf. Sci.* **233**, 209–222 (1990).

- 
- [105] Gee, A. T., Hayden, B. E., Mormiche, C., and Nunney, T. S. *Surf. Sci.* **512**(3), 165–172 (2002).
- [106] Honkala, K., Hellman, A., Remediakis, I. N., Logadottir, A., Carlsson, A., Dahl, S., Christensen, C. H., and Nørskov, J. K. *Science* **307**, 555–558 (2005).
- [107] Behrens, M., Studt, F., Kasatkin, I., Kühl, S., Hävecker, M., Abild-Pedersen, F., Zander, S., Girgsdies, F., Kurr, P., Knief, B.-L., Tovar, M., Fischer, R. W., Nørskov, J. K., and Schlögl. *Science* **336**(6083), 893–897 (2012).
- [108] Hoffmann, F. M. *Surf. Sci. Rep.* **3**, 107–192 (1983).
- [109] Chabal, Y. J. *Surf. Sci. Rep.* **8**(5-7), 211–357 (1988).
- [110] Greenler, R. G. *J. Chem. Phys.* **50**, 1963 (1969).
- [111] Greenler, R. G. *J. Chem. Phys.* **44**(1), 310–315 (1966).
- [112] Suzaki, Y. and Tachibana, A. *Appl. Opt.* **14**, 2809–2810 (1975).
- [113] Ertl, G. *Reactions at solid surfaces*, volume 14. John Wiley & Sons, (2010).
- [114] McEwen, J.-S., Payne, S. H., Kreuzer, H. J., Kinne, M., Denecke, R., and Steinrück, H.-P. *Surf. Sci.* **545**, 47–69 (2003).
- [115] Steininger, H., Lehwald, S., and Ibach, H. *Surf. Sci.* **123**(2-3), 264–282 (1982).
- [116] Baro, A. M. and Ibach, H. *J. Chem. Phys.* **71**, 4812 (1979).
- [117] Ogletree, D. F., Van Hove, M. A., and Somorjai, G. A. *Surf. Sci.* **173**, 351–365 (1986).
- [118] Ertl, G., Neumann, M., and Streit, K. M. *Surf. Sci.* **64**(2), 393–410 (1977).
- [119] Yang, H. J., Minato, T., Kawai, M., and Kim, Y. *J. Phys. Chem. C* **117**, 16429–16437 (2013).

- [120] Ryberg, R. *Phys. Rev. B* **40**(1), 865 (1989).
- [121] Malik, I. J. and Trenary, M. *Surf. Sci. Lett.* **214**, L237–L245 (1989).
- [122] Xu, J. and Yates, J. T. *Surf. Sci.* **327**, 193–201 (1995).
- [123] Mukerji, R. J., Bolina, A. S., and Brown, W. A. *Surf. Sci.* **527**, 198–208 (2003).
- [124] Tränkenschuh, B., Fritsche, N., Fuhrmann, T., Papp, C., Zhu, J. F., Denecke, R., and Steinrück, H.-P. *J. Chem. Phys.* **124**(7), 074712 (2006).
- [125] Tränkenschuh, B., Papp, C., Fuhrmann, T., Denecke, R., and Steinrück, H.-P. *Surf. Sci.* **601**, 1108–1117 (2007).
- [126] Shimizu, S., Noritake, H., Koitaya, T., Mukai, K., Yoshimoto, S., and Yoshinobu, J. *Surf. Sci.* **608**, 220–225 (2013).
- [127] van Hove, M. A. and Somorjai, G. A. *Surf. Sci.* **92**, 489 (1980).
- [128] Yoshinobu, J., Tsukahara, N., Yasui, F., Mukai, K., and Yamashita, Y. *Phys. Rev. Lett.* **90**, 248301 (2003).
- [129] Blyholder, G. *J. Phys. Chem.* **68**(10), 2772–2777 (1964).
- [130] Crossley, A. and King, D. A. *Surf. Sci.* **68**, 528–538 (1977).
- [131] Horn, K. and Pritchard, J. *J. Phys. Colloq.* **38**(C4), 164–171 (1977).
- [132] Hollins, P. *Surf. Sci. Rep.* **16**, 51–94 (1992).
- [133] Froitzheim, H., Hopster, H., Ibach, H., and Lehwald, S. *Appl. Phys.* **13**, 147–151 (1977).
- [134] Herzberg, G. *Molecular spectra and molecular structure, vol II*. Van Nostrand Reinhold Company, (1945).
- [135] Nagaoka, S. I., Teramae, H., and Nagashima, U. *J. Chem. Educ.* **90**, 669–670 (2013).



- 
- [136] Yoder, B. L. *Steric Effects in the Chemisorption of Vibrationally Excited Methane on Nickel*. PhD thesis, L'Ecole Polytechnique Fédérale de Lausanne, (2012).
- [137] Rothman, L. S., Gordon, I. E., Barbe, A., Benner, D. C., Bernath, P. F., Birk, M., Boudon, V., Brown, L. R., Campargue, A., Champion, J. P., Chance, K., Coudert, L. H., Dana, V., Devi, V. M., Fally, S., Flaud, J. M., Gamache, R. R., Goldman, A., Jacquemart, D., Kleiner, I., Lacome, N., Lafferty, W. J., Mandin, J. Y., Massie, S. T., Mikhailenko, S. N., Miller, C. E., Moazzen-Ahmadi, N., Naumenko, O. V., Nikitin, A. V., Orphal, J., Perevalov, V. I., Perrin, A., Predoi-Cross, A., Rinsland, C. P., Rotger, M., Šimečková, M., Smith, M. A., Sung, K., Tashkun, S. A., Tennyson, J., Toth, R. A., Vandaele, A. C., and Vander Auwera, J. *J. Quant. Spectrosc. Ra.* **110**(9-10), 533–572 (2009).
- [138] Demtröder, W. *Laser Spectroscopy: Basic Concepts and Instrumentation*. Springer-Verslag, (1981).
- [139] Bennett, W. R. *Phys. Rev.* **126**, 580–593 (1962).
- [140] Lamb, W. E. *Phys. Rev.* **134**, A1429–A1450 (1964).
- [141] Chadwick, H., Hundt, P. M., van Reijzen, M. E., Yoder, B. L., and Beck, R. D. *J. Chem. Phys.* **140**, 034321 (2014).
- [142] Juurlink, L. B. F. *Eigenstate-resolved measurements of methane dissociation on Ni(100)*. PhD thesis, Tufts University, (2000).
- [143] Miller, R. E. *Rev. Sci. Instrum.* **53**, 1719–1723 (1982).
- [144] Ebbing, D. D. and Gammon, S. D. *General Chemistry*. Houghton Mifflin Company, 9 edition, (2009).



### **Chapter 3**

Site-specific reactivity of molecules with surface defects – the case of H<sub>2</sub> dissociation on Pt

R. van Lent, S. V. Auras, K. Cao, A. J. Walsh, M. A. Gleeson, L. B. F. Juurlink *Science* **363**(6423) 155-157 (2019)

- Gekromd vlak zet zaken recht  
A. Dijkgraaf *C2W* **4** (2019)
- Een fundamentele controverse beslecht  
L.B.F. Juurlink *Nederlands Tijdschrift voor Natuurkunde* **85**(3) (2019)
- Chemists solve persistent problem after four decades  
B. Benda *Universiteit Leiden FWN nieuwsbrief* **11**(1) (2019)
- Leidse onderzoekers ontrafelen reacties met waterstof  
R. Canrinus-Moezelaar *NEMO Kennislink* January 2019
- Highlight DIFFER: hardnekkig katalysator-probleem na 40 jaar opgelost  
M. Vianen *Inside NWO-I nieuwsbrief* (2) (2019)

### **Chapter 4:**

Two-faced step edges in HD exchange on Pt

R. van Lent, K. Cao, S. V. Auras, A. J. Walsh, M. A. Gleeson, L. B. F. Juurlink *To be submitted*

---

## Chapter 5:

Step type dependence of oxygen reduction on Pt(1 1 1) surfaces

R. van Lent, A. den Dunnen, S. V. Auras, A. J. Walsh, M. A. Gleeson, L. B. F. Juurlink *To be submitted*

## Chapter 6:

Step-type and step-density influences on CO adsorption probed by reflection absorption infrared spectroscopy using a curved Pt(1 1 1) surface

A. J. Walsh, R. van Lent, S. V. Auras, M. A. Gleeson, O. T. Berg, L. B. F. Juurlink *J. Vac. Sci. Tech. A* **35**,(3) 03E102 (2017)

## Other publications:

A molecular beam study of D<sub>2</sub> dissociation on Pt(1 1 1): Testing SRP-DFT calculations

K. Cao, R. van Lent, A. W. Kleyn, L. B. F. Juurlink *Chem. Phys. Lett.* **706** 680-683 (2018)

Steps on Pt stereodynamically filter sticking of O<sub>2</sub>

K. Cao, R. van Lent, A. W. Kleyn, M. Kurahashi, L. B. F. Juurlink *Proc. Natl. Acad. Sci. USA* **116**(28) 13862-13886 (2019)

It's not just the defects – a curved crystal study of H<sub>2</sub>O desorption from Ag

S. V. Auras, R. A. B. van Bree, D. L. Bashlakov, R. van Lent, L. B. F. Juurlink *Phys. Chem. Chem. Phys.* **21**(28) 15422-15430 (2019)

Heterogeneous Catalytic Oxidation of Ammonia by Various Transition Metals

P. C. M. Laan, M. C. Franke, R. van Lent, L. B. F. Juurlink *J. Chem. Educ.* **96**(10) 2266-2270 (2019)

Richard van Lent was born in Gorinchem, the Netherlands, on March 28 1986 and grew up in Arkel. He obtained his HAVO diploma from Merewade College in Gorinchem in 2004. He found his passion in 2006 when he started studying Chemistry at the University of Applied Sciences in Rotterdam. After obtaining his propaedeutic diploma in 2007, he started the joint BSc program between Leiden University and Delft University of Technology: Molecular Science and Technology. He choose both a major and supplementary minor in Chemistry. In spring 2010, Richard was first introduced to Surface Science in the Catalysis and Surface Chemistry group during a minor internship under supervision of Matthijs van Spronsen and Maarten van Reijzen. He performed his final bachelor internship under supervision of Dr. Arban Uka and Dr. Ludo Juurlink, where he started designing and building one of the ultra-high vacuum setups described in chapter 2 of this thesis: Boxfish.

After obtaining his BSc diploma, Richard remained at Leiden University for his Research in Chemistry MSc. During his major research internship, he continued his previous work on Boxfish under supervision of Klaas Jan Schouten. The capabilities of Boxfish were expanded to include sample preparation and Reflection Absorption Infrared Spectroscopy. During the summer of 2012, he performed a paid heterogeneous catalysis project in the Catalysis and Surface Chemistry group. During this project, he prepared supported catalyst and subsequently built and applied a gas chromatography setup to test the catalysts to reproduce previous results. Finding interest for heterogeneous catalysis, Richard performed his second MSc research internship in 2013 under supervision of Dr. André Sijpkens at Avantium Chemicals B.V. During this work, another experimental setup

---

was built to study how drying and calcination conditions may be used to control the particle size of supported cobalt nanoparticles.

After obtaining his MSc in 2014, Richard started his PhD as part of the CO<sub>2</sub> neutral fuels project, funded by NWO, FOM, and Shell. The project was a collaboration between the Catalysis and Surface Chemistry group, again under supervision of Dr. Ludo Juurlink, and the Dutch Institute for Fundamental Energy Research, under supervision of Dr. Michael Gleeson. The aim of the project was to compare how CO<sub>2</sub> dissociation depends on vibrational and kinetic energy. To this end, an optical setup was constructed to prepare CO<sub>2</sub> from a supersonic molecular beam in a vibrationally excited state. (chapter 7) Initial experiments focused on double molecular beam experiments (chapter 5), to learn how to use the molecular beam apparatus, and developing reflection absorption infrared spectroscopy for use with curved single crystal surfaces (chapter 6). Significant delays in delivery of a working optical parametric oscillator meant some side projects were taken up that will benefit future projects involving state-resolved CO<sub>2</sub> dissociation at stepped surfaces. Richard looked into step type and step density dependencies of hydrogen dissociation (chapter 3), and isotopic scrambling of hydrogen (chapter 4). The former resulted in a publication in the prestigious scientific journal *Science*.

Richard attended and presented his results at a number of (international) conferences. Among others, he presented posters at the Gordon Research Conference on Dynamics at Surfaces in 2015 and 2017, the Netherlands Catalysis and Chemistry Conference, and the American Vacuum Society international symposium in 2019. He also gave oral presentations at: the Gordon Research Seminar on Dynamics at Surfaces in 2017, the Holland Research School of Molecular Chemistry symposium in 2018, and the American Vacuum Society international symposium in 2018. He competed for the Graduate Student Presentation Award for the latter. Richard also attended a number of courses, e.g. Tulip-VI Summer School on Modern Developments in Spectroscopy in 2015 and the Summer School On Plasma Chemistry in 2015. Richard also assisted in teaching General and Inorganic Chemistry to freshman students for three years.